The Shape Dependence of Chameleon Gravity

Thesis submitted to the University of Nottingham for the degree of
Doctor of Philosophy, 01/09/2023.

Chad John Briddon

14248573

Supervised by

Clare Burrage
Adam Moss

Abstract

The chameleon model is a modified gravity theory that introduces an additional scalar field that couples to matter through a conformal coupling. This 'chameleon field' possesses a screening mechanism through a nonlinear self-interaction term which allows the field to affect cosmological observables in diffuse environments whilst still being consistent with current local experimental constraints. Due to the self-interaction term, the equations of motion of the field are nonlinear and therefore difficult to solve analytically. The analytic solutions that do exist in the literature are either approximate solutions and or only apply to highly symmetric systems.

In this work I introduce the software package SELCIE (`https://github.com/C-Briddon/SELCIE.git`). This package equips the user with tools to construct an arbitrary system of mass distributions and then to calculate the corresponding solution to the chameleon field equation. It accomplishes this by using the finite element method and either the Picard or Newton nonlinear solving methods. I compare the results produced by SELCIE with analytic results from the literature including discrete and continuous density distributions. I find strong (sub-percentage) agreement between the solutions calculated by SELCIE and the analytic solutions.

One consequence of this screening mechanism is that the force induced by the field is dependent on the shape of the source mass (a property that distinguishes it from gravity). Therefore an optimal shape must exist for which the chameleon force is maximised. Such a shape would allow experiments to improve their sensitivity by simply changing the shape of the source mass. In this work I use a combination of genetic algorithms and SELCIE to find shapes that optimise the force at a single point in an idealised experimental environment. I note that the method I use is easily customised, and so can be used to optimise a more realistic experiment involving particle trajectories or the force acting on an extended body. I find the shapes outputted by the genetic algorithm possess common characteristics, such as a preference for smaller source masses, and that the largest fifth forces are produced by small 'umbrella'-like shapes with a thickness such that the source is unscreened but the field reaches its minimum inside the source. This remains the optimal shape even as we change the chameleon potential, and the distance from the source, and across a wide range of chameleon parameters. I find that by optimising the shape in this way the fifth force can be increased by 2.45 times when compared to a sphere, centred at the origin, of the same volume and mass.

Acknowledgements

I would like to thank my supervisors Clare Burrage and Adam Moss, for all of their guidance and support over the last four years. One piece of sage advise I will definitely hold onto is “perfect is the enemy of done”. I would like to thank my collaborator Andrius Tamosiunas for all of his hard work and contributions to SELCIE. I would also like to thank Daniela Saadeh for teaching me how to use FEniCS in the early days of this project. A very big thanks to Phil Parry, who has used his powers over computers to save me many a time. Also, thank you to Pamela Davies, Aggie Gasiorowska, and the rest of the office staff.

A big heart felt thanks to all the lovely people at CAPT for making it such a nice place to work. Thanks to Bradley March, my evil twin, for his help and advice regarding the art of making plots look nice. To Kieran Wood and his clockwork orange, I just want to tell you good luck. We’re all counting on you. Thank you to the always dapper Swagat Mishra, an amazing physicist and great guy, for always being there to explain the intricacies of the universe. Thank you also to my office mate Oliver Gould, who has answered countless random queries of mine. I am grateful for my friendships with the above, as well as the rest of the sky people: Matthew Gorton, Lauren Gaughan, and Sergio Sevillano Munoz. Also thanks to all the astronomy people past and present for your friendship.

I would like to thank my family who have always encouraged and supported me. Thank you to my sister Shannon, who risked her life on the Nottingham roundabouts to surprise visit me when I was down. You all mean the world to me.

Lastly, I would like to thank my lovely wife Hannah who has helped me throughout my PhD, both emotionally and through her unnatural knowledge of English grammar (big bucks). Thank you for everything.

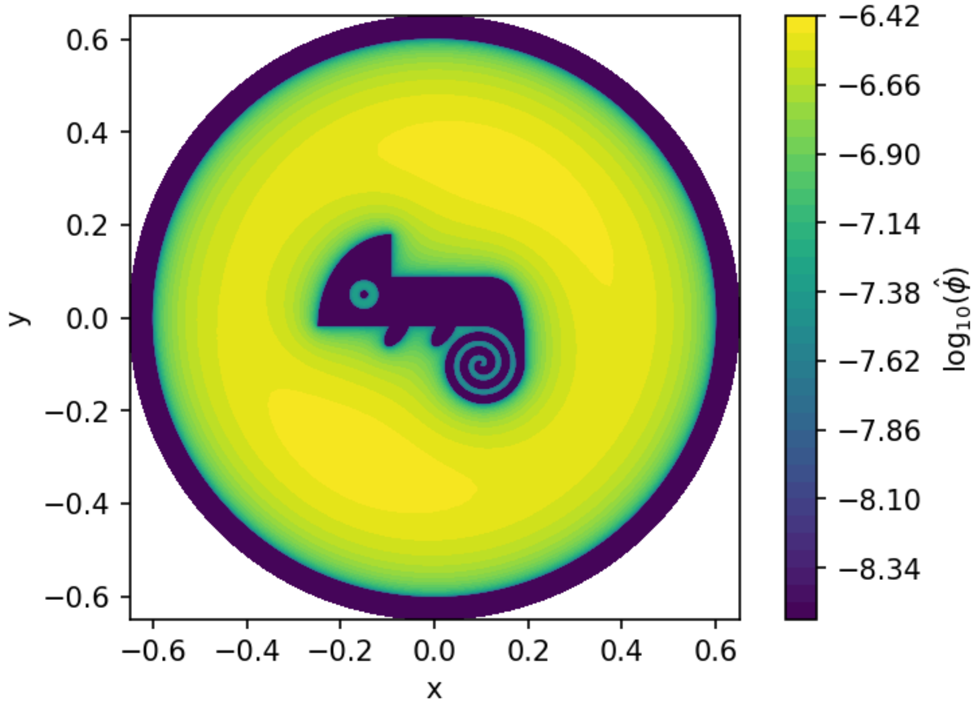

Figure 1: The chameleon field profile of a chameleon inside a vacuum chamber, calculated by SELCIE.

Declaration

I hereby declare that this dissertation is all my own work, except as indicated in the text. No part of the thesis has previously been submitted for a degree or other qualification at this or any other university.

The published original research is contained in the following publications:

[1] Chad Briddon, Clare Burrage, Adam Moss, and Andrius Tamosiunas. SELCIE: a tool for investigating the chameleon field of arbitrary sources. Journal of Cosmology and Astroparticle Physics, 2021(12):043, dec 2021.

[2] Andrius Tamosiunas, Chad Briddon, Clare Burrage, Weiguang Cui, and Adam Moss. Chameleon screening depends on the shape and structure of nfw halos. Journal of Cosmology and Astroparticle Physics, 2022(04):047, 2022.

[3] Andrius Tamosiunas, Chad Briddon, Clare Burrage, Alan Cutforth, Adam Moss, and Thomas Vincent. Chameleon screening in cosmic voids. Journal of Cosmology and Astroparticle Physics, 2022(11):056, 2022.

[4] Chad Briddon, Clare Burrage, Adam Moss, and Andrius Tamosiunas. Using machine learning to optimise chameleon fifth force experiments, 2023.

Chapters 2 and 3 contain work from [1] and [4] respectively, while some aspects of [2] and [3] is covered in chapter 4.

Contents

Abbreviations

BAO baryon acoustic oscillations.

CC cosmological constant.

FEM finite element method.

GA genetic algorithm.

GR general relativity.

NFW Navarro–Frenk–White.

QFT quantum field theory.

SELCIE Screening Equations Linearly Constructed and Iteratively Evaluated.

WEP weak equivalence principle.

Chapter 1

Introduction

Einstein's theory of general relativity (GR) is currently our best description of gravity. Under the assumption that gravity obeys GR at all scales, and that the universe is homogeneous and isotropic, the universe is found to be capable of periods of expansion. Through a variety of astrophysical and cosmological observations including type Ia supernova [5], baryon acoustic oscillations (BAO) [6], and gravitational waves [7, 8], it has been discovered that the universe is currently in a period of accelerated expansion. This indicates that the universe recently has become dominated by a vacuum energy refereed to as 'dark energy', the exact nature of which is not entirely understood. Some sources of this energy are a bare cosmological constant (CC) that appears in GR and zero-point fluctuations from quantum fields [9].

Another possible source, referred to as quintessence, introduces a scalar degree of freedom that starts to behave like a vacuum energy close to today [10, 11]. There is also the possibility that GR is an incomplete theory and so requires modifications [12]. However, through the use of a conformal transformation of the metric tensor, some modifications of GR can be recast as GR but with a new scalar degree of freedom that couples to matter [13]. This field would therefore mediate a new fundamental force due to this coupling. This ‘fifth force’ would be observed as deviations in gravitational phenomena from those predicted by GR. However, to date, all experimental results have been in agreement with the predictions of GR, placing strong constraints on the couplings between such a scalar field and matter, in models with a linear equation of motion [14, 15, 16]. This has motivated research into nonlinear scalar field models that possess screening mechanisms [12]. These models have fifth forces that are suppressed in and around regions of relatively high density, resulting in weaker experimental constraints. Some examples of such models include the symmetron [17], chameleon [18], and Galileon models [19].

In this work I will focus on the chameleon, which is a class of models where the field has an effective mass that scales with the local matter-energy density [18]. Consequently, in regions of high density, such as close to the Earth, the field’s mass is larger and interactions are suppressed. Despite this, numerous experiments, including torsion balance [20], Casimir [21, 22, 23, 24], levitated force sensors [25], atom interferometry [26, 27, 28, 29, 30], atomic spectroscopy [31, 32], neutron bouncing [33, 34, 35, 36, 37], and neutron interferometry [38, 39], have been able to constrain the chameleon parameter space, as will be discussed in section 1.6.3. For a comprehensive review of the constraints on the chameleon model see Refs. [40, 41, 42].

1.1 General Relativity

Since this work is in regards to modifications to GR, I will begin with a short review of the unmodified theory. In this section I outline some of the key concepts of GR and derive the most important expressions that will be needed when addressing the modified theory. I conclude this section by commenting on the successes of GR, along with some reasons that suggest the theory may require modifying.

The metric $g_{\mu\nu}$ is a rank-2 tensor that relates coordinate distances ($dx^\mu = (dt, d\vec{x})$) to the physical separation distances (ds) of two events in an arbitrarily curved space-time through the equation

$$ds^2 = g_{\mu\nu} dx^\mu dx^\nu, \tag{1.1}$$

where I have used the Einstein summation convention. The metric also has an inverse $g^{\alpha\beta}$ which is defined by the expression $g_{\mu\lambda} g^{\lambda\rho} = \delta^\rho_\mu$, where the Kronecker delta function δ^ρ_μ is unity if its indices match and zero otherwise. In GR the metric $g_{\mu\nu}$, and therefore the curvature of space-time itself, is treated as a dynamical field that depends on the matter-energy content of the universe. What we observe as gravitational forces then are objects following straight line trajectories, or geodesics, through a curved space-time where the curvature has been induced by the massive 'gravitating body'.

Under a change of coordinates $x^\mu \to \tilde{x}^\mu$, the infinitesimal displacement transforms as $dx^\mu \to \left(\partial x^\mu / \partial \tilde{x}^\alpha\right) d\tilde{x}^\alpha$, while ds^2 is invariant since it is a numerical value. Applying these transformation rules to equation (1.1), it can be shown that under this coordinate transformation the metric transforms as

$$\tilde{g}_{\alpha\beta}(\tilde{x}) = \left(\frac{\partial x^\mu}{\partial \tilde{x}^\alpha}\right) \left(\frac{\partial x^\nu}{\partial \tilde{x}^\beta}\right) g_{\mu\nu}(x). \tag{1.2}$$

This is the transformation rule for a tensor of rank-2 for a change of coordinates, with the general rule for a tensor of any rank being

$$\tilde{T}^{\mu_1'...\mu_k'}{}_{\nu_1'...\nu_q'} = \left(\frac{\partial \tilde{x}^{\mu_1'}}{\partial x^{\mu_1}}\right) ... \left(\frac{\partial \tilde{x}^{\mu_k'}}{\partial x^{\mu_k}}\right) \left(\frac{\partial x^{\nu_1}}{\partial \tilde{x}^{\nu_1'}}\right) ... \left(\frac{\partial x^{\nu_q}}{\partial \tilde{x}^{\nu_q'}}\right) T^{\mu_1...\mu_k}{}_{\nu_1...\nu_q}. \quad (1.3)$$

From this transformation rule it is simple to show that the partial derivative of a tensor is not itself a tensor. Instead the covariant derivative should be used, which is the tensor form of the partial derivative and when acting on a tensor is written as

$$\begin{aligned}\nabla_\sigma T^{\mu_1...\mu_k}{}_{\nu_1...\nu_k} = \partial_\sigma T^{\mu_1...\mu_k}{}_{\nu_1...\nu_k}& \\ + \Gamma^{\mu_1}_{\sigma\lambda} T^{\lambda...\mu_k}{}_{\nu_1...\nu_k} + ... + \Gamma^{\mu_k}_{\sigma\lambda} T^{\mu_1...\lambda}{}_{\nu_1...\nu_k}& \\ - \Gamma^{\omega}_{\sigma\nu_1} T^{\mu_1...\mu_k}{}_{\omega...\nu_k} - ... - \Gamma^{\omega}_{\sigma\nu_k} T^{\mu_1...\mu_k}{}_{\nu_1...\omega},& \quad (1.4)\end{aligned}$$

while becoming the partial derivative when acting on a scalar. In this definition $\Gamma^\lambda_{\mu\nu}$ is the metric connection, which is not a tensor but transforms under a coordinate change such that the covariant derivative of a tensor is itself a tensor. If we restrict the metric connection to ones that are symmetric in the lower indices[1] and are metric compatible ($\nabla_\sigma g_{\mu\nu} = 0$), then the unique choice of connection is

$$\Gamma^\lambda_{\mu\nu} = \frac{1}{2} g^{\lambda\omega} \left(\partial_\mu g_{\omega\nu} + \partial_\nu g_{\mu\omega} - \partial_\omega g_{\mu\nu}\right), \quad (1.5)$$

which is referred to as the Levi-Civita connection.

In flat space, particle trajectories follow straight lines, which can be considered as the particle's velocity vector being transported parallel to itself. The general expression for a vector being parallel transported through a curved space-time is $V^\mu \nabla_\mu V^\nu = 0$. Parallel transporting a particle's four-velocity

---

[1] This is done such that the torsion of the space-time, which is defined as $T^\sigma_{\mu\nu} = \Gamma^\sigma_{\mu\nu} - \Gamma^\sigma_{\nu\mu}$, is always zero.

$U^\mu = dx^\mu/d\tau$, where τ is the proper time, gives the geodesic equation

$$\frac{d^2x^\sigma}{d\tau^2} + \Gamma^\sigma_{\mu\nu} U^\mu U^\nu = 0. \tag{1.6}$$

The curvature of the space-time is a measure of how vectors change when parallel transported around an infinitesimally small closed loop, and this information is encoded by the Riemann curvature tensor

$$R^\alpha_{\mu\beta\nu} = \partial_\beta \Gamma^\alpha_{\mu\nu} - \partial_\nu \Gamma^\alpha_{\mu\beta} + \Gamma^\omega_{\mu\nu}\Gamma^\alpha_{\omega\beta} - \Gamma^\omega_{\mu\beta}\Gamma^\alpha_{\omega\nu}. \tag{1.7}$$

Contracting the upper and second lower indices we obtain the Ricci tensor

$$R_{\mu\nu} \equiv R^\rho_{\mu\rho\nu} = \partial_\sigma \Gamma^\sigma_{\mu\nu} - \partial_\nu \Gamma^\sigma_{\mu\sigma} + \Gamma^\sigma_{\mu\nu}\Gamma^\omega_{\sigma\omega} - \Gamma^\sigma_{\mu\omega}\Gamma^\omega_{\sigma\nu}, \tag{1.8}$$

which is then related to the Ricci scalar by $R = g^{\mu\nu}R_{\mu\nu}$.

The matter and energy of a system can be described by its energy-momentum tensor, which is defined as

$$T^{\mu\nu} = -\frac{2}{\sqrt{-g}}\frac{\partial \mathcal{L}_\mathrm{m}}{\partial g_{\mu\nu}}, \tag{1.9}$$

where $\mathcal{L}_\mathrm{m}$ is the Lagrangian density of the system. A tensor theory of gravity must relate the matter and energy of a system, described by the energy-momentum tensor, to the curvature of the space-time. Additionally, such a theory would need to be in agreement with Newton's law of gravitation in the non-relativistic regime and the curvature terms must be zero when acted upon by the covariant derivative, so as to agree with energy conservation ($\nabla_\mu T^{\mu\nu} = 0$). This ultimately leads to the Einstein equation

$$R_{\mu\nu} - \frac{1}{2}Rg_{\mu\nu} + \Lambda g_{\mu\nu} = M_\mathrm{pl}^{-2} T_{\mu\nu}, \tag{1.10}$$

where $M_{\rm pl} = \sqrt{1/8\pi G}$ is the reduced Planck mass, G is Newton's constant, and Λ is the cosmological constant (CC), which is required to be small to be consistent with Newton's law of gravitation. This equation describes how the matter and energy content of a system, $T_{\mu\nu}$, induces curvature in space-time, which then through the geodesic equation (1.6) governs how bodies move through that space-time. Rewriting equation (1.10) as an action gives the Einstein-Hilbert action

$$S = \int d^4x\sqrt{-g}\frac{M_{\rm pl}^2}{2}(R - 2\Lambda) - \int d^4x\mathcal{L}_{\rm m}, \tag{1.11}$$

Not only does equation (1.10) accurately reproduce Newton's laws of gravitation in the non-relativistic limit but it also accurately predicts the perihelion of Mercury [43], a feat that Newton's gravity could not account for barring the existence of unseen gravitational bodies. Other successful predictions of GR include: measuring light bending around the Sun [44], Shapiro time delay [45], gravitational waves [46], and even black holes which have recently been directly imaged for the first time [47, 48]. The weak equivalence principle (WEP) states that the inertial and gravitational mass of an object are equal, no matter the composition of the object. The consequence of this principle is that point like particles will fall in a gravitational field in the same way, independently of their composition. The WEP is a foundational concept in GR and any detected violations of this principle is tantamount to proving GR is not the fundamental theory of gravity. That being said, the recent MICROSCOPE experiment, which tests the WEP by precisely measuring the relative free fall of cylinders composed of different material, found no violations up to a precision of 10^{-15} [49]. Additionally, as will be discussed further in section 1.2, our universe appears to resemble one that is governed by GR and is homogeneous and isotropic on large scales.

Despite all the experimental and predictive success of GR, just like how the perihelion of Mercury hinted towards a more fundamental theory of gravity than that stated by Newton, there are aspects of GR that also hint towards the need for an even more fundamental theory, or modifications to our existing one. Some of these problems include: the fine-tuning of Λ so as to reproduce observations [9] (this will be elaborated upon in section 1.3), the fact that the effective field theory description of GR breaks down at high energies [50], and the existence of singularities at the centre of black holes [51]. Consequently, there are a plethora of modified gravity models in the literature that aim to resolve one or more of the above mentioned problems. The contents of this work, however, will only discuss a specific scalar-tensor theory known as the chameleon model, which is a modification of GR that exhibits different behaviour depending on the contents of the local environment, and leads to violations of the WEP.

1.2 A Homogeneous and Isotropic Universe

In the previous section, I discussed GR and how it relates the matter and energy content of space to the curvature of the surrounding space-time. In this section I will discuss the consequences of assuming that the universe is homogeneous and isotropic, and what GR can tell us about the evolution of such a universe. We will find that the evolution will depend on the energy contents of the universe, along with its intrinsic curvature, and can therefore be described using four constants. I will conclude this section by commenting on the values of these constants obtained from observations, and on some of the problems that arise specifically regarding the dark energy contribution.

The cosmological principle states that on large scales our universe becomes homogeneous and isotropic. The former states that there are no special points in the universe, while the latter states that there are no preferred directions. Applying the condition of homogeneity to a spatial metric imposes that it must be unchanged (form-invariant) under all translations. This is because if the metric is initially defined using coordinates that have Earth at the origin, after a translation the origin will have moved to a new position. If the universe is homogeneous then all choices of origin are equivalent and so the metric should have the same form, and therefore be independent of the choice of origin. By a similar argument, imposing the space to be isotropic means the metric must be form-invariant to rotation. For three spatial dimensions the metric will therefore be invariant to six independent transformations. Therefore, a spatial metric that obeys the cosmological principle must be maximally symmetric. Neglecting metrics related through a coordinate transformation, there exists only three unique solutions, each represented by the Robertson-Walker metric

$$ds^2 = -dt^2 + a^2(t)\left[\frac{dr^2}{1 - kr^2/R_0^2} + r^2 d\theta^2 + r^2 \sin^2(\theta) d\varphi^2\right], \tag{1.12}$$

where the curvature scale R_0 is a constant, and the specific maximally symmetric spatial solutions are spherical ($k = +1$), hyperbolic ($k = -1$), and flat ($k = 0$). The function $a(t)$, referred to as the scale factor, describes how this homogeneous and isotropic universe will evolve between maximally symmetric spatial slices, through expansion and contraction. Using equations (1.5) and (1.10), the Ricci tensor of the metric in equation (1.12) is calculated to be

$$\begin{aligned} R_{00} &= -3\frac{\ddot{a}}{a} && (1.13) \\ R_{\mathrm{ij}} &= \left(\left(\frac{2k}{a^2R_0^2}\right) + 2\left(\frac{\dot{a}}{a}\right)^2 + \left(\frac{\ddot{a}}{a}\right)\right) g_{\mathrm{ij}} && (1.14) \\ R_{0\mathrm{i}} &= 0, && (1.15) \end{aligned}$$

where I have used the short-hand $\dot{f}(t) = \frac{df}{dt}$.

Since we are taking the universe to be homogeneous and isotropic, we require its matter and energy content to be as well. This condition leaves the only valid option for the energy-momentum tensor to be that of a perfect fluid

$$T_{\mu\nu} = pg_{\mu\nu} + (\rho + p)U_\mu U_\nu, \tag{1.16}$$

where both the fluid's pressure, p, and energy density, ρ, are defined in the rest frame, while U^μ is the four-velocity of the fluid. Imposing conservation of energy ($\nabla_\mu T^{\mu\nu} = 0$) then results in the continuity equation

$$\dot{\rho} = -3\frac{\dot{a}}{a}(\rho + p). \tag{1.17}$$

If we consider a perfect fluid consisting of only relativistic particles (particles with momentum much larger than their mass), or of non-relativistic particles (particles with mass much larger than their momentum), then the pressure and density of the fluid will be related as $p = \omega\rho$, where the constant ω is the equation of state, and therefore equation (1.17) gives

$$\rho \propto a^{-3(1+\omega)}. \tag{1.18}$$

For non-relativistic fluids $\omega = 0$, and so $\rho \propto a^{-3}$, which matches the intuition of how the density of a fixed number of particles changes in an expanding volume of size $V \propto a^3$. For relativistic particles, such as photons, $\omega = 1/3$ and therefore behaves as $\rho \propto a^{-4}$. Recalling that the energy of a particle is inversely proportional to its wavelength, the extra inverse power of $a(t)$ implies relativistic particles are not only diluted in an expanding space, but also lose energy due to their wavelengths increasing with the expanding space. Through a rescaling of our time coordinate we can choose the scale factor to equal unity when $t = t_0$, where the subscript 0 denotes the value today. This choice then means the constant of proportionality in equation (1.18) is ρ_0.

Inputting the expression for $T_{\mu\nu}$ shown in equation (1.16) and the expressions for $R_{\mu\nu}$ shown in equations (1.13) - (1.15) into the Einstein equation (1.10), we arrive at the Friedmann equations

$$H^2 = \frac{\rho}{3M_{\rm pl}^2} + \frac{\Lambda}{3} - \frac{k}{a^2 R_0^2} \tag{1.19}$$

$$\frac{\ddot{a}}{a} = -\frac{1}{6M_{\rm pl}^2}(\rho + 3p) + \frac{\Lambda}{3}, \tag{1.20}$$

where $H(t) \equiv \dot{a}/a$ is the Hubble parameter. These two equations, along with the continuity equation (1.17), govern the evolution of a homogeneous and isotropic universe. The contents of said universe will be assumed to consist of relativistic radiation ($\rho_{\rm r}$) and non-relativistic matter ($\rho_{\rm m}$), neglecting any intermediate states. We can therefore express the total energy density of the universe as $\rho = \rho_{\rm r} + \rho_{\rm m} + \rho_\Lambda$, where the Λ-term on the right-hand side of equation (1.19) has been absorbed into the total energy density by expressing it as an effective energy density

$$\rho_\Lambda = \Lambda M_{\rm pl}^2. \tag{1.21}$$

This is the dark energy density[2] and since ρ_Λ is a constant in time, equation (1.18) implies that it has an equation of state of $\omega = -1$. In the case of a flat universe ($k = 0$), the total density is

$$\rho_{\mathrm{c}} = 3H^2 M_{\mathrm{pl}}^2, \tag{1.22}$$

which is referred to as the critical density, and is used to define the dimensionless density parameters $\Omega_{\mathrm{i}} \equiv \rho_{\mathrm{i}}/\rho_{\mathrm{c}}$ for $\mathrm{i} \in [\mathrm{r}, \mathrm{m}, \Lambda]$. Using this notation, we can rearrange equation (1.19) into the form

$$H^2 = H_0^2 \left(\Omega_{\mathrm{r},0} a^{-4} + \Omega_{\mathrm{m},0} a^{-3} + \Omega_{k,0} a^{-2} + \Omega_{\Lambda,0}\right), \tag{1.23}$$

where $\Omega_{\mathrm{i},0} \equiv \Omega_{\mathrm{i}}(t = t_0)$, $\Omega_{k,0} \equiv -k/(H_0 R_0)^2$, and I have made explicit how each density term varies with $a(t)$. In this form we see that the expansion history of an idealised universe can be described using only the four constants, $\Omega_{\mathrm{r},0}$, $\Omega_{\mathrm{m},0}$, $\Omega_{\Lambda,0}$, and H_0^2, where I have used the fact that when $t = t_0$ then equation (1.23) gives the constraint $\Omega_{k,0} = 1 - (\Omega_{\mathrm{r},0} + \Omega_{\mathrm{m},0} + \Omega_{\Lambda,0})$. In reality, however, this formula is only valid under the assumption that the number of particles that are relativistic and non-relativistic are fixed. As the universe expands and cools, relativistic particles can become non-relativistic and so the expansion during different eras will be described using formulas with the same form as equation (1.23), but with different density parameters. That being said, the contents of this work is only interested in late time cosmology post matter domination.

Through a combination of baryon acoustic oscillations and cosmic microwave background measurements, the curvature parameter is found to be very close to zero and so is treated as being zero in the base cosmologi-

---

[2] Non-CC contributions to the total dark energy content of the universe will be discussed in section 1.3.

cal model [52]. This means that all terms on the right-hand side of equation (1.23) are positive, and so $H(t) > 0$ at all times. Consequently, the universe will always be expanding, which will ultimately lead Ω_Λ to dominate at late times and the rate of growth to tend towards being exponential. Using a range of cosmological observations, and assuming $k = 0$, the remaining parameters are determined to be $\Omega_{\mathrm{r},0} \approx 9.0 \times 10^{-5}$, $\Omega_{\mathrm{m},0} \approx 0.31$, $\Omega_{\Lambda,0} \approx 0.69$, and $H_0 \approx 67$ kms^{-1}Mpc^{-1} [53]. Additionally, the baryonic matter contribution is only $\Omega_{\mathrm{b},0} \approx 0.05$, with the majority of the matter content of the universe being made of matter that has only been observed through its gravitational interaction, and so is referred to as 'dark matter' [53]. Therefore, the cosmological model discussed throughout this section is called the ΛCDM model, where CDM stands for 'cold dark matter'.

1.3 The Cosmological Constant Problem

The measured value of the dark energy density is $\rho_\Lambda \approx (2.4 \text{ meV})^4$. In the previous section, this density was determined entirely by the CC that appears in the Einstein equations (1.10). In reality, however, this dark energy would also receive contributions from the 'vacuum energy' that arises from the zero-point fluctuations of quantum fields. These fluctuations are a prediction of quantum field theory (QFT) and are a property of the vacuum. Therefore, since the vacuum is Lorentz invariant, the energy-momentum tensor of this vacuum energy will be

$$T_{\mu\nu}^{\mathrm{QFT}} = -\langle\rho\rangle g_{\mu\nu}, \tag{1.24}$$

which clearly behaves as a CC, when compared to equation (1.10). From vacuum loop calculations the contribution of a single particle of mass m

to the vacuum energy is expected to go as $\langle\rho\rangle \sim m^4$ [9]. This is usually not of too much interest since most of physics is concerned with changes in energy and not the absolute values. However, this is not the case with GR which states that all energy, including vacuum energy, will induce space-time curvature. Considering both CC and QFT contributions the total effective dark energy is

$$\rho_{\text{eff}} = \rho_\Lambda + \sum_{\text{i}} \langle\rho_{\text{i}}\rangle, \tag{1.25}$$

where the summation is over all particle species. As discussed in section 1.2, we have measurements of ρ_{eff} from cosmological observations. However, the QFT contributions are found to be substantially larger than the measured value of ρ_{eff}. Allowing particle masses up to the TeV scale, this corresponds to a ratio of $\langle\rho\rangle/\rho_{\text{eff}} \sim 10^{60}$. This means that the value of the bare CC, Λ, must be extremely fine-tuned so as to ensure the effective value is small. The requirement of this fine-tuning is the CC problem. There are a range of proposed solutions to the CC problem, including invoking the anthropic principle, extra dimensions, and modifications to GR [54, 55, 56, 57].

1.4 Quintessence

One proposed solution to the CC problem is that the observed dark energy is sourced by a scalar field, ϕ, while some undiscovered mechanism causes the bare constant to cancel the QFT contribution [11]. Such a field is called a quintessence field and if we neglect any possible couplings to other non-gravitational fields, the action of such a field is

$$S = \int d^4x\sqrt{-g}\left[-\frac{1}{2}g^{\mu\nu}\partial_\mu\partial_\nu\phi - V(\phi)\right], \tag{1.26}$$

where $V(\phi)$ is the field's potential. Varying the action with respect to ϕ gives the equation of motion for the field as

$$\ddot{\phi} + 3H\dot{\phi} + V'(\phi) = 0, \tag{1.27}$$

where since we are working under the cosmological principle, the spatial derivatives of the field are zero and the metric is of the form (1.12). This field equation is of the same form as the Klein-Gordon equation, but with an addition term known as the Hubble friction. The pressure and energy density of this scalar field are

$$p_\phi = \frac{1}{2}\dot{\phi}^2 - V(\phi) \tag{1.28}$$

$$\rho_\phi = \frac{1}{2}\dot{\phi}^2 + V(\phi), \tag{1.29}$$

which gives an equation of state of

$$\omega_\phi = \frac{\dot{\phi}^2 - 2V(\phi)}{\dot{\phi}^2 + 2V(\phi)}. \tag{1.30}$$

This implies that a scalar field whose potential is much larger that its kinetic part will behave like a CC with $\omega_\phi \approx -1$. On the other hand, if the field is dominated by its kinetic part it will have an equation of state $\omega_\phi \approx +1$. Equation (1.18) then implies that the field will dilute as $a^{-6}(t)$, which is faster than both matter and radiation at $a^{-3}(t)$ and $a^{-4}(t)$ respectively. This means that, depending on whether the field's kinetic or potential energy term dominates, it will determine if the field is diluting faster than the other components or has constant energy density. If the scalar has a monotonically decreasing potential, the dynamics of equation (1.27) will, for a wide range of initial conditions, lead the scalar field's equation of state to converge to a common evolutionary track [10]. These are known as tracking solutions; they reduce the problem of obtaining a scalar field that is subdominant at early times but dominates at late times to finding an appropriate form for the field's potential, and not on its initial conditions. The current measured value for the equation of state of the cosmological dark energy has an upper-bound of $\omega_{\rm DE} \lesssim -0.95$ [53, 58]. Therefore, a further constraint on the potential of a dark energy candidate scalar field is that its equation of state today satisfies this observational constraint. On the other hand, if more accurate measurements of $\omega_{\rm DE}$ start to become in tension with the CC value, then this would be evidence in favour of a quintessence model.

Throughout this section we assumed that the scalar field does not couple to the matter sector. If such a coupling did exist, however, it would mean that this field would mediate a new fundamental force. Therefore, such a coupling would be very tightly constrained due to laboratory experiments, such as torsion balance, and solar system dynamics, such as lunar laser ranging [14, 59]. In section 1.6, I will discuss a model where the scalar field can have a larger coupling strength whilst still satisfying the observational constraints mentioned above through the use of a screening mechanism.

1.5 Conformal Transformations

The scalar field, discussed in the previous section, was a possible candidate for the observed dark energy. In this section I will show how a modified version of GR involving an explicit, non-minimal, coupling between a scalar field and gravity can, through a change of reference frame, be equated to GR with an additional scalar degree of freedom. However, unlike in the previous section, where the scalar field was assumed to not couple to matter, a consequence of the frame transformation is that the field becomes non-minimally coupled to the matter sector. I will then state the strength of the force that acts on matter due to this coupling.

As mentioned in section 1.1, GR has many experimental and predictive successes, but there also exists hints that a more fundamental theory is required. According to Lovelocks's theorem [60, 61] if we wish to construct a gravitational action which only depends on a local 4-dimensional metric $g_{\mu\nu}$ and is Lorentz invariant, then the only possible choice that gives second-order equations of motion (for higher than second-order Ostrogradsky instabilities can occur [62]) are ones that have the same form as the Einstein-Hilbert action shown in equation (1.11). This means any theory that modifies the GR action must break one of the conditions stated in Lovelock's theorem. We have already explored how introducing a new scalar degree of freedom could amend the fine-tuning problem, as discussed in section 1.4. In this section I will show how modifying the curvature term in the action shown in equation (1.11) can be equated to GR with a scalar degree of freedom that couples to the matter fields, thereby breaking the Lovelock condition that $g_{\mu\nu}$ is the only field in the gravitational sector.

To start I will introduce the conformal transformation

$$g_{\mu\nu} = A^2(\varphi)\tilde{g}_{\mu\nu}, \tag{1.31}$$

where φ is a dynamical scalar field. Applying this to equation (1.5), and using the notation $A'(\varphi) = \partial A/\partial\varphi$, we obtain that the Levi-Civita connection in the $\tilde{g}_{\mu\nu}$ frame is

$$\tilde{\Gamma}^{\sigma}_{\mu\nu} = \Gamma^{\sigma}_{\mu\nu} - \frac{A'}{A}\left(\delta^{\sigma}_{\mu}\varphi_{,\nu} + \delta^{\sigma}_{\nu}\varphi_{,\mu} - g_{\mu\nu}g^{\sigma\lambda}\varphi_{,\lambda}\right), \tag{1.32}$$

where I have used the short-hand $f_{,\mu} = \partial f / \partial x^{\mu}$. Inputting equation (1.32) into equation (1.8) gives that the Ricci tensor transforms as

$$A^{-2}\tilde{R} = R + 6\left[\Box \ln(A) - g^{\mu\nu}\left(\nabla_{\mu}\ln(A)\right)\left(\nabla_{\nu}\ln(A)\right)\right], \tag{1.33}$$

where $\Box$ is the d'Alembert operator. If we assume a modified gravity model with an action

$$S = \int dx^4\sqrt{-g}\left(\frac{M_{\rm pl}^2}{2}A^2(\varphi)\tilde{R} - \frac{1}{2}\tilde{g}^{\mu\nu}\partial_{\mu}\varphi\partial_{\nu}\varphi - \tilde{V}(\varphi)\right) - \int d^4x\mathcal{L}_{\rm m}(\tilde{g}_{\mu\nu}, \psi_{\rm i}), \tag{1.34}$$

where $\mathcal{L}_{\rm m}(\tilde{g}_{\mu\nu}, \psi_{\rm i})$ represents the dynamics of the matter fields, then applying the conformal transformation shown in equation (1.31), followed by a field redefinition of the form

$$\left(\frac{d\phi}{d\varphi}\right)^2 = \frac{1}{A^2} + 6M_{\rm pl}^2\left(\frac{A'}{A}\right)^2, \tag{1.35}$$

will give the action of the theory as

$$S = \int dx^4\sqrt{-g}\left(\frac{M_{\rm pl}^2}{2}R - \frac{1}{2}g^{\mu\nu}\partial_{\mu}\phi\partial_{\nu}\phi - V(\phi)\right) - \int d^4x\mathcal{L}_{\rm m}(A^{-2}(\phi)g_{\mu\nu}, \psi_{\rm i}), \tag{1.36}$$

where $\tilde{V}(\varphi) = A^4(\phi)V(\phi)$. Note that the $\Box \ln(A)$ term from the conformal transformation of R is missing since it is a total derivative and so contributes zero so long as $\partial_{\mu}\phi = 0$ at infinity. Since physical observables are not affected by our choice of frame, the two actions shown in equations (1.34) and (1.36) must be equivalent. Therefore, a modified gravity theory of the form (1.34) is equivalent to GR with a scalar field non-minimally coupled to the non-gravitational fields. In this work the initial frame, $\tilde{g}_{\mu\nu}$, shall be referred to as the Jordan frame, while the Einstein frame, $g_{\mu\nu}$, is the one for which the curvature part of the action is the same as in GR.

Using the definition of the energy-momentum tensor in equation (1.9) we see that under the conformal transformation in equation (1.31) it transforms as

$$\tilde{T}^{\mu\nu} = A^6 T^{\mu\nu}, \tag{1.37}$$

and therefore its trace ($\tilde{T} = \tilde{g}_{\mu\nu}\tilde{T}^{\mu\nu}$) will transform as

$$\tilde{T} = A^4 T. \tag{1.38}$$

Using these transformation laws and varying the action in equation (1.36) with respect to ϕ, the field's equation of motion is

$$\Box\phi = V'(\phi) - \frac{\beta(\phi)}{M_{\rm pl}} A^{-4}\tilde{T}, \tag{1.39}$$

where the coupling strength $\beta(\phi)$ is defined as

$$\beta(\phi) \equiv -M_{\rm pl}\frac{d\ln(A)}{d\phi}. \tag{1.40}$$

We see that the equation of motion is simply the Klein–Gordon equation, but with an extra term due to the conformal coupling which couples the field to the trace of the energy-momentum tensor in the Jordan frame[3]. Consequently, the scalar field does not couple to relativistic particles, like photons, since they are traceless ($T = 0$). The reason the field is written in terms of its coupling to matter in the Jordan frame is because in this frame particle masses and couplings have no dependence on ϕ.

If we consider a test particle of mass m in the Einstein frame, its motion will go along geodesics governed by equation (1.6). Returning to the Jordan

---

[3] When applying a conformal transformation, of the form shown in equation 1.31, to the standard model action, and after performing canonical normalisation, only the Higg's mass term will explicitly depend on the conformal factor, $A(\phi)$. Therefore, if the Higgs was massless, then the scalar field would not couple to the matter sector [63].

frame, by substituting equation (1.32) into (1.6), we see that the geodesic can be expressed as

$$\frac{d^2x^\sigma}{d\tau^2} + \tilde{\Gamma}^\sigma_{\mu\nu} U^\mu U^\nu = \frac{\beta(\phi)}{M_{\text{pl}}} \left(2U^\sigma \dot{\phi} + \tilde{g}^{\mu\lambda} \phi_{,\lambda} \right). \tag{1.41}$$

While the left-hand side of this expression is the usual geodesic equation (1.32), the right-hand side is not necessarily zero, representing a new force mediated by the scalar field. This 'fifth force' is therefore a means of confirming the existence of such a conformal scalar field. For particles that move much slower than the speed of light ($v \ll 1$) the term on the right-hand side of equation (1.41) simplifies to

$$\vec{F}_\phi = -m \frac{\beta(\phi)}{M_{\text{pl}}} \vec{\nabla} \phi. \tag{1.42}$$

The contents of this work shall focus solely on a conformal model known as the chameleon model. However, for completeness I will comment that modifications to GR of the kind shown in equation (1.34) are not the only ones that can be equated to GR but with an additional scalar degree of freedom. One potential solution to address why gravity is so much weaker than the other forces is that it exists in a higher-dimensional space, which can be evaluated as an effective 4-dimensional theory with additional scalar degrees of freedom through dimensional reduction [64]. Additionally, there exist other models consisting of a scalar field coupled to gravity. Any scalar tensor theory that has equations of motion no higher than second-order, including the class of models discussed in this section, can all be shown to be subclasses of the Horndeski Lagrangian [65]. DHOST (Degenerate Higher Order Scalar Tensor) models are a further generalisation of scalar tensor theories, where the equations of motion are capable of being greater than second-order, but with no Ostrogradsky instabilities [66, 67].

1.6 The Chameleon Model

In the previous section, I showed how a conformal transformation can be used to equate a modified gravity action to the GR action at the cost of introducing a scalar degree of freedom non-minimally coupled to the matter sector. This section focuses on a specific conformal field model know as the chameleon, and how its screening mechanism allows it to avoid observational constraints from high density regions. I will then discuss some approximate analytic solutions to the field's nonlinear equation of motion for highly-symmetrical source shapes, including spheres, cylinders, and ellipsoids. Some examples of experiments that have constrained the chameleon model's parameter space will be provided at the end of this section.

1.6.1 The Chameleon Screening Mechanism

Using the definition of the coupling strength shown in equation (1.40), we see that by choosing to have a coupling strength that is a constant in ϕ this gives a conformal factor of

$$A(\phi) = e^{-\frac{\beta\phi}{M_{\rm pl}}}. \tag{1.43}$$

In principle each matter species can have a different coupling strength; however, in this work, along with much of the literature, a universal coupling strength shall be assumed for all matter species. This means that the chameleon's equation of motion, in the Einstein frame, is exactly the same as that shown in equation (1.39).

Desiring the chameleon to act as late time dark energy, as discussed in section 1.4, we shall assume it to have a potential

$$V(\phi) = \frac{\Lambda^{n+4}}{\phi^n}, \tag{1.44}$$

where Λ is a mass scale and n is an integer[4], following Ref. [18]. Throughout this work we shall be in the non-relativistic regime, and can therefore make use of the approximation $\tilde{T} \approx -\rho$, where ρ is the energy density of non-relativistic matter in the Jordan frame. Therefore the non-relativistic equation of motion for the chameleon field is

$$\Box\phi = -\frac{n\Lambda^{n+4}}{\phi^{n+1}} + \frac{\beta\rho}{M_{\text{pl}}}, \tag{1.45}$$

where we have also assumed $M_{\text{pl}} \gg \beta\phi$, and so $e^{-\beta\phi/M_{\text{pl}}} \approx 1$. This field equation is a Klein-Gordon equation with an effective potential of

$$V_{\text{eff}}(\phi) = V(\phi) + \frac{\beta\rho}{M_{\text{pl}}}\phi. \tag{1.46}$$

Since the bare potential, $V(\phi)$, is a monotonically decreasing function for $n > 0$, the effective potential will therefore have a minimum at the field value

$$\phi_{\text{min}}(\rho) = \Lambda \left(\frac{nM_{\text{pl}}\Lambda^3}{\beta\rho}\right)^{\frac{1}{n+1}}, \tag{1.47}$$

and therefore the mass of the chameleon field at the position of this minimum is

$$m_\phi^2 = V''_{\text{eff}}(\phi_{\text{min}}) = n^{-\frac{1}{(n+1)}}(n+1)\Lambda^2 \left(\frac{\beta\rho}{M_{\text{pl}}\Lambda^3}\right)^{\frac{(n+2)}{(n+1)}}. \tag{1.48}$$

We see from equation (1.48) that the effective mass of the field depends on ρ, such that as ρ increases so does the mass. This means the field's

---

[4] I note here that in principle n can take some negative values. However, due to time constraints the contents of this thesis focus solely on models where $n > 0$.

Compton wavelength, $\lambda = 1/m_\phi$, will be smaller in regions of higher density, resulting in any forces mediated by the field to become suppressed. This is the chameleon's screening mechanism which allows it to avoid constraints from Earth bound and solar system experiments, while having a non-negligible contribution on cosmological scales. Additionally, the fact that the minimum of the chameleon's effective potential, equation (1.47), depends on the matter density makes it an ideal tracker solution [68].

One consequence of the chameleon's screening mechanism is that large dense sources of matter will exhibit a 'thin-shell' effect. This is because contributions to the fifth force from matter inside a dense source will be suppressed by the screening mechanism. Consequently, the fifth force will effectively be sourced by a thin-shell of matter at the edge of the source mass only, and not the entire mass as is the case in GR. Since the Earth and other dense objects are presumably screened, we would only observe gravitational effects as expected of GR, while the chameleon contribution would be relatively negligible. Another consequence of this thin-shell effect is that it would violate the WEP as screened and unscreened bodies would not experience the same fifth force and so would follow different trajectories, governed by equation (1.41). In the following subsection, I will discuss how the thin-shell effect is used in the literature to construct approximate analytic solutions.

1.6.2 Approximate Analytic Solutions

The parameters of the chameleon model are the integer n, which controls the form of the bare potential, the coupling strength to matter β, and the self-coupling strength Λ, which if the chameleon does source the observed dark energy should have a value of $\Lambda_{\mathrm{DE}} = 2.4$ meV as indicated in section

1.3. To understand the constraints on the chameleon model from existing observations and identify which regions of the parameter space remain viable, exact solutions to the equation of motion, equation (1.45), are required. However, the nonlinear nature of equation (1.45), while providing the chameleon with its screening mechanism, makes obtaining exact solutions extremely difficult. The approach often adopted in the literature to solve for the field around a source of density $\rho_{\rm c}$ in a background of density $\rho_{\rm bg}$ is to take advantage of the thin-shell effect by approximating the chameleon's effective potential, equation (1.46), as

$$V_{\rm eff}(\phi) \approx \begin{cases} m_{\rm c}(\phi - \phi_{\rm c}) & \text{, screened inner region} \\ \beta\rho_{\rm c}/M_{\rm pl}^2 & \text{, thin-shell} \\ m_{\rm bg}(\phi - \phi_{\rm bg}) & \text{, background,} \end{cases} \tag{1.49}$$

where $\phi_{\rm c}$ and $\phi_{\rm bg}$ are the field values that minimise the effective potential inside the source and in the background respectively, equation (1.47), and $m_{\rm c}$ and $m_{\rm bg}$ are the corresponding field masses, equation (1.48). These solutions can then be pieced together by enforcing the field to be continuous at the boundaries between these regions. I will now discuss some examples of approximate analytic solutions from the literature that are constructed using this approach, each of which are for the $n = 1$ model as this is the most researched.

Sphere

The approximate analytical solution for a spherical source was first derived in Ref. [18]. Since the source is static we assume the field has no time dependence. Additionally, given the spherical symmetry of the system the

Laplacian can be written as

$$\nabla^2 \phi = \frac{1}{r^2} \frac{\partial}{\partial r} \left(r^2 \frac{\partial \phi}{\partial r} \right), \tag{1.50}$$

where r is the radial coordinate. Solving the static Klein-Gordon equation for each form of the effective potential in equation (1.49) gives three equations consisting of six unknown constants of integration. Using the index $\mathrm{i} \in [\mathrm{c}, \mathrm{bg}]$, both the solutions for the inner screened and background regions can be expressed as

$$\phi = \phi_{\mathrm{i}} + \frac{A_{\mathrm{i}}}{r} e^{+m_{\mathrm{i}} r} + \frac{B_{\mathrm{i}}}{r} e^{-m_{\mathrm{i}} r}, \tag{1.51}$$

where A_{i} and B_{i} are constants. Applying the boundary conditions $\phi(r = 0) = \phi_{\mathrm{c}}$ and $\phi(r \to \infty) = \phi_{\mathrm{bg}}$, we see that $A_{\mathrm{c}} = B_{\mathrm{c}} = 0$ and $A_{\mathrm{bg}} = 0$. This therefore reduces the number of unknowns to three. If the sphere is screened then there is an additional unknown, R_{c}, which is the boundary of the screened region, such that $\phi = \phi_c$ when $r \leq R_{\mathrm{c}}$. Enforcing the field, and its derivative, to be continuous at the boundaries of the thin-shell, $r \in [R_{\mathrm{c}}, R]$, gives four constraint relations that can be used to calculate these unknowns. The resulting approximate solution for the chameleon field profile produced by a spherical source of radius R can then be written as

$$\phi(r) \approx \begin{cases} \phi_{\mathrm{c}} & , 0 \leq r \leq R_{\mathrm{c}} \\ \frac{\beta \rho_{\mathrm{c}}}{6 M_{\mathrm{pl}}^2} \left(r^2 + \frac{2 R_{\mathrm{c}}^3}{r} - 3 R_{\mathrm{c}}^2 \right) & , R_{\mathrm{c}} \leq r \leq R \\ \phi_{\mathrm{bg}} - \left(\frac{3\beta}{4\pi M_{\mathrm{pl}}} \right) \left(\frac{\Delta R}{R} \right) \frac{M_{\mathrm{c}}}{r} e^{-m_{\mathrm{bg}}(r-R)} & , R \leq r, \end{cases} \tag{1.52}$$

where M_c is the mass of the source and $\Delta R = R - R_{\mathrm{c}}$ is the width of the thin-shell. Since we are interested in models that are relevant on cosmological scales, the field's Compton wavelength in vacuum is assumed to be large. Therefore, in the bottom expression of equation (1.52) it was assumed that $m_{\rm bg}R \ll 1$. It is also assumed that the thin-shell is small, which gives the constraint relation

$$\frac{\Delta R}{R} = \frac{|\phi_{\rm bg} - \phi_c|}{6\beta M_{\rm pl}\Phi_c} \ll 1, \tag{1.53}$$

where $\Phi_c = M_c/8\pi M_{\rm pl}^2 R$ is the Newtonian potential at the surface of the source. Equation (1.53) is the condition determining whether objects are large and dense enough (more specifically objects with a sufficiently high surface Newtonian potential) to have a thin-shell and thus be screened. For an unscreened source, $\Delta R/R > 1$, the field can be solved using the exact same method as discussed above but with $R_{\rm c} \to 0$ and dropping the requirment that $\phi(r = 0) = \phi_{\rm c}$. Therefore, the field profile of an unscreened source has an equivalent solution to equation (1.52) but with the substitution $\Delta R/R \to 1$.

For cases where $\rho_{\rm c} \gg \rho_{\rm bg}$ this implies that $\phi_{\rm c} \ll \phi_{\rm bg}$, due to equation (1.47). Applying this to equation (1.53) and then substituting it into equation (1.52) gives the background field solution in the form

$$\phi(r) \approx \phi_{\rm bg}\left(1 - \frac{R}{r}e^{-(r-R)/\lambda_{\rm bg}}\right), \tag{1.54}$$

where $\lambda_{\rm bg} = 1/m_{\rm bg}$ is the Compton wavelength of the field in the background. This form of the solution will be used later in this work.

Cylinder

As shown in Ref. [26], we can obtain the chameleon field profile around a cylindrical source by utilising the same methodology as was used above for the spherical case. For a static cylindrical system, the Laplacian simplifies to

$$\nabla^2\phi = \frac{1}{r}\frac{\partial}{\partial r}\left(r\frac{\partial\phi}{\partial r}\right), \tag{1.55}$$

where r is the radial distance as defined in cylindrical coordinates. As before, we solve the static Klein-Gordon equation using each of the approximations of the effective potential in equation (1.49), once again giving us three equations with six unknown constants of integration. The solutions will involve modified Bessel functions of the first and second kind, $\mathcal{I}_0(x)$ and $\mathcal{K}_0(x)$ respectively, since they are solutions to the ordinary differential equation

$$x^2y'(x) + xy'(x) - x^2 = 0. \tag{1.56}$$

Enforcing the same boundary conditions as was used in the spherical case, and requiring the field to be continuous at the boundary of the cylinder, R, and the edge of the thin-shell region, S, we arrive at the piece-wise solution

$$\phi(r) \approx \begin{cases} \phi_{\rm c} & , 0 < r \leq S \\ \phi_{\rm c} + \frac{\beta\rho_{\rm c}r^2}{4M_{\rm pl}}\left(1 - \frac{S^2}{r^2} + 2\ln\left(\frac{S}{r}\right)\right) & , S \leq r \leq R \\ \phi_{\rm bg} - \frac{\beta\rho_{\rm c}R^2}{2M_{\rm pl}}\left(1 - \frac{S^2}{R^2}\right)\mathcal{K}_0(m_{\rm bg}r) & , R \leq r, \end{cases} \tag{1.57}$$

where again the bottom expression has been simplified by assuming $m_{\rm bg}R \ll 1$. The expression for the radial value where the thin-shell starts, S, is

$$\frac{4M_{\rm pl}\phi_{\rm bg}}{\beta\rho_c R^2} = \left(1 - \frac{S^2}{R^2}\right)\left(1 - 2\gamma_E - 2\ln\left(\frac{m_{\rm bg}R}{2}\right)\right) + \frac{2S^2}{R^2}\ln\left(\frac{S}{R}\right), \tag{1.58}$$

where γ_E is the Euler-Mascheroni constant. Like in the spherical case, we see that the source must be sufficiently large and dense to have a thin-shell ($S \neq R$). In the regime where $m_{\rm bg}R \ll 1$, equation (1.58) simplifies to

$$1 - \frac{S^2}{R^2} \approx -\frac{2M_{\rm pl}\phi_{\rm bg}}{\beta\rho_{\rm c}R^2\ln(m_{\rm bg}R/2)}. \tag{1.59}$$

Substituting this into the bottom expression in equation (1.57) gives the field profile for $r > R$ as

$$\phi(r) \approx \phi_{\mathrm{bg}} \left(1 - \frac{2\mathcal{K}_0(r/\lambda_{\mathrm{bg}})}{\ln(4\lambda_{\mathrm{bg}}^2/R)} \right). \tag{1.60}$$

Since this solution assumes cylindrical symmetry it would only be valid around an infinitely long cylinder. That said, for very long but finite cylinders the field profile around the cylinder should be well approximated by equation (1.60) when sufficiently far from the ends of the cylinder.

Ellipsoids

In Ref. [69] an attempt was made to derive an approximate analytic solution for the chameleon field around an ellipsoidal shape. On inspection, however, this expression was incorrect and so I will recalculate it using the same method as shown in Ref. [69] . The coordinate system that will be used is

$$\begin{aligned} x &= a\sqrt{(\xi^2 - 1)(1 - \eta^2)} \cos(\phi), \\ y &= a\sqrt{(\xi^2 - 1)(1 - \eta^2)} \sin(\phi), \\ z &= a\xi\eta, \end{aligned} \tag{1.61}$$

where a is the distance from the ellipse's foci to the origin, η is analogous to an angular coordinate ($-1 \leq \eta \leq +1$), ξ is analogous to a radial coordinate ($1 \leq \xi < \infty$), and ϕ is the azimuthal angle ($0 \leq \phi < 2\pi$). In these coordinates the Laplacian is

$$\begin{aligned} \nabla^2 = &\frac{1}{a^2(\xi^2 - \eta^2)} \left(\frac{\partial}{\partial \xi}(\xi^2 - 1)\frac{\partial}{\partial \xi} + \frac{\partial}{\partial \eta}(1 - \eta^2)\frac{\partial}{\partial \eta} \right) \\ &+ \frac{1}{a^2(\xi^2 - 1)(1 - \eta^2)} \frac{\partial^2}{\partial \varphi^2}. \end{aligned} \tag{1.62}$$

The sources that will be investigated are rotationally symmetric around the azimuthal-axis, and so the field will be independent from φ. Note that unlike the previous approximate analytic solutions discussed in this section, where the symmetry of the source reduced the effective problem to 1-dimensional, the solution around an elliptical source will be 2-dimensional. After applying the rotational symmetry, what remains of the Laplacian has a separable form, and so the ansatz for the form of the field is

$$\phi(\xi,\eta) = \sum_{\mathrm{l}=0}^{\infty} X_{\mathrm{l}}(\xi) H_{\mathrm{l}}(\eta). \tag{1.63}$$

Using this ansatz we obtained the pair of separable equations

$$\frac{\partial}{\partial\xi}\left((\xi^2-1)\frac{\partial X_l(\xi)}{\partial\xi}\right) - \lambda_l X_l(\xi) = 0 \tag{1.64}$$

$$\frac{\partial}{\partial\eta}\left((1-\eta^2)\frac{\partial H_l(\eta)}{\partial\eta}\right) + \lambda_l H_l(\xi) = 0. \tag{1.65}$$

It is then shown in Ref. [69], that $\lambda_l = l(l+1)$, thereby reducing equations (1.64) and (1.65) into copies of the Legendre equation

$$(1-x^2)y''(x) - 2xy'(x) + n(n+1)y(x) = 0, \tag{1.66}$$

the solutions to which are the Legendre functions of the first and second kinds, $P_n(x)$ and $Q_n(x)$ respectively. Therefore, after taking into account the domains of the different kinds of Legendre functions, the ansatz for the form of the field shown in equation (1.63) becomes

$$\phi(\xi,\eta) = \sum_{l=0}^{\infty} \left[A_l P_l(\eta) P_l(\xi) + B_l P_l(\eta) Q_l(\xi)\right], \tag{1.67}$$

where A_l and B_l are constants.

We take our source ellipsoid to be bounded by $\xi = \xi_0$, and assume the boundary of the thin-shell with the screened inner region to be at $\xi = \xi_{\rm c}$. Note that we are making the implicit assumption that the boundary where the field starts to vary inside the source is independent of the angular position η. Inside the screened region the field is $\phi = \phi_{\rm c}$, while inside the thin-shell it is

$$\begin{aligned}\phi = &\sum_{l=0}^{\infty}\left[A_l P_l(\eta)P_l(\xi) + B_l P_l(\eta)Q_l(\xi)\right] \\ &+ \frac{a^2\beta\rho_{\rm c}}{M_{\rm pl}}(\xi^2-1)\left[P_0(\eta) - P_2(\eta)\right],\end{aligned} \tag{1.68}$$

and in the background regions it is assumed to have the form

$$\phi = \phi_{\rm bg} + \sum_{l=0}^{\infty} C_l P_l(\eta)Q_l(\xi), \tag{1.69}$$

where we have used the boundary condition at $\xi \to \infty$, and have taken $m_{\rm bg} \approx 0$. We shall now enforce that the field, and its gradient with respect to ξ, are continuous at the boundaries ξ and ξ_0. Since the Legendre functions of the first kind form a complete basis, enforcing continuity also means the coefficients corresponding to the functions $P_l(\eta)$ must match on both sides of the boundaries. This will give an infinite number of constraint equations for each boundary. Luckily, almost all of the constants can be shown to be zero, and the existence of a degeneracy between some of the constraint equations prevents the remaining ones from being over constrained. This ultimately leads to the field solution inside the thin-shell to be

$$\begin{aligned}\phi = \phi_{\rm c} + \frac{a^2\beta\rho_{\rm c}}{6M_{\rm pl}}\Big\{&\left(\xi^2-\xi_{\rm c}^2\right)\left[1-P_2(\eta)\right] - 3\xi\left(\xi-\xi_{\rm c}\right)\left(\xi_{\rm c}^2-1\right)P_2(\eta) \\ &+2\xi_{\rm c}\left(\xi_{\rm c}^2-1\right)\left[Q_0(\xi)-Q_0(\xi_{\rm c})\right]\left[1-P_2(\eta)P_2(\xi)\right]\Big\},\end{aligned} \tag{1.70}$$

and the field solution in the background to be

$$\phi(\xi,\eta) = \phi_{\rm bg} - \frac{a^2\beta\rho_c}{3M_{\rm pl}}\left[\xi_0(\xi_0^2-1) - \xi_c(\xi_c^2-1)\right]\big(Q_0(\xi) - P_2(\eta)Q_2(\xi)\big). \quad (1.71)$$

As with the spherical and cylindrical cases, we end the calculation with an additional constraint on the thin-shell boundary $\xi_{\rm c}$,

$$\frac{6M_{\rm Pl}}{a^2\beta\rho_c}\phi_{\rm bg} + (\xi_c^2-1)\big\{1+2\xi_c Q_0(\xi_c)\big\} = (\xi_0^2-1)\big\{1+2\xi_0 Q_0(\xi_0)\big\}, \quad (1.72)$$

where it has been assumed that $\phi_{\rm bg} \gg \phi_{\rm c}$.

In the case of a very small thin-shell ($\delta\xi = \xi_0 - \xi_c \ll \xi_0$), the equation (1.72) simplifies to

$$\delta\xi = \frac{3M_{\rm pl}\phi_{\rm bg}}{\beta\rho_{\rm c}a^2(3\xi_0^2-1)Q_0(\xi_0)} \ll \xi_0, \quad (1.73)$$

while equation (1.71) simplifies to

$$\phi(\xi,\eta) = \phi_{\rm bg}\left(1 - \frac{Q_0(\xi) - P_2(\eta)Q_2(\xi)}{Q_0(\xi_0)}\right). \quad (1.74)$$

1.6.3 Chameleon Bounds

Looking at the background field profiles for the spherical, cylindrical, and ellipsoidal sources, as shown in equations (1.52), (1.57), and (1.71) respectively, we see that as the thickness of the thin-shell increases the gradient of the field also increases at all distances. This corresponds to the fifth force increasing as the source becomes less screened and more matter contributes to the force. Despite this screening mechanism, however, various table top experiments and astrophysical observations have constrained the model's parameter space. The strongest of these bounds, at time of writing, are shown in Figure 1.1.

Atom Interferometry

In these experiments laser pulses are used to place a vertical beam of cold atoms into a quantum superposition, with the different states possessing different momentum and therefore reaching a different maximum height. Later in their trajectories a series of lasers are used to merge the particle beams so that any phase shifts resulting from their different paths can be measured. As mentioned in section 1.5, a conformal field, such as the chameleon, does not couple to relativistic (traceless) particles. Since the beam is made of cold atoms and not photons, as is the case in regular interferometry experiments, the beam will be sensitive to the effects of the chameleon. Therefore, the phase shift between the beam paths is used as a measure of the difference in gravitation forces between the paths. This result can then be compared to the value predicted by GR and therefore constrain the strength of any fifth forces. This method is especially useful for probing models with screening mechanisms, such as the chameleon, since individual particles can be unscreened and so the fifth force will not be suppressed. Typical values for the size and density of the vacuum and materials involved can be seen in Table 1.1 [27, 28]. In Ref. [29] anomalous accelerations, possibly due to a fifth force, were not detected with an upper-bound of 50 nm/s^2, placing an upper bound on the strength of any fifth forces, chameleon or otherwise.

Torsion Balance

The WEP is a fundamental property of GR, and as discussed in section 1.6.1 can be violated in scalar-tensor theories with a screening mechanism,

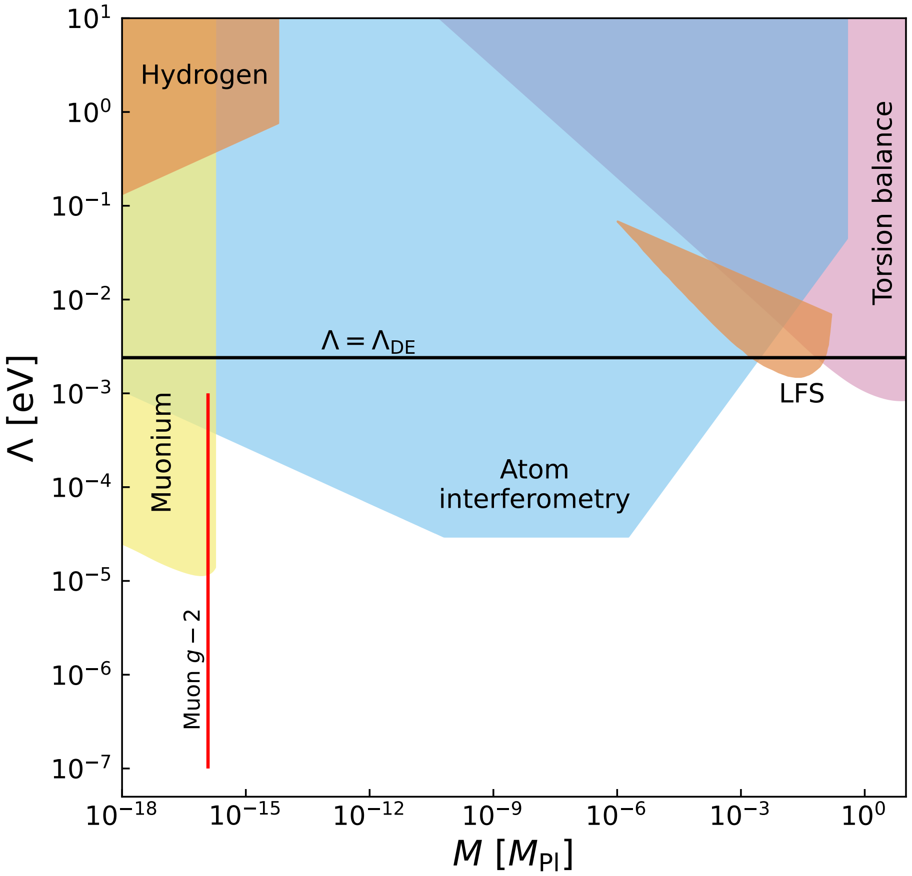

Figure 1.1: The current constraints (shaded regions) on the parameter space of the chameleon model with a $V(\phi) = \Lambda^5/\phi$ potential. $M = M_{\rm pl}/\beta$ controls the strength of the coupling to matter and Λ is the strength of the self-interactions of the scalar field. The black line indicates where Λ is equal to the dark energy value, $\Lambda_{\rm DE} = 2.4$ meV. The red line indicates where the chameleon can explain the difference in the measured and theoretical values of the muon $g-2$ value [70]. LFS stands for Levitated Force Sensor. Figure reproduced with permission from Ref. [24].

	radial (cm)	density (g/cm^3)
source mass (aluminium)	0.95	2.7
vacuum	5	6.6×10^{-17}
vacuum chamber outer wall	~ 7	7

Table 1.1: Typical values for the radial size and density of the source mass, vacuum, and chamber outer wall for an atom interferometry experiment, as depicted in Refs. [27, 28]. The wall thickness is the difference between the vacuum and vacuum chamber outer wall radii.

such as the chameleon. Torsion balance experiments therefore constrain models such as the chameleon by probing for violations in the WEP. In Ref. [71], this was accomplished by using an I-shaped pendulum with tungsten masses at both ends, suspended across from a rotating disk holding ‘attractor masses’ that alternate between tungsten and glass. The result is that in a purely Newtonian universe, the forces of attraction at both ends of the suspended pendulum would cancel out resulting in zero torque. However, since the alternating attractor masses possess different densities, the chameleon will have different minima in the two materials, and subsequently the fifth force will differ depending on the attractor mass. This will then result in a net torque that can be measured. The resulting constraints on the $n = 1$ chameleon model from this experiment are plotted in Figure 1.1.

Levitated Force Sensor

Until recently, there was still a region of parameter space for the $n = 1$ chameleon model that was not ruled out where the field had a self-coupling strength equal to the dark energy scale. However, this last part has recently been ruled out using a levitated force sensor [25]. How this setup works is a magnetically levitating plate is held inside a vacuum chamber, separated from the source masses by a thin film. These source masses are thin plates, positioned at the edge of a wheel. As the wheel rotates this will induce an attractive force with oscillating magnitude on the levitating plate. The frequency of the rotating source mass plates was set to equal the resonance frequency of the force sensor along the z-direction. The constraints from this experiment on the parameter space of the $n = 1$ chameleon model are labelled as LFS in Figure 1.1.

1.7 Outline

Chapter 2 of this thesis introduces the software package SELCIE, which was designed to solve for the chameleon field profile of arbitrarily complex physical systems. The topic of chapter 3 then covers my research into optimising vacuum chamber experiments by combining SELCIE with a genetic algorithm. Finally, in chapter 4 I review when the analytic solutions for NFW and cosmic void density profiles break down.

I begin with section 2.1, where I introduce the rescaled parameters and equations that will be used throughout this thesis.

In section 2.2 I introduce the finite element method. I outline the equations that define finite element method and illustrate how it can be equated a problem defined over a non-uniform mesh to a problem of matrix multiplication.

In section 2.3 I describe the Picard and Newton nonlinear solving methods. I show how these methods can be applied to a problem defined by the finite element method. I then go on to discussing preconditioners and show how different ones scale with the number of cells in a mesh.

Section 2.4 regards the applications of SELCIE. I will discuss how a user can use SELCIE to generate a mesh, and how a 3D system can be described using a 2D mesh through the inclusion of symmetry factors. I then analyse the chameleon field profile calculated by SELCIE for a torus inside a vacuum chamber. I compared the residual of the components of the field's equation of motion to the expected error due to machine precision and found that the residual was in acceptable bounds. I also compared solutions calculated from a 2D and 3D mesh to confirm the effectiveness of the symmetry factors. The relative error was sufficiently small everywhere except at the boundaries, where the error was likely due to the amount of refinement on the 3D mesh.

In section 2.5 I go through several examples of analytic and numerically calculated solutions to the chameleon field found in the literature. I then compare the results obtained from SELCIE for these systems and compare them to the solution from the literature.

I then conclude chapter 2 with a comment on the outlook of the SELCIE code in section 2.6.

In section 3.1 I expanded upon the large-α regime first introduced in section 2.5. I show that in this regime the shape dependence of the field solutions can be separated from the model parameters.

The details of the genetic algorithm will be explained in section 3.2.

In section 3.3 I defined various shape parameterisations. I also discussed the behaviour of the chameleon around an ellipsoidal source and commented on the appearance of a critical volume which maximises the chameleon's fifth force, given a fixed eccentricity. For the other shapes investigated, I have commented on the shapes returned by the genetic algorithm, and the apparent convergent evolution towards a general optimal solution.

Throughout this chapter the chameleon fifth force was measured at a fixed distance to the source mass. In sections 3.4 I investigate the effect varying the measuring distance has on the optimal shapes outputted by the genetic algorithm.

In section 3.5 I show how the optimal shape varies when changing the chameleon's bare potential and comment on what the common features tell us about optimising the fifth force through the shape of the source mass.

I conclude chapter 3 in 3.6, with a discussion on the applicability of the optimisation method developed in this work and on the results from this chapter more generally.

In chapter 4 I discuss some of my contributions to the papers Ref. [2] and Ref. [3]. Specifically, I review the calculation that determines when the tracing solution of the scalar field breaks down in systems with a continuous density profile. I then apply this calculation to NFW and cosmic void profiles.

I will then conclude this work in chapter 5.

Chapter 2

SELCIE: A tool for investigating the chameleon field of arbitrary sources

In section 1.6.2, I discussed the difficulty of solving the chameleon equation of motion, equation (1.45), and gave some examples from the literature of approximate analytic solutions for highly symmetric source shapes. However, even for this small subset of possible source shapes we see that the strength of the fifth force can vary depending on the matter configuration. To compare screened scalar theories with experimental and observational tests, and to optimise these searches, we need the ability to determine the scalar field profiles and corresponding fifth forces for arbitrary sources. It is for this reason I developed SELCIE[1].

SELCIE (Screening Equations Linearly Constructed and Iteratively Evaluated) is a software package that provides the user with tools to investigate nonlinear scalar field models such as the symmetron and chameleon in

---

[1] Code available at `https://github.com/C-Briddon/SELCIE.git`.

user defined systems such as an irregularly shaped source inside a vacuum chamber, galaxy clusters, etc. To accomplish this SELCIE uses a nonlinear solving method (either the Picard or Newton method [72]) with the finite element method (FEM) via the software package FEniCS [73, 74, 75, 76]. Through the FEM the field equations can be solved over irregularly spaced meshes. This allows the use of meshes that are more refined in regions where the field variation is largest, allowing us to solve the equations to a greater degree of accuracy with less computing time. Tools to easily construct and optimise these meshes are also provided in SELCIE, using the mesh generating software GMSH [77]. From the calculated field solutions, SELCIE can determine the strength of the corresponding fifth force that would be experienced by test particles.

This is not the first time the FEM, or meshes tailored to experimental configurations, have been used to determine the behaviour of screened scalar fields. A similar approach to solving screened equations of motion using the FEM was recently taken in Ref. [78], and this has been used to investigate the existence of screening in UV complete Galileon models [79]. The behaviour of chameleon and symmetron fields inside an experimental chamber has been studied using finite difference and finite element techniques, in Ref. [25, 28, 80] leading to new bounds on the parameters of the theory [29]. In Ref. [22] the symmetron equations of motion were solved for the experimental set-ups used to search for Casimir forces. Currently SELCIE is configured to find solutions for the chameleon equation of motion; however, in principle the methodology used can be generalized to other scalar fields.

In this chapter I will demonstrate the effectiveness of SELCIE in solving the chameleon equation of motion in a variety of different scenarios. I will start in section 2.1 by showing how the chameleon's equation of motion, equation (1.45), can be rescaled for ease of numerical solving. In section 2.2 I introduce the FEM, followed in section 2.3 by a description of the nonlinear solving methods that SELCIE uses. Section 2.4 describes the application of SELCIE and section 2.5 describes how its results compare to existing results. Finally, I conclude with a summary of the results and will briefly discuss the future of SELCIE.

2.1 A Rescaled Chameleon Field

The aim of this work is to solve the chameleon's equation of motion for arbitrary systems using numerical methods. To simplify the computations I worked using a dimensionless form of the chameleon's equation of motion shown in equation (1.45). To derive this new form I rescaled the density and scalar field as $\hat{\rho} = \rho/\rho_0$ and $\hat{\phi} = \phi/\phi_0$, where ρ_0 is a density scale, typically the density of the background inside the vacuum chamber hence referred to as the vacuum density, and ϕ_0 is simply equation (1.47) evaluated at $\rho = \rho_0$. Spatial distances are rescaled with respect to an arbitrary length scale L, meaning the Laplacian rescales as $\hat{\nabla}^2 = L^2\nabla^2$. Although this length is arbitrary, in practise it is useful to take it to be the characteristic length of the system, such as the vacuum chamber radius. Substituting these dimensionless parameters into equation (1.45), and using equation (1.47) to relate ρ_0 to ϕ_0, we get that the dimensionless chameleon equation is

$$\alpha\hat{\nabla}^2\hat{\phi} = -\hat{\phi}^{-(n+1)} + \hat{\rho}, \tag{2.1}$$

where I have assumed a static field, and introduced the dimensionless constant α which is defined as

$$\alpha \equiv \left(\frac{M_{\rm pl}\Lambda}{L^2\beta\rho_0}\right)\left(\frac{nM_{\rm pl}\Lambda^3}{\beta\rho_0}\right)^{\frac{1}{n+1}}. \tag{2.2}$$

In this dimensionless rescaling, the minimum of the effective potential and the Compton wavelength of fluctuations around this minimum have the simpler forms,

$$\hat{\phi}_{\rm min}(\hat{\rho}) = \hat{\rho}^{-\frac{1}{n+1}}, \tag{2.3}$$

and

$$\hat{\lambda}^2(\hat{\rho}) = \frac{\alpha}{(n+1)}\hat{\rho}^{-\frac{n+2}{n+1}}, \tag{2.4}$$

respectively, where $\hat{\lambda} = \lambda/L$ is the rescaled Compton wavelength. Note that if ρ_0 is taken to be the vacuum density, then we see that α is related to the field's vacuum Compton wavelength, $\hat{\lambda}_0$, by the expression

$$\alpha = (n+1)\hat{\lambda}_0^2. \tag{2.5}$$

The magnitude of the fifth force experienced by an unscreened test particle, equation (1.42), in these rescaled units is

$$\frac{|\vec{F}_\phi|}{|\vec{F}_{\rm g}|} = \left(\frac{\beta\phi_0}{LM_{\rm pl}|\vec{a}_{\rm g}|}\right)|\hat{\nabla}\hat{\phi}|, \tag{2.6}$$

where I have also rescaled the force by the magnitude of the gravitational force $\vec{F}_{\rm g}$ which is related to the gravitational acceleration by $\vec{F}_{\rm g} = m\vec{a}_{\rm g}$. Therefore, for fixed model parameters, by maximising the rescaled field gradient magnitude, $|\hat{\nabla}\hat{\phi}|$, we will also be maximising the corresponding fifth force.

Through this rescaling the field is now a function of only three variables

(α, n and $\hat{\rho}$). The definition of α also makes it simple to discern the degeneracies of any particular model. In other words, when solving $\hat{\phi}$ for some value of α, that solution is also valid for all combinations of Λ, β, ρ_0 and L that produce the same α-value. A similar approach to utilising degeneracies in the chameleon model was taken in Ref. [30].

2.2 Finite Element Method

As discussed in section 2, I intended to solve for the chameleon field profile around matter distributions with complicated shapes. To do this I used the FEM to solve the chameleon equation of motion shown in equation (2.1). Because of the ease in which this method can be adapted to arbitrary meshes, this allows us to adjust the mesh to any arbitrary source shape, and to add additional refinement where necessary. For example, for sources where the chameleon field profile exhibits the thin-shell effect, much of the variation in the field occurs at the boundaries of the dense regions. I can add additional refinement to the mesh in these regions, and make the mesh in other regions coarser to reduce computation cost whilst not sacrificing the accuracy of the solution. To perform the FEM calculations I use the FEniCS software package [73, 74, 75, 76]. In this section I introduce the FEM, and its application to solving the chameleon equation of motion. For a more detailed introduction to the FEM I refer the reader to Ref. [81].

In the FEM the domain of the problem, Ω, is segmented into cells, whose boundaries are defined by their vertices, P_i. The value of the field inside each cell is approximated by a piecewise polynomial function that matches the field values at each of the cell's vertices [82]. Extending this to the whole domain, the field, $u(\underline{x})$, can be defined using the basis functions

$e_i(\underline{x})$ as

$$u(\underline{x}) = \sum_i U_i e_i(\underline{x}), \tag{2.7}$$

where $U_i = U(P_i)$. In this setup, e_i is defined such that $e_i(P_j) = \delta_{ij}$ and between vertices e_i is only nonzero in cells containing the corresponding vertex P_i [83].

The FEM is designed to solve second order PDEs of the form $\nabla^2 u\left(\underline{x}\right) = -f\left(\underline{x}\right)$, with boundary conditions $u(\underline{x}) = u_0(\underline{x})$ applied to the edge of the domain, $\partial\Omega$ [82]. This is done by first transforming the second order equation into the integral of a first order equation using Green's theorem,

$$\int_\Omega \left(\nabla^2 u\right) v_j d\vec{x} + \int_\Omega \nabla u \cdot \nabla v_j d\vec{x} = \int_{\partial\Omega} \left(\partial_n u\right) v_j ds, \tag{2.8}$$

where $\partial_n u$ is the gradient of the field perpendicular to $\partial\Omega$. The functions v_j are continuous test functions, chosen from the Sobolev function space by FEniCS, which vanish on $\partial\Omega$ for all j [81, 82]. As a result of this choice $\partial_n u = 0$ and the boundary term in equation (2.8) vanishes. Applying this boundary condition and substituting in the form of the second order PDE gives the relation

$$\int_\Omega \nabla u \cdot \nabla v_j d\vec{x} = \int_\Omega f(\underline{x}) v_j d\vec{x}. \tag{2.9}$$

Decomposing the field u as in equation (2.7) we find

$$\sum_i \left(\int_\Omega \nabla e_i \cdot \nabla v_j d\vec{x} \right) U_i = \int_\Omega f(\underline{x}) v_j d\vec{x}, \tag{2.10}$$

which can be rewritten explicitly as a linear matrix relation,

$$\mathbf{MU} = \mathbf{b}, \tag{2.11}$$

where $\mathbf{U}$ is a vector with elements U_i and the matrix $\mathbf{M}$ and vector $\mathbf{b}$ are defined to be

$$\mathbf{M}_{ij} = \int_\Omega \nabla e_i \cdot \nabla v_j d\vec{x}, \tag{2.12}$$

$$\mathbf{b}_j = \int_\Omega f(\underline{x}) v_j d\vec{x}. \tag{2.13}$$

The vector $\mathbf{U}$ can therefore be determined by inverting $\mathbf{M}$. The calculation of the inverse is made easier by the fact that the e_i are only nonzero for cells that contain the vertex P_i, and so $\mathbf{M}$ is a sparse matrix [83]. Additionally, while the original Poisson equation would generally require two sets of boundary conditions to obtain a unique solution, the Lax-Milgram Theorem [84] gives the conditions required for equation (2.9) such that it has a unique solution. This enables FEniCS to obtain a unique solution for $\mathbf{U}$ using less than two bouindary conditions [74].

2.3 Nonlinear Solvers

Integrating the chameleon equation of motion, equation (2.1), as described in the previous section, we find the integral form of the equation of motion:

$$\alpha \int_\Omega \hat{\nabla}\hat{\phi} \cdot \hat{\nabla} v_j d\vec{x} = \int_\Omega \hat{\phi}^{-(n+1)} v_j d\vec{x} - \int_\Omega \hat{\rho} v_j d\vec{x}. \tag{2.14}$$

This equation is nonlinear in $\hat{\phi}$, and so a nonlinear solving method is required to compute the solution. SELCIE has two inbuilt solvers of this form, the Picard and Newton iterative solving methods. In the following subsections I outline how these solvers work and their performance. For a full discussion of these methods and proof of their validity I refer the reader to Ref. [72].

2.3.1 Picard Method

In the Picard method I take the Taylor series expansion of the potential term around some field $\hat{\phi}_k$ which is the k^{th} estimate of the field,

$$\begin{aligned} \hat{\phi}^{-(n+1)} &\approx \hat{\phi}_k^{-(n+1)} - (n+1)\hat{\phi}_k^{-(n+2)}(\hat{\phi} - \hat{\phi}_k) + \mathcal{O}(\hat{\phi} - \hat{\phi}_k)^2 \\ &\approx (n+2)\hat{\phi}_k^{-(n+1)} - (n+1)\hat{\phi}_k^{-(n+2)}\hat{\phi} + \mathcal{O}(\hat{\phi} - \hat{\phi}_k)^2. \end{aligned} \tag{2.15}$$

Neglecting higher order terms and substituting the expansion in equation (2.15) into equation (2.14) gives the following equation for $\hat{\phi}$:

$$\alpha \int_\Omega \hat{\nabla}\hat{\phi}\cdot\hat{\nabla}v_j d\vec{x} + (n+1)\int_\Omega \hat{\phi}_k^{-(n+2)}\hat{\phi}v_j d\vec{x} = (n+2)\int_\Omega \hat{\phi}_k^{-(n+1)}v_j d\vec{x} - \int_\Omega \hat{\rho}v_j d\vec{x}, \tag{2.16}$$

where I have rearranged terms so that the left-hand side of Equation (2.16) is bi-linear in $\hat{\phi}$ and v_j, and the right-hand side is linear in v_j [82]. With the equation in this form, FEniCS can then be used to solve for the field $\hat{\phi}$. I iterate this procedure by setting $\hat{\phi}_{k+1} = \hat{\phi}$ and then re-solving equation (2.16) to find a new $\hat{\phi}$. I then repeat this process iteratively updating the value $\hat{\phi}_k$ each time until the condition $|\hat{\phi}_{k+1} - \hat{\phi}_k| < \delta$, where δ is the tolerance, is satisfied at all vertices.

A downside of the Picard method outlined above is that the process gives no control over the rate of change of $\hat{\phi}$ between iterations and by extension the stability of the convergence. To address this I introduce a relaxation parameter, ω, and a new update procedure so that

$$\hat{\phi}_{k+1} = \omega\hat{\phi} + (1-\omega)\hat{\phi}_k. \tag{2.17}$$

By decreasing the parameter ω, the solver takes smaller step sizes between values and as such is less likely to overshoot the true solution and diverge.

However, smaller step sizes also mean that the solver will take longer to converge. Therefore, some care is needed in the choice of ω.

As discussed in section 2.2, the FEM calculation can be expressed as a linear equation for a vector whose elements are the values of the field at each vertex. Writing equation (2.16) in this form gives

$$\left[\alpha\mathbf{M} + (n+1)\mathbf{B}_k\right]\hat{\mathbf{\Phi}} = (n+2)\mathbf{C}_k - \hat{\mathbf{P}}, \tag{2.18}$$

where $\hat{\mathbf{\Phi}}$ is the vector whose elements are the values of the field $\hat{\phi}$ at each of the mesh vertices. Here $\mathbf{M}$ is defined as in equation (2.12), while the matrices $\mathbf{B}_k$ and $\mathbf{C}_k$ are defined as

$$[\mathbf{B}_k]_{ij} = \int_\Omega \hat{\phi}_k^{-(n+2)} e_i v_j d\vec{x}, \tag{2.19}$$

$$[\mathbf{C}_k]_j = \int_\Omega \hat{\phi}_k^{-(n+1)} v_j d\vec{x}, \tag{2.20}$$

and e_i are the basis functions of the field. The density vector $\hat{\mathbf{P}}$ is defined as

$$\hat{\mathbf{P}}_i = \int_\Omega \hat{\rho}(x) v_i d\vec{x}, \tag{2.21}$$

which is calculated alongside $\mathbf{B}_k$ and $\mathbf{C}_k$ using FEniCS[2]. The advantage of solving the problem in the form of equation (2.18) is that since $\mathbf{M}$ and $\hat{\mathbf{P}}$ do not depend on $\hat{\phi}_k$ these can be computed once, before the iterative solver, thereby reducing the total amount of computing required.

---

[2] The computational cost for computing these vectors and matrices will depend on the number of vertices in the mesh.

2.3.2 Newton Method

The FEM Newton iterative method solves equations of the form $F(\hat{\phi}; v_j) = 0$, by evaluating the linear problem

$$\sum_{i=1}^{N} \frac{\partial F}{\partial \hat{\phi}_i} \delta \hat{\phi}_i = -F(\hat{\phi}_k; v_j), \tag{2.22}$$

where $\hat{\phi}_k$ is the k^{th} estimate of the field, as was the case in the Picard method, and $\delta\hat{\phi}_i$ are the elements of a correction field $\delta\hat{\phi}$ which has the same basis functions as $\hat{\phi}$ [82]. The components of the field $\hat{\phi}_k$ are then updated as

$$\hat{\phi}_{k+1} = \hat{\phi}_k + \omega \delta \hat{\phi}, \tag{2.23}$$

where again ω is a relaxation parameter. The code terminates when $|\delta\hat{\phi}| < \delta$ at all vertices, where again δ is the tolerance. For the chameleon field, I want the field $\hat{\phi}$ to satisfy

$$F(\hat{\phi}; v_j) = \alpha \int_\Omega \hat{\nabla}\hat{\phi} \cdot \hat{\nabla} v_j d\vec{x} + \int_\Omega \hat{\rho} v_j d\vec{x} - \int_\Omega \hat{\phi}^{-(n+1)} v_j d\vec{x} = 0. \tag{2.24}$$

Therefore, equation (2.22) becomes

$$\begin{aligned} \alpha \int_\Omega \hat{\nabla}\delta\hat{\phi} \cdot \hat{\nabla} v_j d\vec{x} + (n+1) \int_\Omega \hat{\phi}_k^{-(n+2)} \delta\hat{\phi} v_j d\vec{x} \\ = -\alpha \int_\Omega \hat{\nabla}\hat{\phi}_k \cdot \hat{\nabla} v_j d\vec{x} - \int_\Omega \hat{\rho} v_j d\vec{x} + \int_\Omega \hat{\phi}_k^{-(n+1)} v_j d\vec{x}. \end{aligned} \tag{2.25}$$

In matrix form the equation to be solved at each iteration is

$$[\alpha \mathbf{M} + (n+1)\mathbf{B}_k]\delta\hat{\mathbf{\Phi}} = -\alpha \mathbf{M} \hat{\mathbf{\Phi}}_k - \hat{\mathbf{P}} + \mathbf{C}_k, \tag{2.26}$$

where $\delta\hat{\mathbf{\Phi}}$ and $\hat{\mathbf{\Phi}}_k$ are the vector forms of $\delta\hat{\phi}$ and $\hat{\phi}_k$ respectively. The matrices $\mathbf{M}$, $\mathbf{B}$, $\mathbf{C}$ and $\hat{\mathbf{P}}$ are defined in equations (2.12) and (2.19)-(2.21) respectively. As was the case with the Picard method, I can compute $\mathbf{M}$ and $\hat{\mathbf{P}}$ prior to the iterative solver to reduce computation time.

2.3.3 Optimising Solvers

Regardless of whether the Picard or Newton solver is chosen, when solving for $\hat{\phi}_k$ or $\delta\hat{\phi}$ in equations (2.18) and (2.26) respectively, at each step it is necessary to solve a *linear* system of the form $\mathbf{Ax} = \mathbf{b}$. For large matrices $\mathbf{A}$, direct substitution is impractical, so iterative methods are required, which can be further classified into stationary and Krylov subspace methods. Stationary methods apply an operator to the residual error from some initial estimate of $\mathbf{x}$ through, for example, splitting of the matrix $\mathbf{A}$. Krylov methods work by forming a set of basis functions with successive powers of $\mathbf{A}$ applied to the residual, and are guaranteed to converge (although this may be slow for large systems). The archetypal example of a Krylov solver is the conjugate gradient (CG) method, which is suitable for symmetric positive-definitive $\mathbf{A}$. Due to the construction of the test and trial functions, the matrices in equations (2.18) and (2.26) always satisfy this property [82]. The convergence of both types of iterative methods can be improved by preconditioning with a matrix $\mathbf{K}$. This involves solving the system $\mathbf{K}^{-1}\mathbf{Ax} = \mathbf{K}^{-1}\mathbf{b}$, where $\mathbf{K}$ is chosen such that the spectrum of eigenvalues of $\mathbf{K}^{-1}\mathbf{A}$ is close to 1, and $\mathbf{K}^{-1}\mathbf{b}$ is inexpensive to evaluate. The simplest type of preconditioner is the Jacobi (or diagonal) preconditioner, where $\mathbf{K} = \operatorname{diag}(\mathbf{A})$.

To determine the optimal choice of nonlinear method, linear solver and preconditioner, I tested various combinations against meshes of varying cell number for a 2D spherical source inside a vacuum chamber. In total, I investigated 6 nonlinear methods: (1) Newton; (2) Picard; (3) Newton with pre-calculated system matrices; (4) Picard with pre-calculated system matrices; (5) the inbuilt FEniCS Newton solver; (6) the inbuilt FEniCS SNES (Scalable Nonlinear Equations Solvers). For each of these I tested 10 linear solvers and 11 preconditioners included in FEniCS, giving a total of 660 solver combinations. Some of these either did not work together or converge, so were excluded from the analysis. The results are summarised in Figure 2.1, which shows the total run-time against cell number for each nonlinear method. In each case, I show the best combination of linear solver and preconditioner. From this, we see that the matrix form of the Picard method is both the fastest and also scales better with mesh size. In this case, the optimal combination was found to be the CG solver with Jacobi preconditioner. To check this generalised to other systems, I evaluated the solution time of the linear system for a variety of source shapes, and found only small differences. The combination of matrix Picard and CG solver with Jacobi preconditioner is therefore the default choice in SELCIE.

2.4 Using SELCIE

In this section I will illustrate the typical work flow of a SELCIE user.

2.4.1 Mesh Generating Tools

I begin by determining the spatial regions within which I wish to solve the chameleon equations of motion, and covering them with an array of points defining a mesh. SELCIE is equipped with tools to help the user construct meshes using the GMSH software [77]. One possibility is to use the functions built into SELCIE to generate basis shapes such as ellipses and rectangles. These shapes can then be rotated, translated, combined or

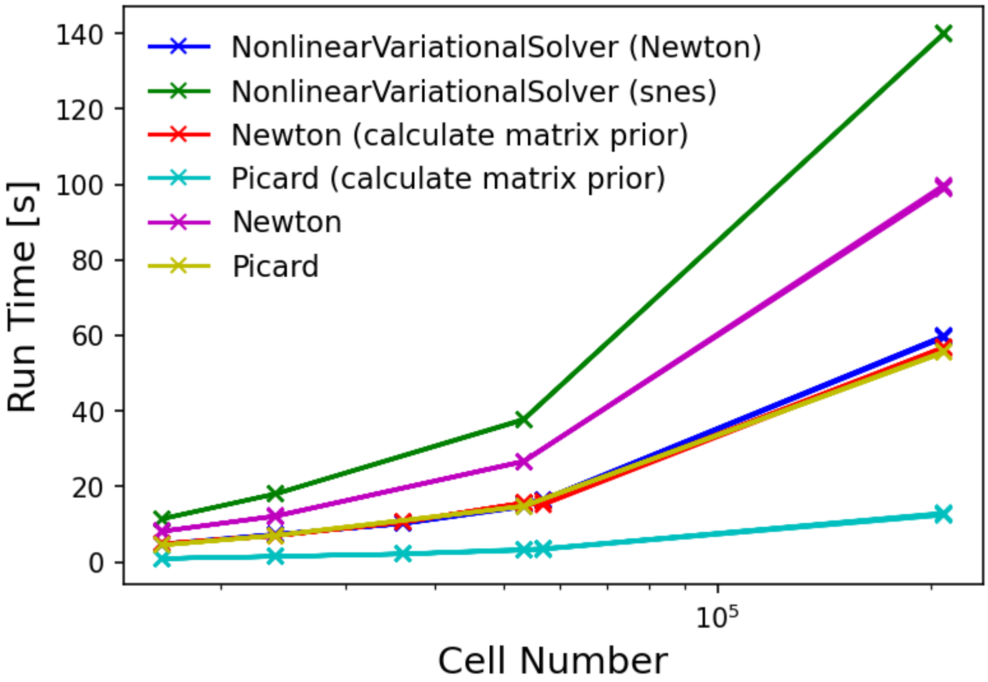

Figure 2.1: Plot showing how the optimum linear solver and preconditioner combinations for various nonlinear solving methods scale with mesh cell number for a 2D spherical source inside a vacuum chamber.

subtracted from one another to produce new, more complex shapes. An example of a complex shape constructed in this manner is shown in Figure 2.2a. Alternatively, it may be that the desired mesh shape is defined by a known function. In that case, SELCIE can construct the mesh directly from a list of points obtained from the function that defines the closed surface of the shape. Figure 2.2b is an example of a mesh constructed using this method. These tools, either used separately or in combination, allow the user to construct a vast range of shapes without prerequisite knowledge of the GMSH interface. These shapes can also be made into subdomains of a larger mesh which can be used to evaluate the field.

A major benefit to the finite element method is the ability to use non-uniform meshes. This can be especially useful with screened scalar field models where the field may vary more significantly in some regions of space than others. As such, SELCIE gives the user control over the size of indi-

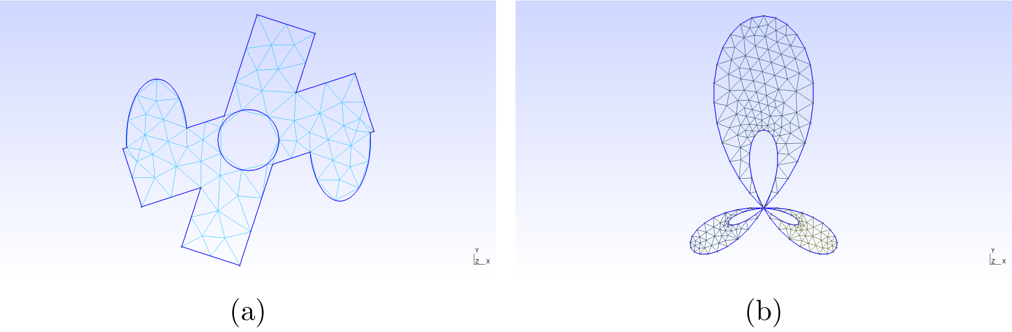
(a) (b)

Figure 2.2: GMSH meshes constructed using: **a)** a combination of functions manipulating rectangles and ellipses into a complex shape. **b)** A mesh of a shape obtained from a series of Legendre polynomials with coefficients [0.0547, 0.0013, 0.0567, 0.2627], constructed using the $points\_to\_surface()$ function.

vidual cells as a function of distance from the boundaries. This can be done by defining some range for which the cell size will vary linearly between some given minimum and maximum. Once generated the mesh is saved as a $.msh$ file.

2.4.2 Dimensional Reduction Through Symmetry

Solving differential equations in three spatial dimensions can be computationally expensive. To reduce the number of degrees of freedom in a given problem a symmetry can be imposed, reducing the effective dimension of the problem. When applicable, this can be done in SELCIE through the introduction of a symmetry factor, σ into the integrations,

$$\int_{\Omega} f\,(\underline{x})d\vec{x} \rightarrow \int_{\Omega/S} f\,(\underline{x})\sigma d\vec{x}. \tag{2.27}$$

where S is the symmetry group of the applied symmetry. Systems with axis symmetry around the x or y axes can be simplified to 2-dimensions using the symmetry factors $|y|$ and $|x|$ respectively. The final option built into SELCIE is a translational symmetry perpendicular to the plane of the

2D mesh which has a symmetry factor equal to 1.

2.4.3 Solving for the Field

Once the mesh has been created and saved, the user can then define the matter distribution which sources the chameleon field profile. The user can define the density profile in terms of a set of functions, each defining the density on a different subdomain of the mesh. In this way, complex density profiles can be easily constructed.

After applying the appropriate symmetry factor, the user is now free to use either the $picard()$ or $newton()$ functions to solve for the field given the density profile and a choice of the chameleon parameters n and α. It is then possible to compute the field gradient (vector or scalar magnitude).

To diagnose the accuracy of the solutions to the chameleon equation of motion obtained by SELCIE, the strong residual can be evaluated. I do this by inputting the solution obtained for the scalar field into the equation of motion, equation (2.1). The amount by which this differs from zero is the strong residual, and I say that the solutions I obtain are accurate when the strong residual is significantly smaller than the dominant term(s) in the equation of motion. As an example, Figure 2.3 shows the density profile of a torus inside a vacuum chamber, the associated chameleon field profile, the magnitude of the field gradient, and the strong residual. The equations have been solved assuming that the system is symmetric under rotations around the vertical y-axis. From Figure 2.3d it can be seen that the strong residual varies by orders of magnitude across the spatial domain. In Figure 2.4 I show the strong residual alongside the component terms of the equation of motion, along the x and y-axes. In regions of high density

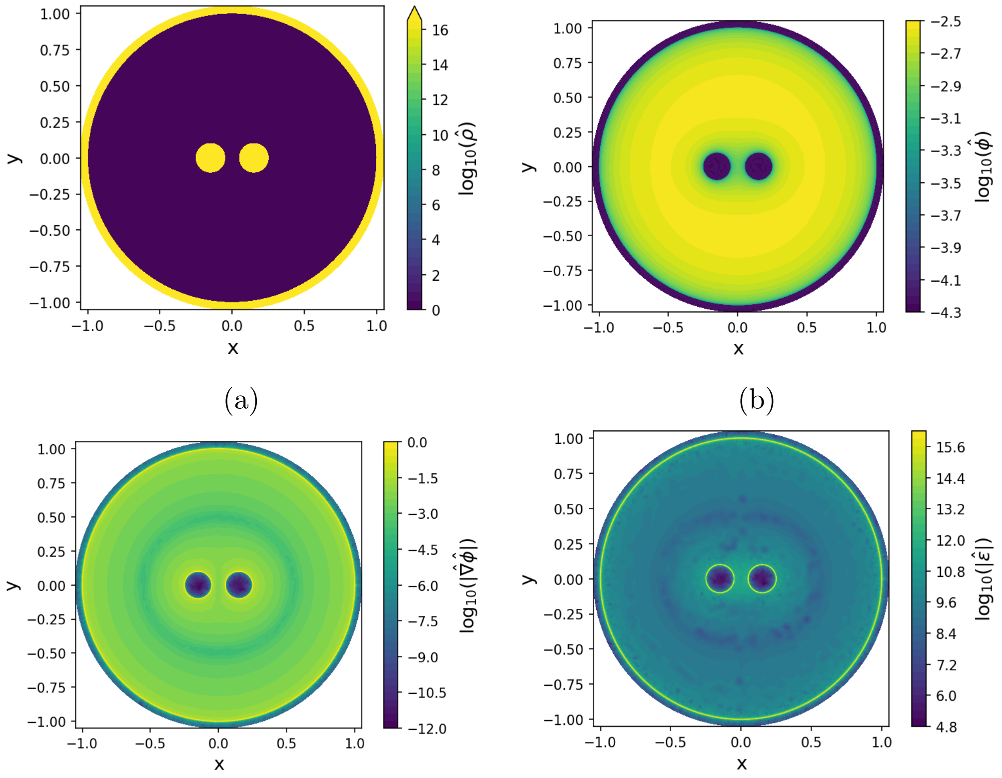

(a) (b)

(c) (d)

Figure 2.3: Calculated field results from SELCIE for an axis-symmetric system in the y-axis consisting of a torus with a hole radius of 0.05 and a tube radius of 0.1, inside a vacuum chamber of unit radius, wall thickness 0.1, and density equal to that of the torus. The chameleon parameters are $n = 3$ and $\alpha = 10^{12}$. **a)** The density profile of the system. **b)** The chameleon field profile. **c)** The magnitude of the field gradient. **d)** The strong residual of the field.

we see that the dominant terms are $\hat{\phi}^{-(n+1)}$ and $|-\hat{\rho}|$. Meanwhile, in the vacuum regions the dominant terms are $\hat{\phi}^{-(n+1)}$ and $|\alpha\nabla^2\hat{\phi}|$. Assuming that the error on the field is of machine precision, $\delta\hat{\phi} \sim 10^{-14}$, and that the field value is $\hat{\phi} \sim 10^{-4}$, this gives that the expected error of the field's bare potential $\hat{\phi}^{-(n+1)}$ is $\sim 10^{7}$. This demonstrates that the error on equation (2.1) can be very large, even at machine precision, due to the nonlinear nature of the equation. I will consider the solutions I find to be accurate if the strong residual is at least one order of magnitude smaller than the dominant terms in the equation of motion. This can be seen to be the case in Figure 2.4.

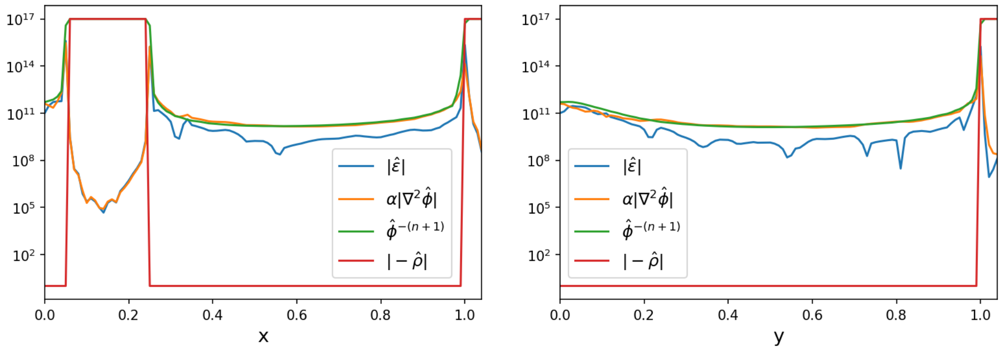

(a) (b)

Figure 2.4: Plot of the strong residual of equation (2.1) and the components of the equation of motion for a torus with hole radius 0.05 and tube radius of 0.1, inside a unit sized vacuum chamber with wall thickness 0.1 and with axis-symmetry imposed in the y-axis. The variation of the residual and the components of the equation of motion along the lines $y = 0$ and $x = 0$ are shown in Figures 2.4a and 2.4b respectively. Both the torus and the vacuum walls have a rescaled density of 10^{17} and the system the chameleon parameters used are $n = 3$ and $\alpha = 10^{12}$.

To check the accuracy of the solver in 3D, we can also solve for the chameleon field around the torus without imposing axis-symmetry. Figure 2.5 shows the maximum relative difference between the 2D and 3D solutions across a range of azimuthal angles. From these plots we see a significant relative error at the discontinuous boundaries of $\sim 60\%$. I found this to be a consequence of the 3D mesh not being sufficiently refined at the boundary. However, due to the scaling relation between boundary precision and cell number, it can quickly become a computationally expensive calculation to construct better refined meshes in 3D. Nevertheless, away from the boundaries the relative error decreases to percent levels and the two solutions have a strong agreement. This illustrates that even with a coarser boundary in 3D, SELCIE can still accurately determine the solution to the equation of motion.

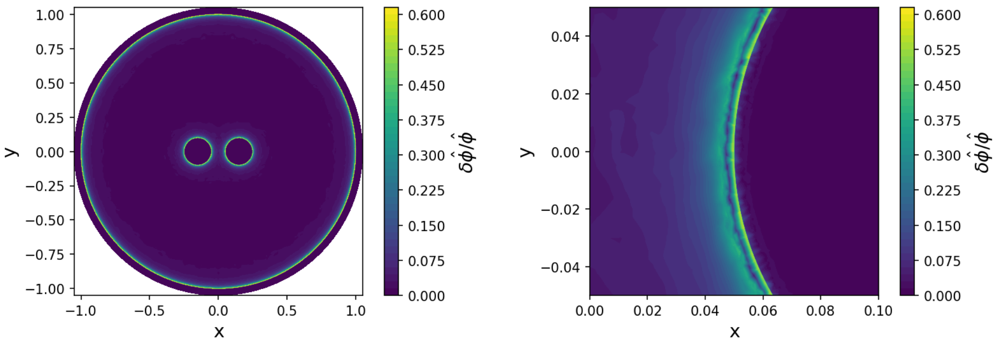

(a) (b)

Figure 2.5: Plots of the maximum relative difference between the 2D and 3D solutions of a torus inside a vacuum chamber for a range of azimuthal angles. Figure 2.5a shows the whole domain while Figure 2.5b shows a small region at the boundary of the source. The torus has a hole of radius 0.05, tube radius of 0.1 and rescaled density of 10^{17}. The chamber wall has the same density as the torus and a thickness of 0.1. Both measurements were measured using the chameleon parameters $n = 3$ and $\alpha = 10^{12}$.

2.5 Comparison with Known Field Profiles

In this section I will compare the analytic solutions to the chameleon model discussed in section 1.6.2 to the solutions numerically calculated by SELCIE. To accomplish this I will start by performing the parameter rescaling discussed in section 2.1 to obtain dimensionless forms of the analytic solutions. These can then be compared directly to the SELCIE solutions.

2.5.1 Field Maximum with No Source

I will start by considering the chameleon field profile inside an empty spherical vacuum chamber. Since I define $\hat{\rho}_0 = 1$ everywhere inside the vacuum chamber, equation (2.4) then shows that when $\alpha \gg (n+1)$ the field's vacuum Compton wavelength is many orders larger than the size of the vacuum chamber. The field, therefore, does not have enough space to reach the value that minimises the effective potential inside the chamber and I can make the approximation $\hat{\phi}^{-(n+1)} \ll \hat{\rho}$ in the vacuum region. Applying this approximation to equation (2.1) and defining a new field related to the original by the rescaling

$$\hat{\phi}(n, \hat{\rho}, \alpha) = \alpha^{-1/(n+2)}\hat{\varphi}(n, \hat{\rho}), \tag{2.28}$$

I then find that the resulting equation for $\hat{\varphi}$,

$$\hat{\nabla}^2\hat{\varphi} = -\hat{\varphi}^{-(n+1)}, \tag{2.29}$$

is independent of α. The equivalent relation for the $n = 1$ case was derived in Ref. [26].

We see that the chameleon field profiles inside an empty vacuum chamber are all equivalent up to the rescaling in equation (2.28) as long as $\alpha \gg (n + 1)$.

It was shown in Ref. [26] that when $n = 1$ the value of $\hat{\varphi}$ at the centre of an empty vacuum chamber should equal 0.69 (to two significant figures).

Figure 2.6 shows the profile of $\hat{\varphi}$ computed with SELCIE for a range of α values, all of which are much greater than unity. As predicted, $\hat{\varphi}$ has the same profile inside the vacuum for the whole range of α values tested, verifying that equation (2.29) holds. The value of $\hat{\varphi}$ at the origin was also consistent with the value found in Ref [26].

2.5.2 Solutions around Circular Sources

For ease of comparison with the results of the SELCIE code, I will express the vacuum field profiles around spherical, equation (1.54), and cylindrical, equation (1.60), sources using the dimensionless rescaled parameters discussed in section 2.1. These expressions for a sphere and cylinder re-

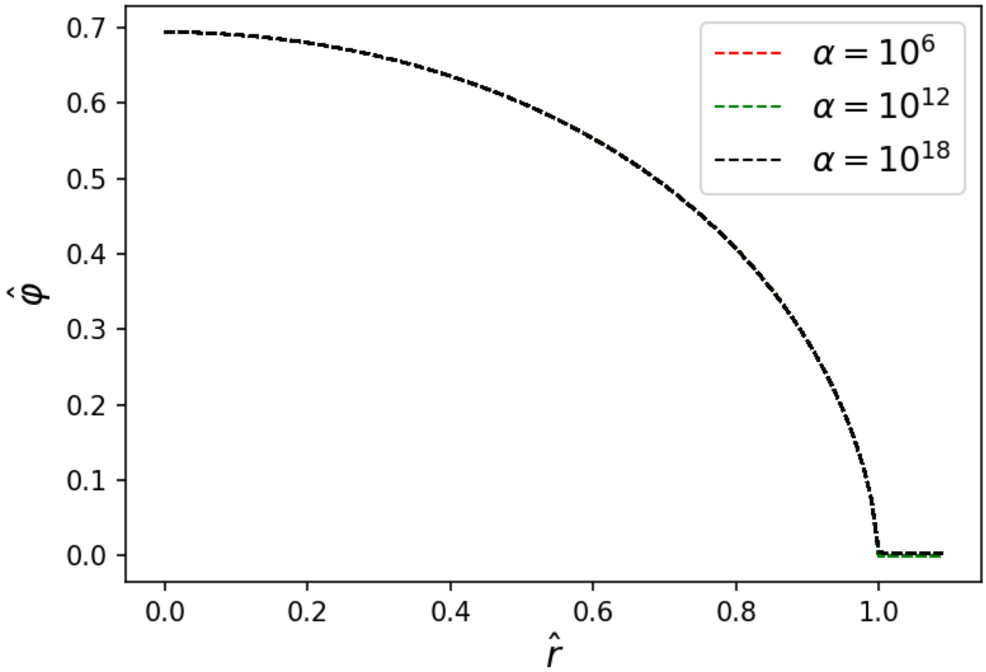

Figure 2.6: The rescaled chameleon field as described in equation (2.28) inside an empty vacuum chamber for various values of α. In each case $n = 1$ and $\hat{\rho}_\mathrm{c} = 10^{17}$. Note that, except when $\hat{r} > 1$, the three curves exactly overlap.

spectively are

$$\hat{\phi}(\hat{r}) \approx 1 - \frac{\hat{R}}{\hat{r}} e^{-(\hat{r}-\hat{R})\sqrt{\frac{(n+1)}{\alpha}}}, \tag{2.30}$$

and

$$\hat{\phi} \approx 1 - \frac{2\mathcal{K}_0\left(\hat{r}\sqrt{\frac{(n+1)}{\alpha}}\right)}{\ln\left(\frac{4\alpha}{(n+1)\hat{R}^2}\right)}, \tag{2.31}$$

both with a rescaled radius of $\hat{R}$. As stated in section 1.6, both these solutions assume $m_\mathrm{bg}R \ll 1$, which is equivalent to $(n+1)\hat{R}^2 \ll \alpha$, and that the thin-shell is very small. To determine if the latter condition is satisfied I apply the parameter rescaling to equations (1.53) and (1.73), which give the conditions for equations (2.30) and (2.31) to be valid as respectively

$$\alpha \ll \hat{\rho}_{\mathrm{c}} \hat{R}^2 \tag{2.32}$$

$$\alpha \ll \frac{1}{4} \hat{\rho}_{\mathrm{c}} \hat{R}^2 \ln \left(\frac{4\alpha}{(n+1)\hat{R}^2} \right) \tag{2.33}$$

To verify that SELCIE can reproduce these approximate analytic solutions, I constructed a 2D mesh of a circular source of radius $\hat{R} = 0.005$ inside a circular vacuum chamber of radius unity. Both spherical and cylindrical cases can be explored using the above 2D mesh by imposing axis-symmetry (along either the x or y-axis) and translational symmetry normal to the mesh, respectively. For the values of the corresponding symmetry factors see section 2.4.2. In both cases I choose $n = 1$, $\alpha = 0.1$ and the source density was set to $\hat{\rho}_{\mathrm{c}} = 10^{17}$, therefore satisfying both equation (2.32) and (2.33). The analytic and numerical field profiles for both spherical and cylindrical sources are shown in Figure 2.7. From this plot we see that SELCIE is able to reproduce the analytic results to within the accuracy of the analytic approximations.

2.5.3 Solutions around Ellipsoidal Sources

As was done for the spherical and cylindrical cases, I will be working in the regime where the thin-shell is very small, $\delta\xi = \xi_0 - \xi_c \ll \xi_0$. Applying the rescaling discussed in section 2.1 to equations (1.73) and (1.74), we obtain that when the small thin-shell condition

$$\delta\xi = \frac{3\alpha\hat{\phi}_{\mathrm{bg}}}{\hat{a}^2(3\xi_0^2 - 1)Q_0(\xi_0)} \ll \xi_0 \tag{2.34}$$

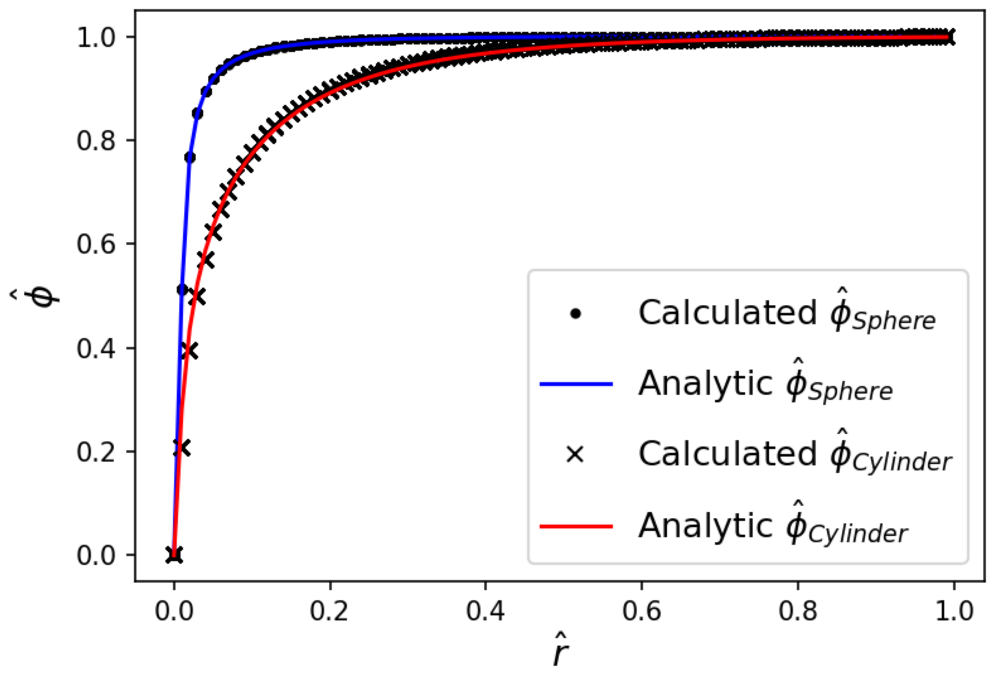

Figure 2.7: The calculated field profiles for the spherical and cylindrical cases against the approximate analytic solutions. For both cases, $n = 1$, $\alpha = 0.1$, $\hat{\rho}_{\rm c} = 10^{17}$, and the source radius was set to 0.005.

is satisfied, where $\hat{a} = a/L$, then the rescaled field profile around the ellipsoidal source is

$$\phi(\xi, \eta) = \hat{\phi}_{\rm bg}\left(1 - \frac{Q_0(\xi) - P_2(\eta)Q_2(\xi)}{Q_0(\xi_0)}\right). \tag{2.35}$$

To test this solution against the field profile found by SELCIE around an elipsoidal source, I first constructed a mesh of an ellipse inside a unit radius vacuum chamber with a wall thickness of 0.1. The value of ξ_0 for this ellipse was allowed to vary while the value of a was set such that for any ξ_0 the volume was set to that of a sphere of radius 0.005. Taking $\hat{\rho}_c = 10^{17}$, $n = 1$ and $\alpha = 10^3$ the chameleon field inside the chamber was calculated using SELCIE for various values of ξ_0. These results are compared to equation (2.35) in Figure 2.8. Close to the surface the analytic result appears to break down as the value of the field is negative. Away from the

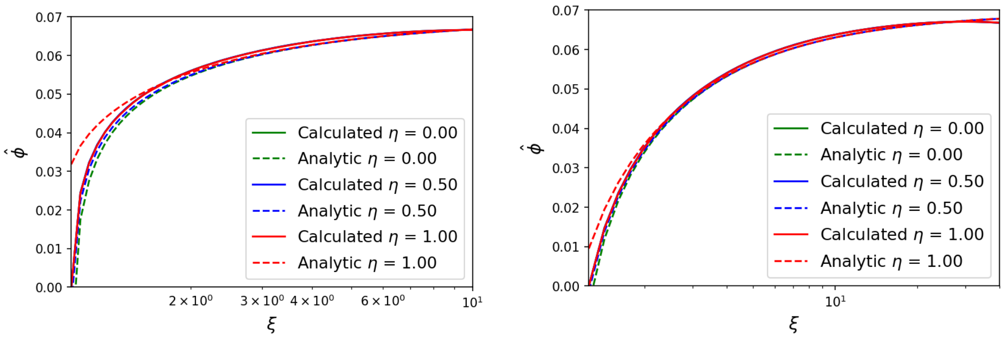

(a) $\xi_0 = 1.01$ (b) $\xi_0 = 1.25$

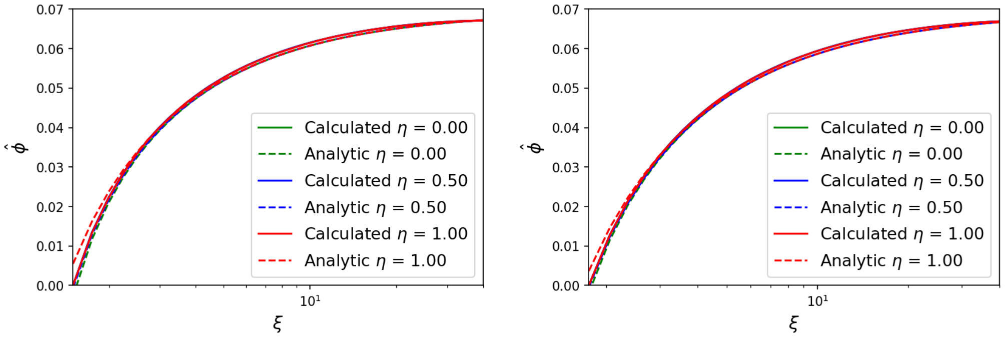

(c) $\xi_0 = 1.50$ (d) $\xi_0 = 1.75$

Figure 2.8: Comparison between the chameleon field profiles calculated by SELCIE around an elliptical source of uniform density and the approximate analytic solution shown in equation (2.35) for various values of ξ_0. The parameters used were $n = 1$ and $\alpha = 10^3$.

surface, however, the results from SELCIE agree with the analytic results with $\sim 1\%$ relative error. Given that this is only an approximate analytic solution, I consider our results to be in good agreement. Commenting on the analytic solution itself, recall that an assumption made in its derivation was that the thin-shell began at ξ_c which is independent of η. The plots shown in Figure 2.8 appear to validate this assumption; however, this is simply due to the thickness of the thin-shell being very small. If α is increased to 10^{15}, therefore increasing the Compton wavelength of the field in the source, we see from Figure 2.9 that ξ_c does depend on η.

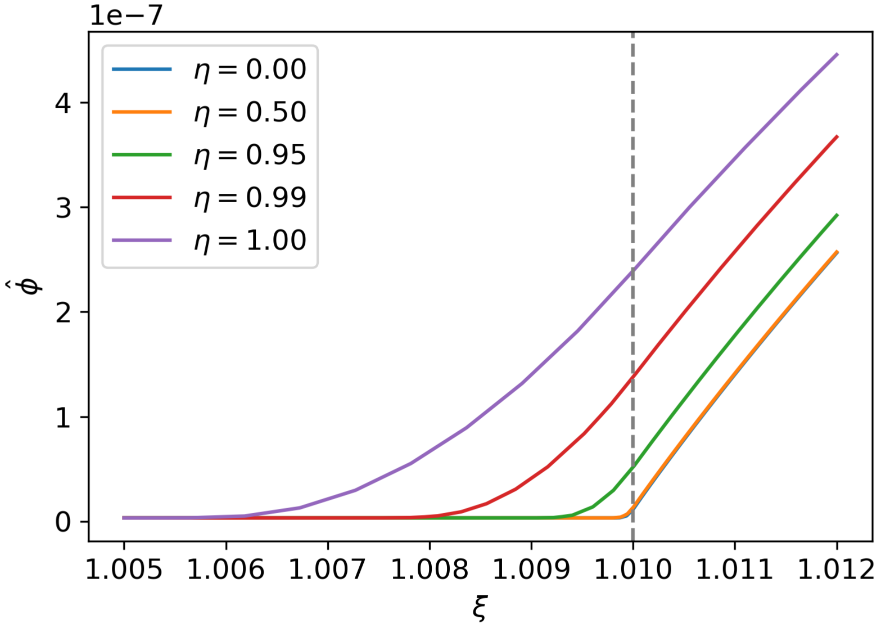

Figure 2.9: The chameleon field profiles around an ellipsoidal source inside a unit sized spherical vacuum chamber. The boundary of the ellipsoid is given by the curve of constant $\xi = 1.01$ and has equal volume to a sphere of radius $r = 0.005$. The density of the ellipsoid relative to the vacuum is 10^{17}. Each line corresponds to the field along lines of constant η. We see that the thickness of the thin-shell in ξ-coordinates is not constant in η, and is in fact thickest at the tip of the ellipsoid ($\eta = 1$).

2.5.4 Analytic solutions for NFW galaxy cluster halos

In the previous subsections I have discussed solutions to the chameleon equation of motion around dense sources, with clearly defined surfaces, inside a vacuum chamber. In this section I will demonstrate that SELCIE can also provide accurate chameleon field profiles for continuous density distributions. An important example of such a system, of relevance to a number of observational tests, is galaxy clusters. These are the largest gravitationally bound systems in the universe. The ability to measure cluster masses in a variety of ways (X-ray temperature, the Sunyaev–Zeldovich effect, weak lensing and other methods [85, 86, 87]) makes clusters invaluable when studying and testing gravity on cosmological scales. In addition, galaxy clusters are known to have a complicated density distribution, which will need to be evaluated when testing for screened models such as the chameleon. These features have been employed in astrophysical fifth force searches, producing strong constraints on chameleon gravity and other models [2, 41, 88, 89, 90, 91, 92, 93].

It has been shown that the underlying density distribution on galaxy and galaxy cluster scales is well-approximated by the Navarro–Frenk–White (NFW) profile [94]. After rescaling, this profile can be written as

$$\hat{\rho}(r) = \frac{\hat{\rho}_s}{\hat{r}\left(1+\hat{r}\right)^2}, \tag{2.36}$$

where the radial coordinate has been rescaled by the scale radius of the cluster r_s, such that $\hat{r} = r/r_s$, and the density has been rescaled by the cosmological critical density ρ_c such that $\hat{\rho} = \rho/\rho_c$ and $\hat{\rho}_s = \rho_s/\rho_c$. The NFW profile of equation (2.36) diverges as $\hat{r} \to 0$, so I also introduced a core radius, $\hat{r}_{\mathrm{cut}}$, so that $\hat{\rho}\left(\hat{r} < \hat{r}_{\mathrm{cut}}\right) = \hat{\rho}\left(\hat{r}_{\mathrm{cut}}\right)$.

There is no exact analytical solution for a chameleon field profile within and around a spherical NFW halo. However, as in the previous subsections, an approximate analytic solution can be obtained by using a piecewise approach as shown in Ref. [88]. Applying the rescaling outlined in section 2.1, this solution can be written as

$$\hat{\phi}(\hat{r}) = \begin{cases} \hat{\phi}_s \left[\hat{r}\left(1+\hat{r}\right)^2\right]^{\frac{1}{n+1}} & \hat{r} \leq \hat{r}_{\mathrm{c}} \\ \hat{\phi}_0 \left(1 - \dfrac{\hat{r}_{\mathrm{c}}}{\hat{r}}\right) + \dfrac{\hat{\rho}_s}{\alpha}\dfrac{1}{\hat{r}} \ln\left(\dfrac{1+\hat{r}_{\mathrm{c}}}{1+\hat{r}}\right) & \hat{r} \geq \hat{r}_{\mathrm{c}}, \end{cases} \tag{2.37}$$

where $\hat{\phi}_s = \hat{\phi}_{\min}(\hat{\rho}_s)$, as defined by equation (2.3), $\hat{\phi}_0$ is the field value at spatial infinity (or at the boundary of the numerical simulation), and $\hat{r}_{\mathrm{c}}$ is the transition scale such that for $r < r_{\mathrm{c}}$ the cluster is screened. For distances less than $\hat{r}_{\mathrm{c}}$ the potential and matter terms dominate over the gradient term and so the field takes the value that minimises the effective potential as given by equation (2.3). For scales larger than $\hat{r}_{\mathrm{c}}$ the field takes values away from this minimum as the potential term becomes subdominant to the gradient and matter terms. The transition scale is $\hat{r}_{\mathrm{c}} \approx (\hat{\rho}_s/\alpha\hat{\phi}_0) - 1$ where, in both this expression and equation (2.37), it has been assumed that $\hat{\rho}_s \gg 1$ and therefore $\hat{\phi}_s \ll 1$.

I compared equation (2.37) against solutions calculated using SELCIE for the cases when $\hat{r}_{\mathrm{c}}$ is much larger than the domain size and for $\hat{r}_{\mathrm{c}} \ll 1$. These results are plotted in Figure 2.10. In both cases the calculated and analytic results have a strong agreement, with sub-percentage relative error. However, I should mention here that due to the before mentioned cutoff that was introduced to the density profile, the assumption that the field traces the minimum of the effective potential near the origin can be broken. This can be seen in Figure 2.10b where the analytic solution predicts the

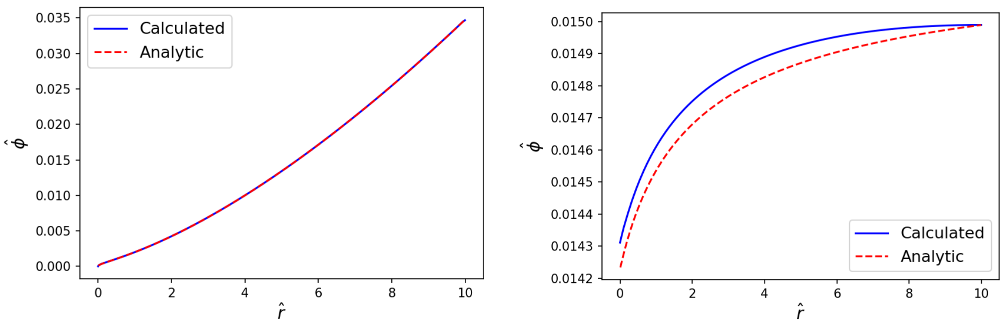

(a) (b)

Figure 2.10: Plots comparing the field profile calculated by SELCIE with the expected analytic solution in the regime: **a)** $r_c \gg 1$ ($\alpha = 10^{-9}$), **b)** $r_c \ll 1$ ($\alpha = 10^{9}$). In both cases the rescaled critical density was set to $\rho_s = 10^6$.

field would tend to zero at the origin but the calculated field tends to some larger value instead.

2.5.5 Solutions around Legendre polynomial shapes

As another comparison to work in the literature, I attempted to reproduce the results from Ref. [95]. This paper attempted to use a Picard nonlinear solving method with the FEM to solve the chameleon field around irregularly shaped sources. In this sense, SELCIE can be viewed as a continuation of this work. Ref. [95] aimed to investigate what shapes would optimise experimental searches for the chameleon field by maximising the resulting fifth force. Specifically, the shapes tested were constructed using Legendre functions, $P_i(\cos\theta)$, as a basis such that shapes are defined

$$R(\cos\theta) = \sum_{i=0}^{3} a_i P_i(\cos\theta), \tag{2.38}$$

where a_i are the coefficients of the shape. The shapes were placed in a vacuum chamber of radius 15 cm and wall thickness of 3 cms. The fifth force was measured for a distance of 5 mms from the surface of the source.

The wall and source density were both set to 1 g/cm^3 while the vacuum density was 10^{-17} g/cm^3. The remaining parameters used were: $n = 1$, $M = M_{\rm pl}/\beta = 10^{18}$ GeV and $\Lambda = 10^{-12}$ GeV. Using SELCIE I reconstructed this setup for each Legendre polynomial shape tested in Ref. [95]. The densities were rescaled by the vacuum value stated above and the length scale L was set to the chamber radius. The value of α was calculated using equation (2.2) to be $\alpha = 6.1158 \times 10^{18}$. Our results are presented alongside the original results from Ref. [95] in Table 2.1.

From this table we see that our results are in disagreement with the previous results. In fact, both the individual values and the increase in the fifth force from the spherical case (bottom row) disagree. However, due to the extensive testing I have performed on SELCIE, I am confident in its results and believe there is an error in the calculation of the results reported in Ref. [95]. The new results for these shapes, found with SELCIE, could be interpreted as implying that optimising the shape may not yield as large an increase to the fifth force as previously suggested in Ref. [95]. However, since I am not confident in the previous results, I also have no reason to believe that the Legendre coefficients listed are the optimum values. It is still possible that for some choice of coefficients there is a significant increase to the fifth force compared to the spherical case.

2.6 Discussion

In this chapter I have introduced SELCIE as a tool to help study the chameleon field. Currently SELCIE solves the static chameleon equation of motion in the form of equation (2.1). Using SELCIE the chameleon field equation can be solved for highly non-symmetric systems constructed by

a_0	a_1	a_2	a_3	$\left.\frac{\delta g}{g}\right\|_P [10^{-11}]$	$\left.\frac{\delta g}{g}\right\|_S [10^{-11}]$
0.82	0.02	0.85	3.94	4.82	2.25
0.97	0.59	0.03	3.99	4.68	2.24
1.34	0.18	0.41	2.89	4.52	2.26
1.47	0.19	0.27	2.63	4.47	2.29
2.00	0.00	0.00	0.00	1.73	2.24

Table 2.1: Table of fifth forces measured from Ref. [95] (labelled as P) compared to results produced from SELCIE (labelled as S). In both cases the recorded acceleration experienced by a test particle, δg, is stated relative to the gravitational acceleration on the surface of the Earth ($g = 9.81$ ms^{-2}). The a_i values correspond to the Legendre coefficients used to define the shapes in [95].

the user. This can therefore be used to find solutions for systems which lack an analytic solution and to optimise existing experiments used to detect the chameleon field.

I have demonstrated the reliability of SELCIE to reproduce approximate analytic results from the literature for a variety of sources and density profiles; however, its functionality is much broader than this. For example, density distributions from N-body simulations or galaxy halo profiles can be easily inputted into SELCIE to find the corresponding chameleon profile and fifth force, enabling precision tests of the chameleon model on cosmological scales.

In Ref. [2], SELCIE has already been used to test the viability of detecting a chameleon signal through observations of galaxy cluster halos. In the following chapter I will use SELCIE with a genetic algorithm to find experimental configurations which optimise the possibility of detecting a chameleon fifth force. This optimisation algorithm could be used, for example, to extend the reach of current and future experiments that search for chameleon fifth forces with atom interferometry [26, 27, 28, 29, 96], ultra-cold neutrons [36, 38, 39, 97, 98, 99], torsion balances [20, 71, 100], Casimir experiments [23, 101, 102, 103, 104] or opto-mechanical sensors [105, 106, 107, 108].

I intend to continue to develop and extend SELCIE in the future to generalise the methodology to work with alternative forms of the chameleon model and other screened scalar fields such as the symmetron. I also plan to extend the code to allow the density profile and the field to evolve in time. Throughout the literature the chameleon field is assumed static,[3] and so it would be of interest to study what effects a dynamic system has on the field. This could lead to strengthening constraints by re-evaluating known systems (e.g. Earth-Moon system) or by developing new experiments that utilise dynamical systems.

---

[3] Notable exceptions include Refs. [109, 110, 111, 112, 113, 114].

Chapter 3

Using Machine Learning to Optimise Chameleon Fifth Force Experiments

The nonlinearity of the chameleon's equations of motion makes calculating analytic solutions very difficult. Examples do exist in the literature, as discussed in section 1.6.2, but these are only for highly symmetrical source shapes and often involve approximations that limit the solution to specific regions of parameter space. Constraints from experiments and observations will either come from one of these analytic approximations or from numerically solving the equations of motion for the system being studied.

The question may then arise: is the experimental system optimal for detecting chameleons? Comparing the solutions in section 1.6.2 it is clear that the resulting field profiles will differ even for sources with equal density and size[1]. We therefore see clearly that the chameleon violates the WEP, since

---

[1] The cylinder would, due to the assumed symmetry, be infinite in length and mass. Therefore, when comparing the sources I am considering a cylinder with equal radial size to the spherical source. When comparing the spherical and ellipsoidal sources I do

its fifth force has a dependence on the shape of the source mass. This means that in an experiment measuring fifth forces, choosing to use a spherical source over a cylinder will improve the experimental sensitivity. Since a dependence on the source shape exists for the chameleon [69, 95, 115, 116], there must exist a shape that maximises the force when taking all other parameters to be fixed. Using such an optimised source shape in current and near future experiments would yield improvements to experimental sensitivity and thereby strengthen the resulting model constraints. The aim of this work is to demonstrate a method by which this optimised source shape can be found. The exact shape will depend on what observable is being optimised and so will depend on the specific experiment.

In this chapter I will determine the rotationally symmetric shape which maximises the force at a single point a fixed distance from the source, inside a spherical vacuum chamber. I employ several parameterisations to mathematically describe the source shapes. This reduces the problem to finding the set of parameters that maximise the fifth force, although the dimension of this parameter space will inevitably be large if we wish it to encompass complex shapes. Using the SELCIE software package, discussed in chapter 2, meshes were generated of the source shape inside a spherical vacuum chamber, with an additional surface for measurements at a fixed distance from the source.[2] SELCIE was also used to numerically solve for the chameleon field profile of the system and solve for the field gradient magnitude which is proportional to the force. I then iterate over the mesh vertices along the 'measuring surface' and output the maximum value of the field gradient magnitude. The goal then is to find the set of parameters defining the source shape that maximise the field gradient

---

so assuming equal mass.

[2] For a review of the challenges in numerically simulating screened theories in laboratory and astrophysical environments see Ref. [117], and for a related finite element code that can simulate the behavior of the chameleon in satellite experiments see Ref. [118].

magnitude outputted by this algorithm. To achieve this optimisation I used the DEAP software package (`https://github.com/deap/deap.git`) to automate the design and running of a ‘genetic algorithm’ (GA) [119]. These GAs are a class of machine learning algorithms that use concepts of Darwinian evolution to improve a population of solutions so that it converges to an extremum in the solution space [120, 121]. They also do not require the problem being optimised to have an analytic form, and are efficient even for problems with a large solution space dimension.

I will begin this chapter by reviewing the large α approximation in section 3.1. The details of the GA will be explained in section 3.2. In section 3.3 I will define the shape parameterisations used and show the results of my investigation using the GA when the measuring distance from the source and chameleon potential are fixed. Sections 3.4 and 3.5 will then explore the effects of changing the measuring distance and potential, respectively. I will then end this chapter with section 3.6, where I will discuss the findings obtained by combining the GA with SELCIE.

3.1 Using Large α Approximation

In section 2.5.1, I showed that in the regime where $\alpha \gg (n+1)$ the chameleon field inside a vacuum chamber is well approximated by equation (2.29), where $\hat{\varphi}$ is related to $\hat{\phi}$ by equation (2.28). The significance of this result is that by solving for $|\hat{\nabla}\hat{\phi}|$ for one value of α, we can then determine the fifth force strength for all values where $\alpha \gg (n+1)$, by applying an overall rescaling to the solution. This statement remains true while the dense regions of the system are much more dense than the vacuum, because the value of φ inside the dense regions will differ for different values of α, but for sufficiently large density the differences become negligible as $\varphi \approx 0$. Therefore, assuming the above conditions to be satisfied I can express equation (2.6) as

$$\frac{|\vec{F}_{\hat{\varphi}}|}{|\vec{F}_{\rm g}|} = \frac{\beta\Lambda}{M_{\rm pl}L|\vec{a}_{\rm g}|}\left(nL^2\Lambda^2\right)^{\frac{1}{n+2}}|\hat{\nabla}\hat{\varphi}|, \tag{3.1}$$

where $|\hat{\nabla}\hat{\varphi}|$ (which in the rest of this work will be referred to as the force) depends on n and the profile of $\hat{\rho}$ but not on Λ, β or L. This equation is also entirely independent of both the source and vacuum density values, so long as there exists a sufficiently large hierarchy between them. We also see from this equation the importance of the domain size on the measured fifth force. Since β and Λ are constants, and $\hat{\varphi}$ is independent of L (as long as $\alpha \gg (n+1)$), the total dependence of the domain size, L, on the above expression is $L^{-n/(n+2)}$. This means smaller systems will yield higher sensitivity to fifth forces. For the case where $n = 1$ equation (3.1) can be used to express the acceleration acting on the test mass due to the scalar field in physical units as

$$\left(\frac{|\vec{a}_{\hat{\varphi}}|}{\rm nm/s^2}\right) = 0.373\beta\left(\frac{\Lambda}{\rm meV}\right)^{\frac{5}{3}}\left(\frac{L}{\rm cm}\right)^{-\frac{1}{3}}|\hat{\nabla}\hat{\varphi}|. \tag{3.2}$$

3.2 Genetic Algorithm

In this chapter I use the genetic algorithm (GA) software DEAP [119] to optimise the shape of a source mass such that the fifth force it gives rise to at a fixed distance is maximised. GAs are designed to take an initially random population of solutions to a problem and evolve them in order to find the optimum solution [120, 122]. This is done in three stages; selection, crossover, and mutation. In the first stage, selection, it is determined which individuals will survive to parent the next generation. To make this determination each solution in the population is evaluated using the function we wish to maximise (or minimise), which I will refer to as the fitness function. The fitness of an individual in our population is then the corresponding output of this fitness function, and will determine the likelihood of an individual surviving. As is the case with the later stages (crossover and mutation) there are many methods to determine survivors in our population. For a comparison of the different possible configurations of the GA see Appendix A. The method I ultimately chose was a tournament method, where I randomly select $N_{\text{tournsize}}$ individuals and return the one with the best fitness (largest value if searching for maximum and smallest value for minimum) [123]. This process is repeated N times, where N is the size of our original population. Note that it is possible for individuals to be selected multiple times. This process imitates natural selection and results in a new population with an increased average fitness. It is these survivors that will be the parents of the next generation. The fact that an individual can be selected multiple times is analogous to members of a species that have more offspring, thereby making its characteristics more abundant in the next generation.

Reproduction is replicated in the crossover stage, whereby individuals in the population are paired and each pair has some probability, P_x, of reproducing. If this occurs then each attribute of the solution pair (e.g. their coefficients) have a p_x chance of being swapped. The pair has now become a pair of children that replace the parents in the population. This process combined with the selection process allows individuals with better fitness values to share features with a larger number of other individuals at a faster rate than those with worse fitness. Overall, this will lead the population as a whole to flow towards optimum fitness.

A general problem with optimisation algorithms is that of local maxima. If an individual finds such a solution, it can lead the rest of the population to it without finding the global maximum (e.g., see Ref. [124]). The strategy used by a GA to address this is contained in the mutation stage. This stage is inspired by the mutations in natural organisms required for evolution, and modifies the information present in the current population. In this stage, each individual in the population has some probability, P_m, of receiving a mutation. This involves changing some of the attributes of the individual through some process involving randomness. In this chapter, since our parameters are continuous, each coefficient of the mutated individual has probability p_m of receiving a Gaussian perturbation with standard deviation σ. This allows individuals to escape from local maxima while introducing more variation into the population, allowing more of the parameter domain to be explored.

In total, this algorithm has 7 parameters that must be set by the user, $\{N, N_{\text{tournsize}}, P_x, P_m, p_x, p_m, \sigma\}$. In this chapter $\{N, N_{\text{tournsize}}, P_x, P_m, p_x\} = \{105, 5, 0.7, 0.1, 0.5\}$. The values of $\{p_m, \sigma\}$ will depend on the number and domain of the coefficients. The process by which I decided on the methods described above, and the values of the parameters, is discussed in Appendix A.

3.3 Shape optimisation

To begin finding the shape which optimises the chameleon force, I will need to first define a space of shapes through some parameterisation. I note that any parameterisation of shapes, for reasons of practicality, must be described by a finite number of coefficients. However, in a complete basis an infinite number of coefficients is required to reproduce all possible shapes. Therefore, any optimisation performed using a particular parameterisation will at best find the global maximum of a finite sub-space of shapes, and not of the infinite space of shapes. I therefore investigated multiple shape parameterisations to probe different regions of the shape space in the hope of discovering consistent solutions, or even shared features that point to a more globally optimum solution. For each of these parameterisations I will require a function that maps the parameters to the measurable of interest. I shall henceforth refer to this function as the fitness function, given I intend to maximise it using the GA discussed in section 3.2. In this chapter, the measurable outputted by this fitness function is the force at a single point that lies somewhere on a measuring surface a distance d from the source, which lies inside of a spherical vacuum chamber (For details see Appendix B). I restricted our search to rotationally symmetric sources as it allowed us to represent the systems using 2D meshes by imposing the symmetry on the field solutions. The reason for this was to reduce the runtime and memory requirements, although in principle our approach can be extended to more arbitrary systems by using 3D meshes instead.

The fitness function starts by taking the shape parameters and from them derives a list where each element contains the coordinates of a point. These points connected in sequence by straight lines define the boundary of the source. The python package SELCIE is then used to construct a mesh representing the system. This includes the source, a measuring surface a distance d from the source[3], the vacuum, and the chamber wall. The mesh settings used were such that the cell size was a minimum at the boundary of two regions, with a size of CellSizeMin $= 10^{-4}$, grew linearly for a distance

---

[3] In Ref. [95], the chamber radius was 15 cm and the force was measured a distance 0.5 cm from the source, giving a ratio of ~ 0.03. Therefore in the following sections the default distance from the source where the force is measured, in rescaled units, is $d = 0.05$.

DistMax = 0.1, beyond which the cell size was CellSizeMax = 0.01 (see Appendix C for a discussion on the tests performed to calibrate the mesh settings). The exception to this was the boundary between the vacuum and the chamber wall which had CellSizeMin = 5×10^{-4} and DistMax = 0.5 instead, since this improved the runtime while contributing negligibly to the solutions' accuracy. The thickness of the chamber wall was set to 0.05, as this is a small value, therefore the mesh is smaller, but still large enough so that the field reaches its minimum inside the wall (even for the case of an empty vacuum chamber which is the scenario with the largest field values). Using this mesh, SELCIE is then used to calculate the scalar field profile and the force induced by the field. Finally, the magnitude of the force is evaluated at the mesh vertices that form the measuring surface. The largest of these values is then the output of the fitness function. The optimal shape will correspond to the global maximum of this function on the shape parameter space. For shape spaces with a dimensionality of one or two, it is reasonable to perform an iterative search of the parameters. However, as the dimension of our parameterised shape space increases this method becomes impractical. I will therefore use the GA, as described in section 3.2, to find the shape parameters that maximise the outputted force value.

In the following sections I will define our shape parameterisations and will probe the corresponding space of shapes to find the shapes that maximise the chameleon force. I will then compare these optimal shapes to determine if there are any consistent features among them and whether these are indicative of a superior class of shapes.

3.3.1 Ellipsoids

I will begin our investigation with ellipsoidal shapes (for earlier work see Ref. [69]). Being the simplest deviation from spherically symmetric sources, these shapes are parameterised by the horizontal and vertical axis radii, r_x and r_y respectively. Since the shape space is only 2-dimensional, it can be thoroughly investigated without the need of the GA. The boundary of the ellipse in the (x, y) plane is $(x, y) = (r_x \sin(\theta), r_y \cos(\theta))$, for $\theta = [0, 2\pi)$. For our purposes, however, it will be more useful to parameterise the ellipsoids by their axis-ratio, $\epsilon = r_y/r_x$, and the volume of the ellipsoid

$$V = \frac{4\pi}{3} r_x^2 r_y, \tag{3.3}$$

where I have used the fact that our source has rotational symmetry around the y-axis. For such ellipsoids with a volume V and axis ratio ϵ, their axis radii can be expressed as $(r_x, r_y) = (\zeta, \zeta\epsilon)$, where the scale factor ζ is

$$\zeta = \left(\frac{3V}{4\pi\epsilon}\right)^{1/3}. \tag{3.4}$$

Some examples of ellipsoids parameterised by (V, ϵ) are shown in Figure 3.1.

Figure 3.2 shows the magnitude of the resulting force, at a distance $d = 0.05$ (in units of vacuum chamber radii) from the source, for the values $\epsilon = [0.01, 2.0]$ and $V = [10^{-5}, 0.1]$. A note-worthy feature of this plot is that slight deviations from spherical sources appear to always result in an increase in the measured force, the location of which is around the pointed region of the ellipsoid as predicted in Ref. [115]. I also note that Figures 3.2a and 3.2b show that for fixed ϵ as V decreases the force increases. The intuition behind this is that as the source decreases in size, and the vacuum

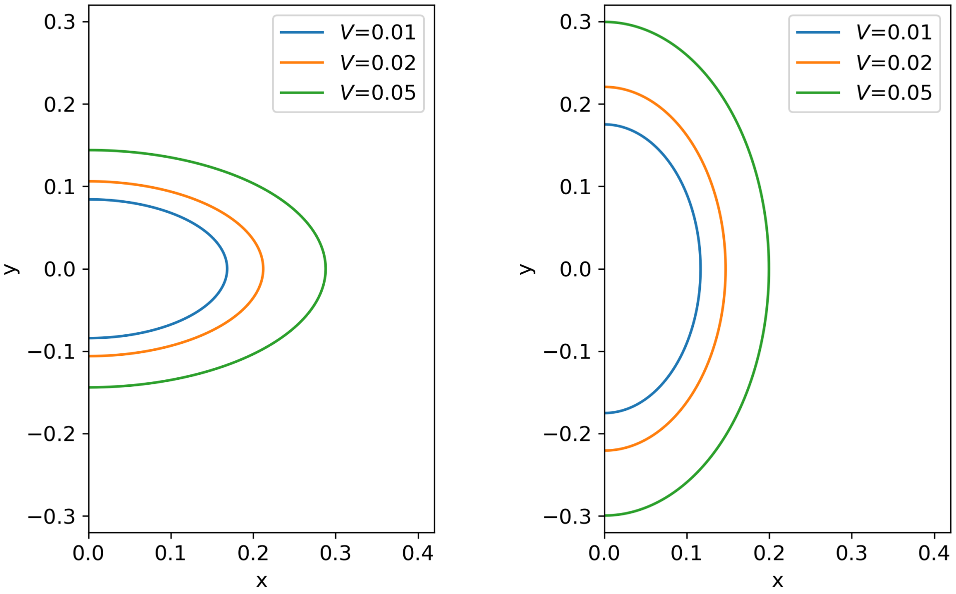

Figure 3.1: Boundary curves of elliptical shapes of varying volume and axis-ratio. The **left** plot contains ellipses with $\epsilon = 0.5$, while the **right** contains ellipses with $\epsilon = 1.5$.

increases in size, the field can reach a larger maximum value in the vacuum, and consequently the field gradients will be larger. However, Figures 3.2c and 3.2d show that this trend reverses after some critical volume, $V_c(\epsilon)$, due to the fact that there is less overall matter contributing to the force. The overall effect can be seen clearly in Figure 3.3 where I have plotted the force against volume for a range of ϵ-values.

Figure 3.4 shows this critical volume $V_c(\epsilon)$, at which the force is maximised, for a range of ϵ. In this plot I also show the maximal force obtained for the corresponding ellipsoids. We see that as the ellipsoids deform away from the spherical case, along either axis, the critical volume decreases and the corresponding force increases. This change is strongest with decreasing ϵ, which corresponds to disc like ellipsoids. I acknowledge that the plot of $V_c(\epsilon)$ is not entirely smooth. This is because when performing our simulations I use a mesh of finite precision, resulting in a small numerical uncertainty. Although the relative uncertainty on the force is of the

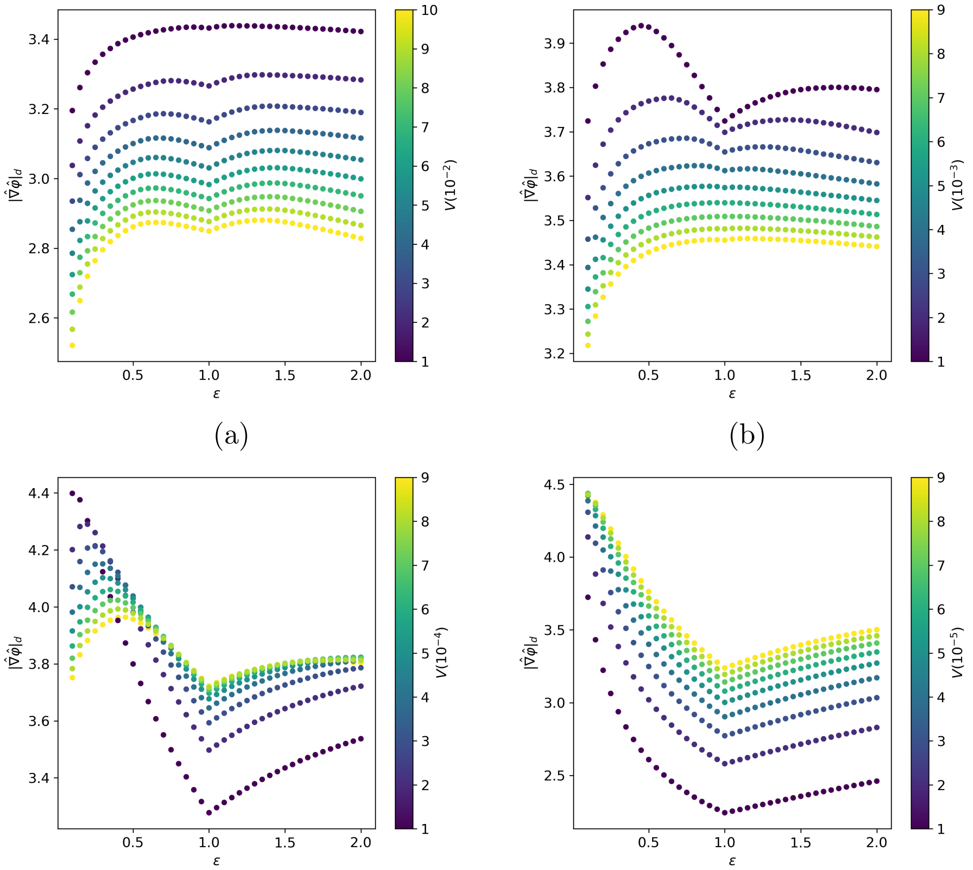

(a) (b)

(c) (d)

Figure 3.2: The measured maximum force (at distance 0.05 from the surface of an ellipsoid) against axis ratio $\epsilon = r_y/r_x$. The colour map represents the volume of the ellipsoid. Each subplot shows the results for a different order of magnitude in volume, with the largest volumes in the top left and the smallest in the bottom right.

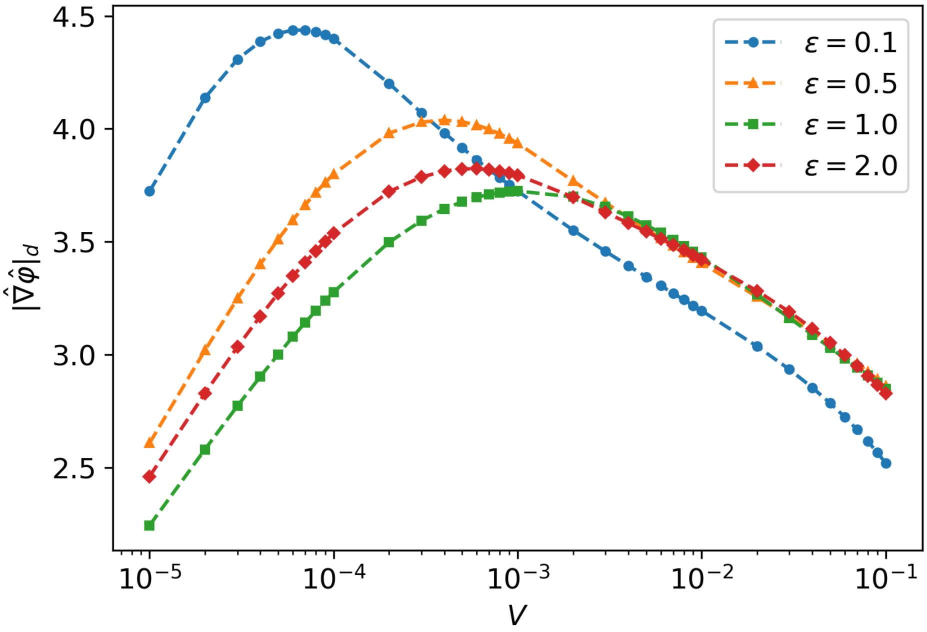

Figure 3.3: Measured maximum force (at distance 0.05 from the surface of the ellipsoid) against source volume, for a range of axis-ratio values.

order 10^{-4}, the finite mesh precision leads to a larger uncertainty on our measurement of V_c. Finally, I acknowledge that our plots would indicate that the ideal ellipsoid lies outside our parameter range. This is because of computational limitations of solving the field equation using meshes capable of resolving such small and elongated shapes. In practise, however, a very small ellipsoid will be impractical in realistic experiments.

3.3.2 Legendre Polynomial Shapes

As mentioned in section 1.6.2, Legendre polynomials, P_n, are a special set of polynomials that are solutions to equation (1.66). This set of functions has the property

$$\int_{-1}^{1} P_n(x)P_m(x)dx = \frac{\delta_{nm}}{2n+1}, \tag{3.5}$$

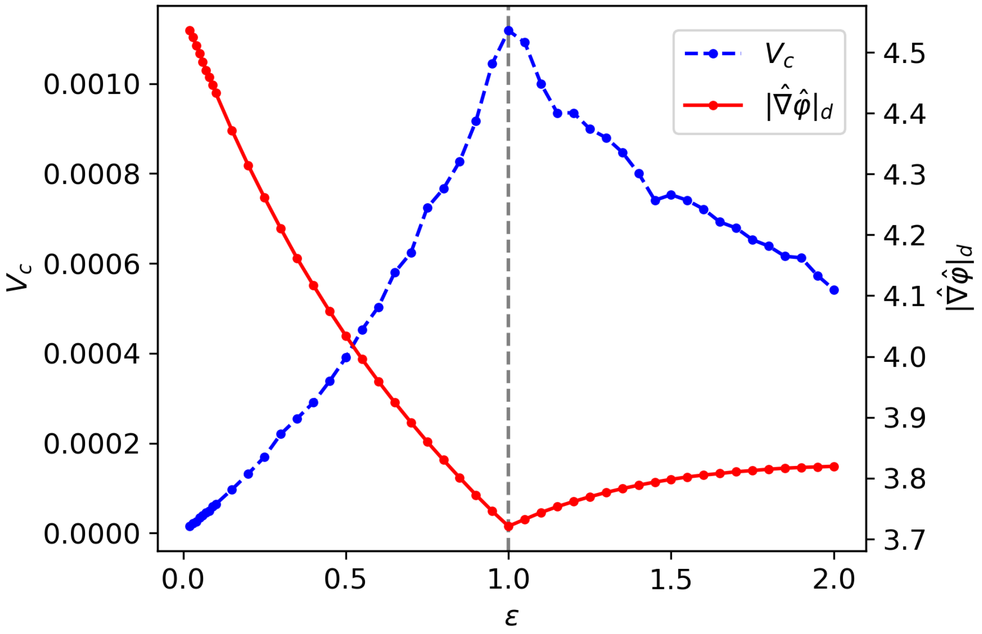

Figure 3.4: Critical volume (**blue**) and corresponding force measurement (**red**) against axis-ratio, ϵ. The vertical gray dashed line at $\epsilon = 1$ indicates the location of the spherical case.

showing that it forms a complete basis in the interval $[-1, 1]$. This means if I define a set of curves in polar coordinates $(R(\theta), \theta)$ where

$$R(\theta) = \sum_{n=0}^{N} a_n P_n(\cos\theta) \tag{3.6}$$

and a_n are the series coefficients, then in the limit $N \to \infty$ the set will grow to contain every closed curve that is also symmetric around the y-axis. However, I must still consider how I relate these curves to shapes. For example, for some sets of a_n, it is possible for $R(\theta)$ to take negative values, which can result in the curve intersecting itself. In this chapter I take positive $r < R(\theta)$ to be inside the shape, and to avoid complications will set $R(\theta) = R_{\text{min}}$ whenever the value of $R(\theta)$ given by equation (3.6) is less than R_{min}. To investigate the shape dependence of the force, I keep the volume of the source fixed. I therefore define a mapping (see Appendix

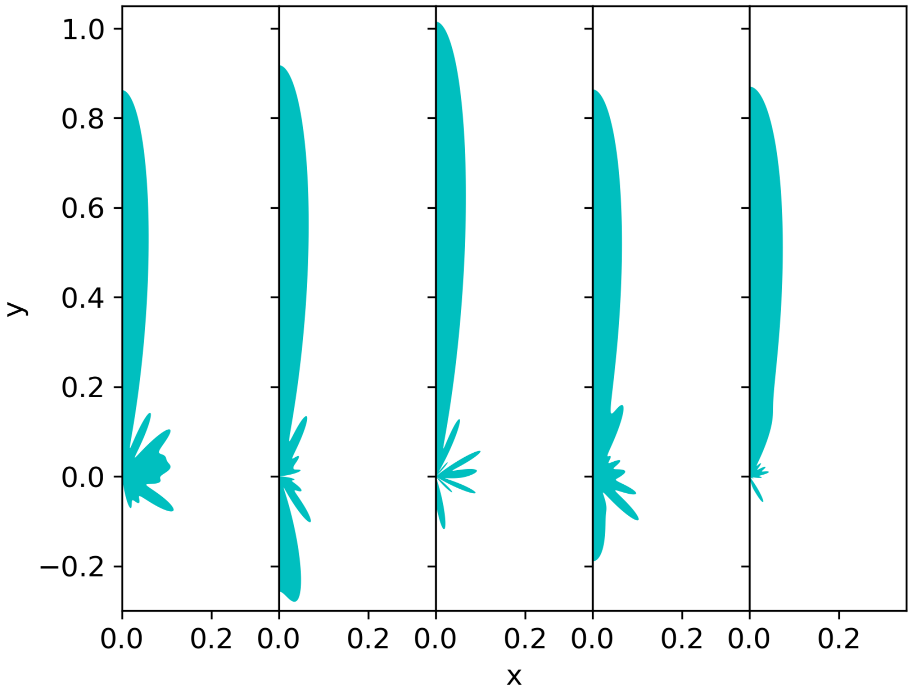

Figure 3.5: Examples of Legendre polynomial shapes defined using $N = 20$ coefficients and with a volume fixed to $V = 0.01$.

E)[4] from one set of coefficients, a_n, to a new set where the corresponding Legendre polynomial shape is similar to the original but with a volume V. Some examples of the kinds of shapes contained inside this class are shown in Figure 3.5.

It can be shown that the Legendre polynomials, in the domain $[-1, +1]$ have a maximum at $P(\theta = 0) = 1$. Constraining the coefficients a_n to be positive, this means the maximum value taken by equation (3.6) is

$$R_{max} = \sum_i a_i. \tag{3.7}$$

For practical reasons, I will only consider Legendre polynomial shapes that

---

[4] Initially I used the method in Appendix D. However, errors due to numerical precision compounded as N increased, rendering it unreliable when using $N = 20$ coefficients.

are contained entirely inside the vacuum chamber, e.g. $R_{max} < 1$ (after constraining the volume).

Using the method described in section 3.3 I can obtain a force value from the set of coefficients a_n that define a Legendre polynomial shape. The number of coefficients used was $N = 20$; however, after applying the volume constraint the number of dimensions of the shape parameter space is reduced to 19. Because of the large number of dimensions of the shape space I will use the GA discussed in section 3.2 to find the shape, parameterised by Legendre polynomials, that maximises the force at a distance $d = 0.05$ from the source evaluated at a single point. For a volume of $V = 0.01$ the shape outputted by the GA generated a force of $|\hat{\nabla}\hat{\varphi}|_d = 5.07$ (located along the y-axis), which is a 48% increase when compared to a spherical source of the same volume centred at the origin. The profile of the scalar force induced by the source is shown in Figure 3.6 along with the position where the force is maximised.

I repeated our GA simulation for a range of other volumes, and found that as the volume is decreased the force becomes larger, as was the case with the ellipsoids. I also observed that the 'umbrella'-like[5] feature near $\theta = 3\pi/4$ in Figure 3.6 appears to be a common feature in each case, with the extra volume being diverted to the upper region, as seen in Figure 3.7. Since our populations have independently evolved this feature, it suggests this may be the most important feature of the final shape and that it is independent of the total volume. This aspect will be further investigated in section 3.3.4.

---

[5] Since I have imposed that the system has rotational symmetry around the y-axis, the shapes will be 'umbrella'-like when viewed in 3-dimensions.

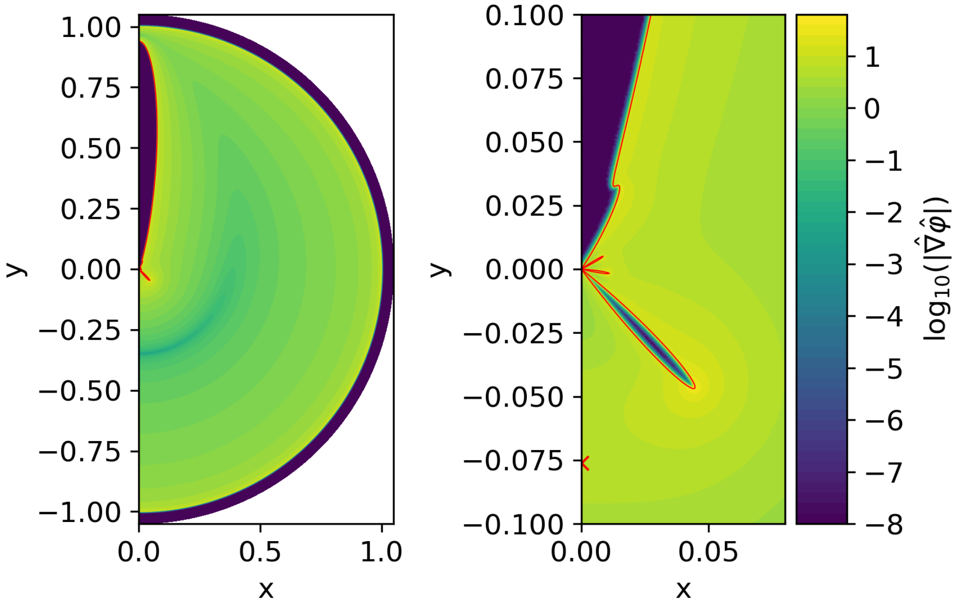

Figure 3.6: The chameleon force profile of an $N = 20$ Legendre polynomial source (boundary of which is indicated by the red line) inside a spherical vacuum chamber. The **left** plot contains the full solution while the **right** is zoomed in on the central region. In the **right** plot the red cross on the y-axis below the source, at around $y = -0.075$, indicates the position where the force (at a distance from the source of $d = 0.05$) is maximised. The value of this maximal force is $|\hat{\nabla}\hat{\varphi}|_d = 5.07$.

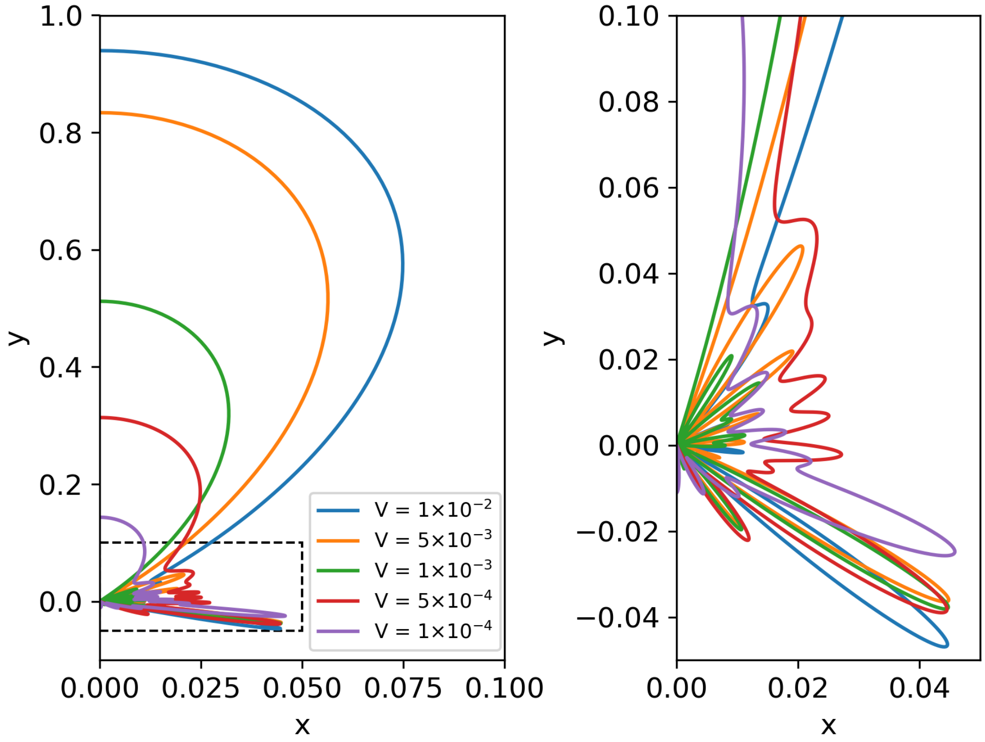

Figure 3.7: Shapes outputted by the GA when finding the optimal Legendre polynomial shape with $N = 20$ coefficients. Each line indicates a shape with a different volume, as shown in the legend, from $V = 10^{-4}$ to $V = 10^{-2}$. The **left** plot shows the full shapes, while the **right** is a zoomed in image of the area inside the dashed line.

3.3.3 Radially-Parameterised Shapes

In this class the N points defining the source boundary are given in polar coordinates as (R_n, θ_n), where $\theta_n = \pi n/N$ and R_n is a product of the coefficients b_k such that

$$R_n = \Pi_{k=0}^{n} b_k. \tag{3.8}$$

For the case $b_k = 1$ for all k-values, the shape will approximately be a sphere (once the rotational symmetry is taken into account). To ensure the class contains well-behaved shapes I enforce that $b_k > 0$, so radial values are always positive. Also, since each radial value can be seen as the previous value multiplied by a factor b_k, by changing the range of values b_k can take, I can control the smoothness of the shapes. This second point is important since I am refining the boundary of the shape, and so a large perimeter will require more cells, increasing the overall simulation time and memory required. I again will constrain the volume of the shapes to be a predetermined value V, therefore reducing the dimension of the shape space to $N - 1$. This was done using the same method as the Legendre polynomial shapes, and is discussed in Appendix E. Some examples of shapes contained in this class are shown in Figure 3.8.

I used the GA to optimise the force, a distance $d = 0.05$ from the source, of a radially-parameterised shape defined by $N = 50$ coefficients ranging between 0.5 and 1.5, and with a target volume of $V = 0.01$. The shape outputted by the GA had a force of $|\hat{\nabla}\hat{\varphi}|_d = 5.16$ (which is slightly larger than the value obtained for the optimal Legendre polynomial shape), and was again located along the y-axis. The profile of the force generated by this optimised source shape is shown in Figure 3.9, along with the position of the recorded value. Comparing this shape to the optimal Legendre polynomial shape shown in Figure 3.6, we see that the GA has outputted a similar

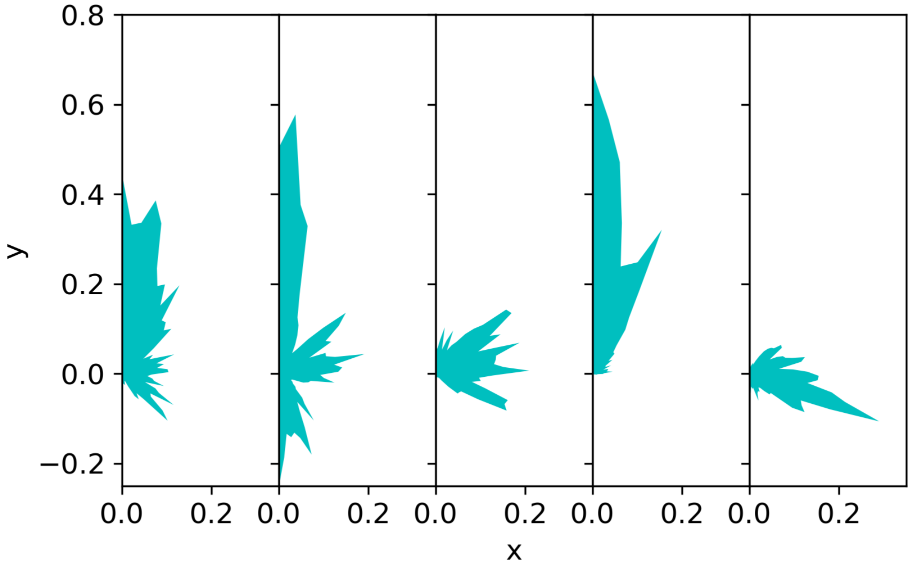

Figure 3.8: Examples of radially-parameterised shapes defined using $N = 50$ coefficients and with a volume fixed to $V = 0.01$.

shape, with a large lobe around $\theta = 0$ and a protruding spike (umbrella-like shape) in the lower region near $\theta = 3\pi/4$, despite being generated from two different shape parameterisations. This similarity is not only present for the $V = 0.01$ case. Comparing the GA results for radially-parameterised shapes of different volumes, I noticed similar shapes to those found when the GA was used with Legendre polynomial shapes for those same volumes, which can be seen by comparing Figures 3.7 and 3.10. In section 3.3.2 I hypothesised that the umbrella-like feature might be the most important to maximising the force, and that the rest of the shape is just there to satisfy the volume constraint. These new results support this hypothesis since we see the same feature independent of the volume and for $V = 10^{-4}$ we obtained only this feature without the upper lobe (note that it is not possible to obtain this shape with our Legendre polynomial parameterisation due to the property shown in equation (3.7)).

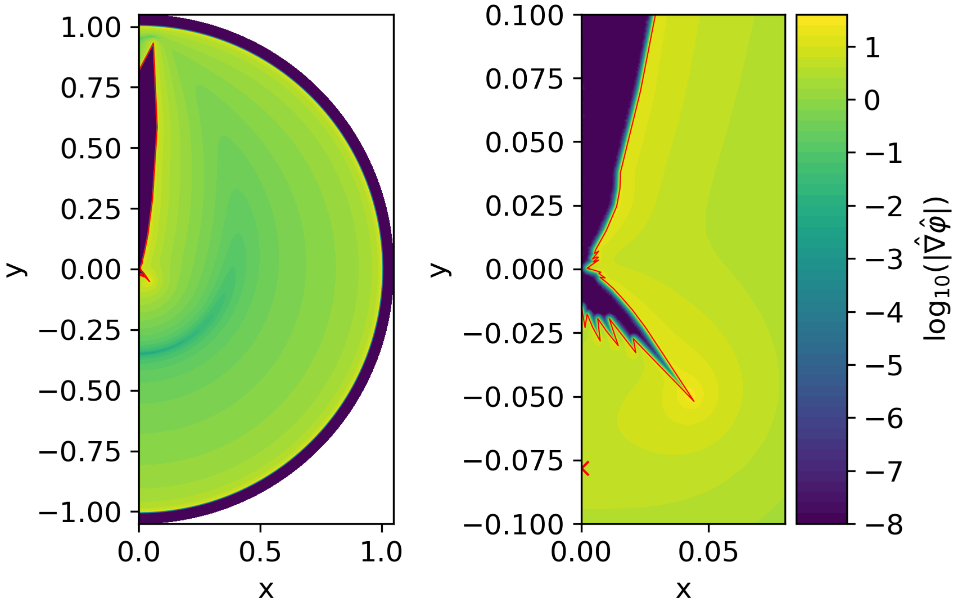

Figure 3.9: The chameleon force profile of a radially-parameterised source (boundary of which is indicated by the red line) inside a spherical vacuum chamber. The **left** plot contains the full solution while the **right** is zoomed in on the central region. The red cross on the y-axis below the source, at around y=-0.075, indicates the position where the force (at a distance from the source of $d = 0.05$) is maximised. The value of this maximal force is $|\hat{\nabla}\hat{\varphi}|_d = 5.16$.

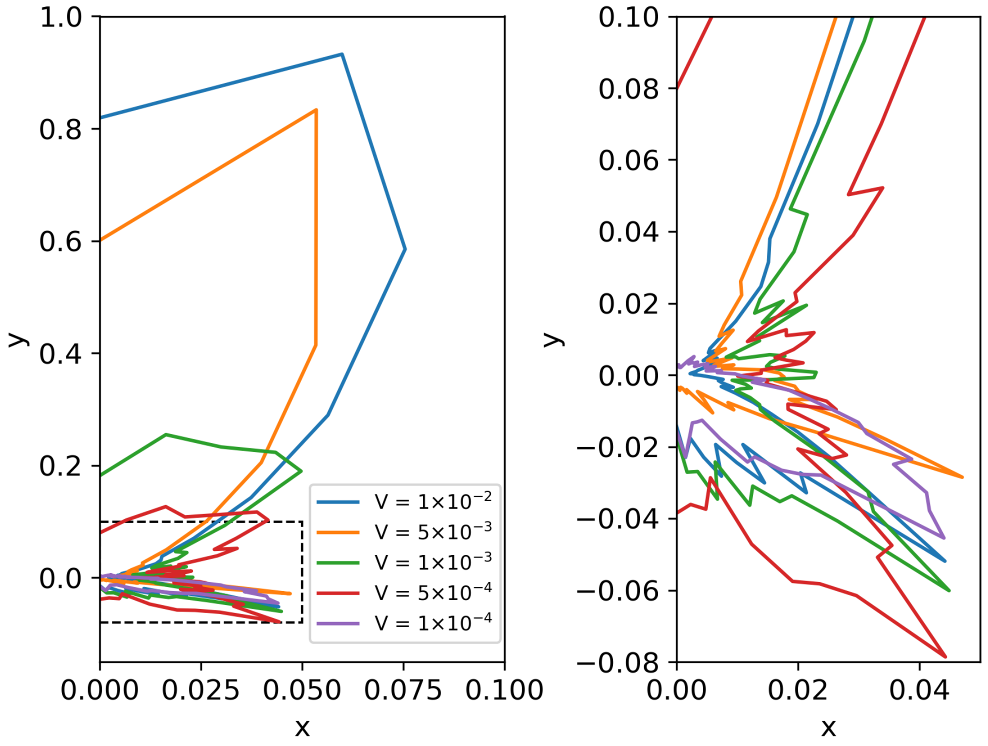

Figure 3.10: Shapes outputted by the GA when finding the optimal radially-parameterised shape with $N = 50$ coefficients that range between 0.5 and 1.5. Each line indicates a shape with a different volume, as shown in the legend, from $V = 10^{-4}$ to $V = 10^{-2}$. The **left** plot shows the full shapes, while the **right** is a zoomed in image of the area inside the dashed line.

3.3.4 Is the Umbrella the Most Impactful Feature?

In sections 3.3.2 and 3.3.3 I found that for both the Legendre polynomial and radially-parameterised shapes, the GA appeared to converge to similar shapes. Furthermore, shapes obtained from different volume constraints consistently produced a similar feature, as seen in Figures 3.7 and 3.10. As I impose rotational symmetry around the y-axis, the feature of interest is an umbrella shape. To test the importance of this umbrella feature I investigated how the measured force responds when other sections of the shapes, obtained in the previous two subsections, are removed. To do this I removed any part of the shape that lies above a cut-off height $y_c = \delta y_{\max}$, where $y_{\max}$ is the maximum y-value of the shape and $\delta \in [0, 1]$. The resulting forces for the Legendre polynomial and radially-parameterised shapes are plotted in Figures 3.11a and 3.11b respectively. In each case we see the position where the force is maximised is unchanged while its value increases as more of each shape is removed. This is in agreement with what was observed in section 3.3.1 (in Figure 3.3), in that above some critical volume the force increases with decreasing source volume. This further suggests that the umbrella shape, of this particular size, is the optimal shape we have been looking for. I will now test this hypothesis using a new shape class inspired by the umbrella shape in hopes to further improve our force.

This new class consists of three polynomials (one of order N and two of order $N + 1$) defined over the range $x \in [0, L_{\mathrm{u}}]$, where L_{u} is a parameter of the shape. The first polynomial (P_0) acts as the baseline of the shape and is defined to have N roots that are contained in the shape coefficients. The magnitudes of the second (P_+) and third (P_-) act as a displacement between P_0 and the boundary of the shape in the positive and negative y-

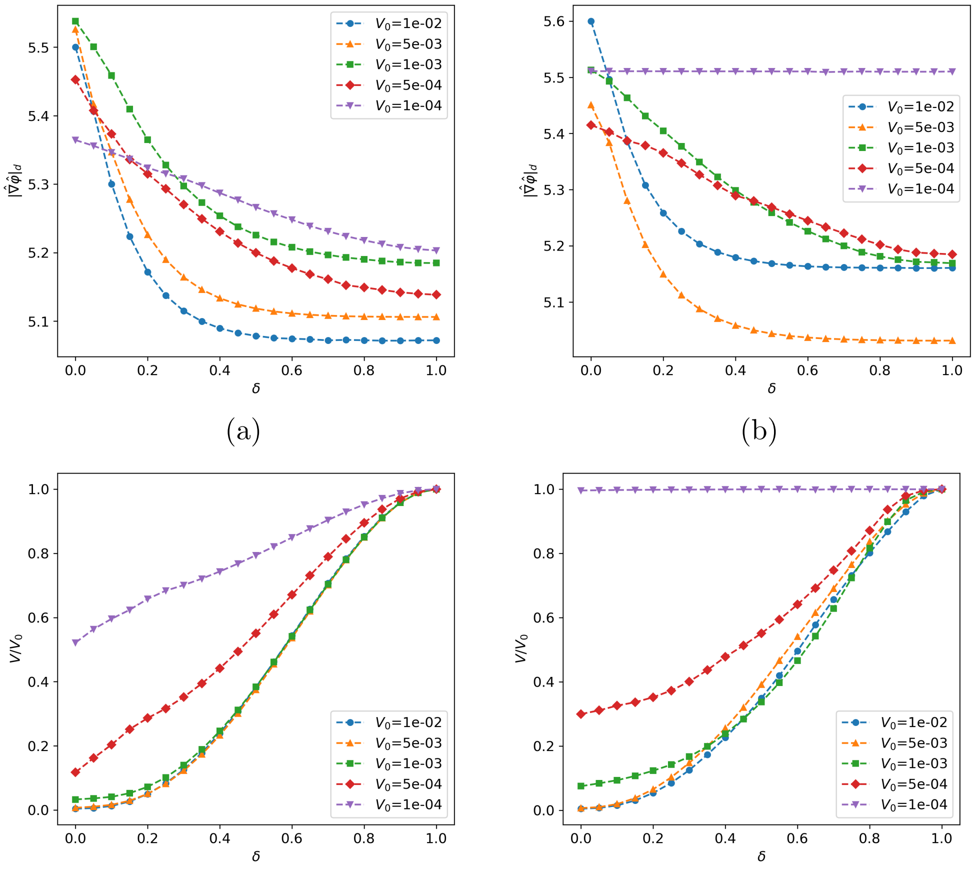

(a) (b)

(c) (d)

Figure 3.11: The force around Legendre polynomial (**a**) and radially-parameterised (**b**) shapes when parts of the upper lobe are removed. Each curve in plot (**a**) corresponds to one shape shown in Figure 3.7, while in plot (**b**) the curves correspond to the shapes in Figure 3.10. Plots (**c**) and (**d**) show the change in volume for the corresponding shapes shown in plots (**a**) and (**b**) respectively. The volumes of the unmodified shapes are shown in the legends.

directions respectively. These two polynomials are also defined by N roots contained in the shape coefficients but also have an additional root at $x = L_{\mathrm{u}}$ so that the combined curves form a closed loop. For simple polynomials with not too many curves this will lead to umbrella-like shapes. However, this class still has the possibility of producing much more complicated shapes. For further generality the shape is then rotated around the origin anti-clockwise in the $(x,\, y)$ plane by an angle θ, and then translated by the vector (x_0, y_0). Altogether, the number of parameters defining this class is $3N + 4$. In this and future sections I used polynomials of order 5 and 6, so the number of coefficients is 19, each ranging between 0 and 0.3. Unlike the previous shape classes, I place no constraints on the volume of the shape. I do, however, set a minimum positive value on the polynomials P_+ and P_-, to ensure that the curve does not intersect itself. A depiction of how shapes in this class are constructed, along with some examples, is shown in Figure 3.12. Among these examples one shows a case where the source has been separated into two disconnected pieces (shape filled in black). This occurred because to impose axis-symmetry I only consider parts of the shape for which $x > 0$, therefore a sufficiently curvy shape can become two disconnected sources.

Using the GA to find the shape in this class that optimises the force, I obtained the shape shown in Figure 3.13. We see the shape outputted by the GA is in agreement with our hypothesis that the umbrella was the optimal shape. Furthermore, thanks to the extra freedom provided by our parameterisation the outputted shape produces the best force value so far at $|\hat{\nabla}\hat{\varphi}|_d = 5.77$, and with a volume of $V = 1.26 \times 10^{-5}$. For scale this force is 2.45 times larger than that generated by a sphere, located at the origin, of equal volume and using the same measuring distance. Furthermore, since the volume (and by extension mass) of the source is so small, this will lead

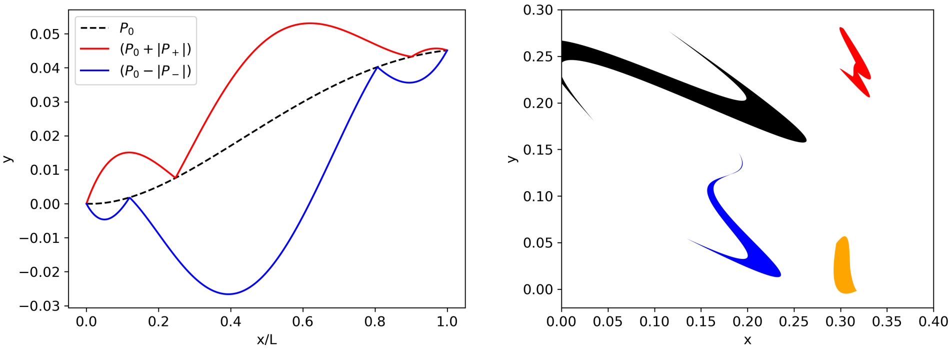

(a) (b)

Figure 3.12: Plot (**a**) illustrates the construction of the polynomial class of shapes where $N = 5$. The dashed line is the polynomial P_0, while the red and blue lines correspond to $(P_0 + |P_+|)$ and $(P_0 - |P_-|)$ respectively. The region enclosed defines the polynomial shape which is then translated and rotated according to the remaining shape coefficients. Plot (**b**) shows examples of shapes belonging to the polynomial class with coefficients bounded between 0 and 0.3.

to large ratios between the chameleon and gravitational forces.

3.4 Effects of varying measuring distance

In this chapter so far the distance between where I wish to measure, and therefore maximise, the force and the surface of the source has been fixed at $d = 0.05$. In this section I investigate how varying this distance, d, affects the optimal shape. I will use the polynomial shape class discussed in section 3.3.4 as it has provided the best results so far. The shapes shown in Figure 3.14a are the results of the GA using this class, for varying values of d. We see that the umbrella shape remains the optimal shape found in each case, with the point of greatest force (at our fixed distance) being on the y-axis. It can also be seen that the vertical position and length of the shape does depend on the measuring distance, with both increasing with d.

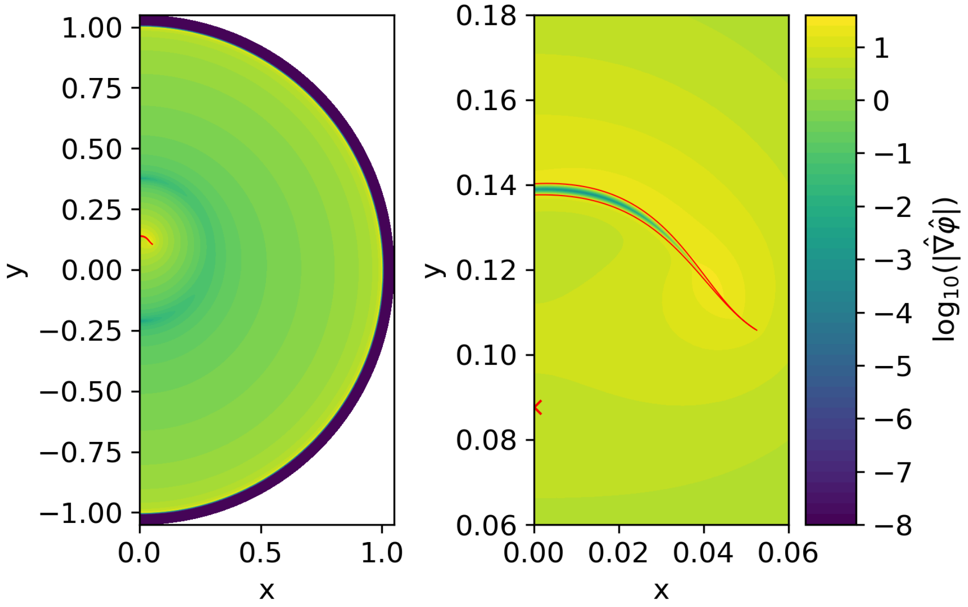

Figure 3.13: The chameleon force profile of a source whose shape belongs to the polynomial shape class where $N = 5$ (the boundary of the shape is indicated by the red line), inside a spherical vacuum chamber. The **left** plot contains the full solution while the **right** is a zoomed in version showing the region immediately around the shape. The red cross on the y-axis below the source, at around $y = 0.09$, indicates the position of where the force (at a distance from the source of $d = 0.05$) is maximised.

For each shape in Figure 3.14a I measured the maximum force at a range of distances, the results of which are shown in Figure 3.14b. In this plot I have also indicated where on each curve the value d is equal to the measuring distance the corresponding shape was optimised for, d_{opt}. As expected each shape has a force that monotonically increases with decreasing distance; however, for $d > d_{\text{opt}}$ the force decreases much faster than when $d < d_{\text{opt}}$. Focusing on the points where $d = d_{\text{opt}}$ we see that they approximately follow a $1/d$ relation, and the largest forces for any value of d are from the shapes optimised at that specific measuring distance. This provides further evidence that the optimal shape does depend on the measuring distance in the experiment. This then means that when designing an experiment the minimum measuring distance (due to the experiment's design or from physical effects such as Casimir or Van der Waals forces) must be established first before the optimal source shape can be determined.

3.5 Effects of Varying n

In the preceding sections I have explored the source shapes that could optimise the chameleon force measured in an experiment, for the potential shown in equation (1.44) with $n = 1$. However, this is not the only possible choice, and as more of the parameter space for $n = 1$ is excluded, interest will increase in the $n > 1$ chameleon models. To investigate how changing the value of n would affect the optimal source shape, I used the GA to find the shape in the polynomial class (see section 3.3.4) that optimises the force at a separation distance $d = 0.05$ for $n = 2$ and $n = 3$. I note that n can take some negative values that were not investigated in this work, but I expect the findings of this section to hold for these cases as well. The shapes outputted by the GA, and corresponding force profiles, are plotted

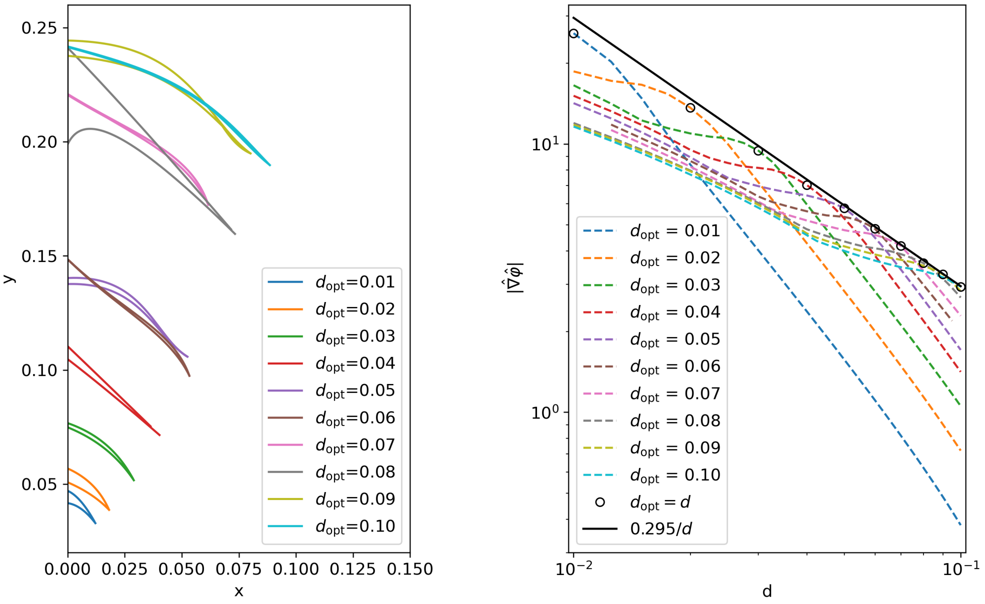

(a) (b)

Figure 3.14: Each line in plot (a) depicts the outline of a cross section of a polynomial shape (as described in section 3.3.4) outputted by the GA when optimising the force at different measuring distances, d_{opt}. For each of these shapes I then measured the maximum force at a range of distances, d, from the surface of the shape and plotted the resulting curves in plot (b). The black circles indicate when $d = d_{\text{opt}}$, and the black line shows the curve $|\hat{\nabla}\hat{\varphi}| = 0.295/d$.

in Figure 3.15a along with the $n = 1$ result discussed in section 3.3.4, for comparison. We see that the umbrella again appears as the optimal shape in each case, but with an increasing thickness and vertical displacement with increasing n.

We see that the $n = 2$ shape has a hole in it, and that the $n = 3$ shape appears to be an umbrella with a 'spike'. Looking at other shapes in the GA population for the $n = 2$ simulations I find almost identical shapes that generate very similar forces as the optimal but with no hole. I therefore conclude that the existence of the hole contributes negligibly to the force. This is because the size of the hole is smaller than the field's Compton wavelength. Since the Compton wavelength is the inverse of the field's mass, as expressed in equation (1.48), as n increases so will the Compton wavelength and consequently smaller features will not affect the chameleon field profile and not contribute as significantly to the force. We also see this in the $n = 3$ case where the shape outputted is consistent with the umbrella-like shape but with a spike. Looking at the force magnitude plotted in Figure 3.15d we see the spike contributes little to the force. The reason the GA outputted this shape can then be considered a consequence of an increasing Compton wavelength leading to a larger degeneracy in the shape to force mapping.

Now that I have determined that both the Compton wavelength and thickness of the shapes are increasing with n, I should determine whether the two effects are related by checking how much screening is occurring in each case. In this chapter I consider the interior of the source to be screened if the field has reached the value that minimises its effective potential in the source, $\hat{\phi}_{\mathrm{c}}$ (see equation (1.47)), and the field gradient has a small magnitude, $|\hat{\nabla}\hat{\phi}| < 10^{-10}$. Under this definition I find that each shape shown in Figure 3.15 is unscreened. However, measuring the field inside the sources, I found that the minimum field value was of the same order of magnitude as $\hat{\phi}_c$. This combination of properties make intuitive sense as an unscreened source has all of its mass contributing to the field, and minimising the field's value inside the source allows for larger gradients around it. The reason then for the thickness of the shapes in Figure 3.15 to increase with n is because as the field's Compton wavelength increases, so does the thickness needed for the field to reach $\hat{\phi}_c$. This also helps to explain why the umbrella shape appears to be the optimal shape, since it maximises the amount of unscreened matter around the measuring position while also maintaining the optimal thickness.

3.6 Discussion

In this chapter I aimed to show that by exploiting the shape dependence of the chameleon field, experimental sensitivity could be improved through the use of an optimised source shape. I also aimed to determine what characteristics were necessary for such a shape. To accomplish this I used the software package SELCIE, discussed in chapter 2, to numerically solve for the chameleon field profile of an axis-symmetric source mass inside a spherical vacuum chamber, and to measure the resulting force at a fixed distance from the source. The first class of shapes I investigated using this method were ellipsoids centred at the origin. I found that, for all volumes tested, as the ellipsoids deviate from the spherical limit the scalar force increases, with the largest forces being generated by disc-like ellipsoids. Additionally, I found that if the axis-ratio is fixed, then there is a critical volume which maximises the force, resulting in a preference for very small sources.

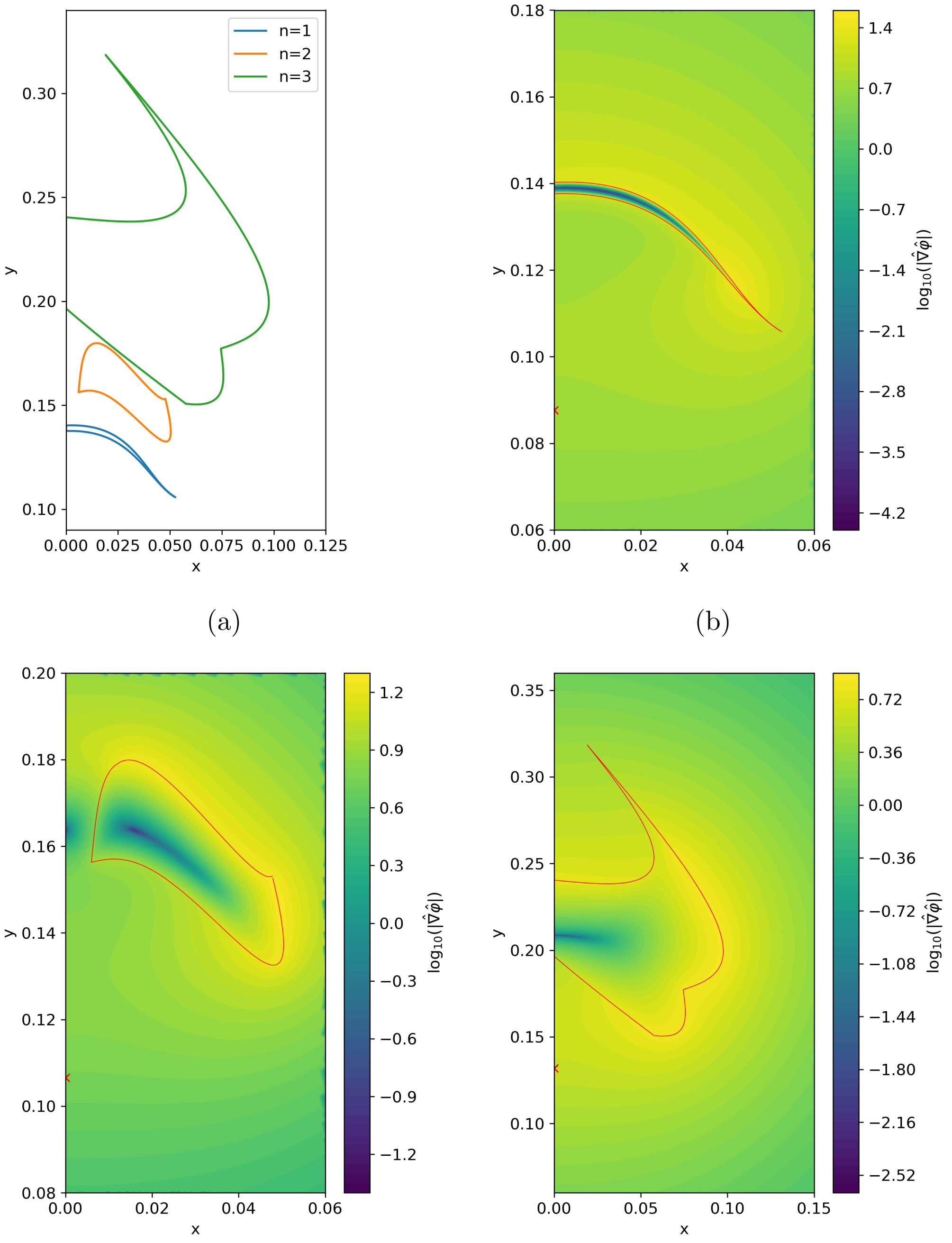

(a) (b)

(c) (d)

Figure 3.15: Polynomial shapes outputted by the GA for fixed measuring distance $d = 0.05$, but for varying n. Figure (a) shows the shapes compared to one another. Figures (b), (c), and (d) each show the chameleon force profiles sourced by the shapes in (a), for $n = 1$, $n = 2$, and $n = 3$ respectively. The red lines indicate the boundary of the shape.

I investigated more complex shapes, with fixed volumes, using multiple shape parameterisations combined with a GA, using the software package DEAP. I found that for each parameterisation used, the GA would converge to shapes with a common feature, even when the volume of the shapes was varied, indicating a solution that is independent of the choice of parameterisation. After further investigation using a new shape parameterisation that did not constrain the volume of the source, I confirmed that the shapes that generate the largest force values are 'umbrella'-like shapes, with the point where the force is maximised being located on the axis of rotation. The force generated by the optimum shape found (for $n = 1$) was 2.45 times larger than that of a sphere of equal volume located at the origin when the force is measured at the same distance to the source.

I also found that the thickness of the umbrella is tuned so that it was both unscreened and had the field reach the value that minimises its effective potential inside the source. This means all the matter sources the field profile whilst also having as large a total field variation as possible, leading to high field gradients. I found that when changing the form of the field's potential, the thickness of the umbrella changed with the field's Compton wavelength, in such a way that this feature was present in each case tested. This characteristic is consistent with the critical volumes found for ellipsoids. When varying the measuring distance d, I found that the umbrella shape remains the optimal choice but its vertical position and length have a dependence on d. Furthermore, I found that the optimal force varies as $1/d$.

The umbrella shapes obtained in this chapter were designed to maximise the fifth force at a single point inside a spherical vacuum chamber. It is not necessarily a given, therefore, that they would be the best shape in an actual experiment, as experiments may use either moving particles, such as in atom interferometry, or an extended body as in torsion balance experiments. However, I believe that the property of the umbrella shapes, whereby the source is unscreened but the field reaches the value that minimises the effective potential inside the source, are generally necessary for optimising a fifth force experiment. Additionally, the method used in this chapter is general enough and sufficiently customisable that it can be tailored to specific experiments. One would only need to change the value outputted by the fitness function, obtained from the field solution, to whatever observable is used in that particular experiment. This is easily accomplished by extracting the required information from the field profile calculated using SELCIE, for example the total work done on a particle trajectory or scalar forces acting on an extended object. Any experimental constraints such as laser paths, particle trajectories, or different vacuum chamber shapes can also be enforced at the level of mesh generation using shape manipulation tools in SELCIE. These types of changes will likely break rotational symmetry and would therefore require solving the chameleon equations of motion using 3D meshes, which will greatly increase the simulation runtime and will therefore be left to future works.

Chapter 4

Analytic Solutions for Astrophysical Systems

The bulk of work in this thesis is in regards to using SELCIE to numerically solve for the chameleon field profile in laboratory sized experiments. Recall that the chameleon equation that is solved by SELCIE, equation (2.1), is defined over an arbitrary length scale. As demonstrated in section 2.5.4, SELCIE can therefore be used to solve for the field profile on astrophysical and cosmological scales just as easily as it can for laboratory scales. However, in this section I also showed that for a continuous density profile, such as the NFW profile discussed in section 2.5.4, a sufficiently small value of α leads to the field solution with the analytic form of equation (1.47), hence forth referred to as the tracing solution. This occurs because the gradient of the density profile becomes too large compared to the Compton wavelength of the field in the same region of space. Recalling the definition of α in equation (2.2), we see that small values of α, and therefore Compton wavelength through equation (2.4), are easier to obtain on astrophysical and cosmological scales, as apposed to laboratory scales. In this scenario, the use of computational solvers such as SELCIE is not necessary. It is therefore important to understand when the tracing solution is valid, and equivalently when tools like SELCIE are required.

In this chapter I will discuss work I contributed to the papers Ref. [2] and Ref. [3]. I will derive the general formula which determines whether the tracing solution is valid for an arbitrary continuous density profile. The following subsections will be dedicated to specific examples from cosmology, namely the NFW and void profiles.

4.1 Analytic Investigation

In this chapter I use the term tracing solution to refer to a field that is at the value that minimises its effective potential everywhere. For the case of a constant background density this will mean that field will have the same value throughout the domain. This scenario is possible no matter the size of the field's Compton wavelength. However, for background density profiles that vary continuously, then the tracing solution can only be valid if the density does not vary too much over distances comparable to the Compton wavelength of the field.

To show this explicitly, and find when the tracing solution becomes invalid, I applied a perturbation to the tracing solution such that $\hat{\phi} = \hat{\phi}_{\min} + \delta\hat{\phi}$. To obtain the form of this perturbation I start by rearranging the chameleon equation of motion shown in equation (2.1) into the form

$$\hat{\phi}(\hat{\rho}) = \hat{\phi}_{\min}(\hat{\rho}) \left(1 - \frac{\alpha \hat{\nabla}^2 \hat{\phi}}{\hat{\rho}}\right)^{\frac{-1}{(n+1)}}, \tag{4.1}$$

where $\hat{\phi}_{\min}(\hat{\rho})$ is defined as it is in equation (2.3). Taking $\alpha \hat{\nabla}^2 \hat{\phi} \ll \hat{\rho}$, equation (4.1) can be approximated as

$$\hat{\phi} \approx \hat{\phi}_{\text{min}}(\hat{\rho}) + \hat{\lambda}^2(\hat{\rho})\hat{\nabla}^2\hat{\phi} \tag{4.2}$$

where I have used the definition of the field's rescaled Compton wavelength $\hat{\lambda}(\hat{\rho})$, as shown in equation (2.4). Plugging equation (4.2) into itself and neglecting both higher derivatives of $\hat{\phi}$ and higher order terms in $\alpha\hat{\nabla}^2\hat{\phi}/\hat{\rho}$, I obtain that the linear perturbation of the tracing solution is

$$\delta\hat{\phi} \approx \hat{\lambda}^2(\hat{\rho})\hat{\nabla}^2\hat{\phi}_{\text{min}}. \tag{4.3}$$

For the tracing solution to be considered valid $\delta\hat{\phi} \ll \hat{\phi}$. Using the definition of $\hat{\phi}_{\text{min}}$ from equation (2.3), the above condition can be expressed as

$$\alpha \ll \frac{(n+1)^2\hat{\rho}^{\frac{(n+2)}{(n+1)}}}{\left[\frac{(n+2)}{(n+1)}\left(\frac{\hat{\nabla}\hat{\rho}}{\hat{\rho}}\right)^2 - \left(\frac{\hat{\nabla}^2\hat{\rho}}{\hat{\rho}}\right)\right]}. \tag{4.4}$$

I will now apply equation (4.4) to the NFW and void profiles, as was done in Ref. [2] and Ref. [3] respectively.

NFW Galaxy Cluster Profiles

In section 2.5.4 I mentioned some reasons why the NFW cluster profile is of interest. The rescaled form of the NFW profile is shown in equation (2.36). Applying this profile to equation (4.4) I obtain the tracing condition

$$\alpha \ll \frac{(n+1)^3\hat{\rho}_{\text{s}}^{\frac{(n+2)}{(n+1)}}\hat{r}}{\left[3\hat{r}^2(n+1) + (n+2)(1+6\hat{r})\right]\left[\hat{r}(1+\hat{r})\right]^{1/(n+1)}}. \tag{4.5}$$

Since the length and density scales, referred to as L and ρ_0 in section 2.1, are arbitrary, they can be chosen such that $\hat{\rho}_{\mathrm{s}} = 1$ and in the region of interest $\hat{r} \sim 1$. This will mean that the right-hand side of equation (4.5) will be of order one, in the region of interest, and therefore the condition for the tracing solution to be valid is simply $\alpha \ll 1$. This is affirmed by the result calculated by SELCIE, for $\alpha = 10^{-9}$, that is plotted in Figure 2.10a.

I note here that in both the limits $\hat{r} \to 0$ and $\hat{r} \to \infty$, the right-hand side of equation (4.5) goes to zero. This means no matter how small the value of α is, the tracing solution will become invalid at small $\hat{r}$ and at large $\hat{r}$. This is not too concerning, however, since the NFW profile is not realistic for values of $\hat{r}$ that are too small or large.

Void Density Profiles

In the context of cosmological tests of gravity, a system of special interest is that of cosmic voids. Voids are the largest underdensities in the Universe and their properties are inherently linked to the physics of large scale structure. Given these properties, cosmic voids make ideal cosmological laboratories for testing screened gravity theories. Using voids as a testing ground for models of modified gravity has been explored extensively in the literature (e.g. see Ref. [125, 126, 127, 128]). Previous works such as Ref. [129] have used void density profiles that obey a step function. In this case to solve the field profile a numerical solver such as SELCIE would be required. In Ref. [3], however, we investigated voids with a rescaled profile of the form

$$\hat{\rho}(\hat{r}) = \frac{1}{2}\left[(\hat{\rho}_{\mathrm{in}} + \hat{\rho}_{\mathrm{out}}) + (\hat{\rho}_{\mathrm{out}} - \hat{\rho}_{\mathrm{in}})\tanh(k(\hat{r} - \hat{r}_{\mathrm{step}}))\right], \tag{4.6}$$

where $\hat{\rho}_{\mathrm{in}}$, $\hat{\rho}_{\mathrm{out}}$, and k are constants. The value $\hat{r}_{\mathrm{step}}$ is also a constant that defines the 'edge' of the void. As $k \to \infty$, this profile converges to a step function, with density $\hat{\rho}_{\text{in}}$ for $\hat{r} < \hat{r}_{\text{step}}$ and density $\hat{\rho}_{\text{out}}$ for $\hat{r} > \hat{r}_{\text{step}}$.

Assuming $\hat{\rho}_{\text{in}} \ll \hat{\rho}_{\text{out}}$, after applying equation (4.6) to (4.4), the constraint on α is

$$\alpha \ll \frac{(n+1)^3}{k\left[(n+2)k - (n+1)\hat{r}_{\text{step}}^{-1}\right]} \left(\frac{\hat{\rho}_{\text{out}}}{2}\right)^{\frac{(n+2)}{(n+1)}}. \tag{4.7}$$

As with the NFW case, we are free to choose our length and density scales so that $\hat{r}_{\text{step}}$ and $\hat{\rho}_{\text{out}}$ are of order unity. Therefore, in the limiting case where k is large, the tracing solution will hold so long as $\sqrt{\alpha} \ll 1/k$. When $n = 1$, for α to lie in the allowed regions of the parameter space it must satisfy $\alpha < 10^{-12}$. Therefore, so long as $k \ll 10^6$, the tracing solutions will be valid, for all values of α allowed by the parameter space. Taking the derivative of equation (4.6) and evaluating it at the step, the constraint on k can be written in as $\rho'(r_{\text{step}})/\rho(r_{\text{step}}) \approx k \ll 10^6$, where I have reintroduced physical units. Slopes steeper than this must be solved using SELCIE or other numerical solvers.

Chapter 5

Conclusion

The chameleon is a scalar field model that conformally couples to matter and possesses a screening mechanism that causes fifth forces mediated by the field to become suppressed in regions of high density. Such a field could source the dark energy that drives the late time expansion of the universe whilst also avoiding observational constraints. However, the nonlinear dynamics that make the model interesting to study also makes obtaining field solutions very difficult, especially for irregularly shaped source masses. Therefore, to obtain solutions for arbitrary systems, computational methods must be employed.

In this thesis I have investigated how the strength of the chameleon fifth force has a dependence on the shape of the matter sourcing the field, in contrast to the gravitational force as predicted by GR. To perform this investigation I developed the SELCIE software package, details of which can be found in chapter 2. This package combines non-uniform mesh generation, the finite element software FEniCS, with nonlinear solving methods. The end result is a software package that allows the user to construct meshes representing arbitrarily complex systems and assign discrete or continuous density profiles to each sub-region independently from one another. The code will then solve the chameleon equation of motion, shown in equation 1.45, to produce a field profile for the given system. From this profile the resulting force can be calculated and from which experimental constraints can be obtained. This software is also very efficient, allowing the user to control which regions in the mesh are more refined than others and the level of refinement in each. This allows the simulations to have high precision in regions where it is required, whilst also not wasting computing power on unimportant regions. This is possible since SELCIE communicates information from the mesh through the finite element method, which importantly for our purposes does not require a uniform mesh. Additionally, systems that posses a symmetry, such as rotational or translational symmetry, can be expressed using 2D meshes, reducing the required computing resources.

In section 2.5 of this thesis I tested SELCIE against analytic solutions for the chameleon field from the literature including spherical, cylindrical, and ellipsoidal sources. The two former solutions had strong agreement throughout the domain, whilst the latter disagreed at small distances. This, however, was shown to likely be an issue with the analytic solution since it gave unphysical field values close to the source. I also tested the analytic solutions for NFW galaxy clusters in the regimes of the field's Compton wavelength being small and large, relative to the size of the cluster. The calculated results from the former agreed with the analytic results; however, the latter did not. I found that this was not an error with the numerical result but rather caused by the inclusion of a core region of constant density introduced to address the fact that the NFW profile diverges as $r \to 0$.

In chapter 3 I combined SELCIE with a genetic algorithm to produce code that would optimise an experiment. In this work the code optimised the shape of an axis-symmetric source mass inside a spherical vacuum chamber so that the resulting fifth force, at a fixed distance to the source, was maximised. I note here that the methodology of the code is more general and is easily altered to optimise other, possibly more realistic, experiments. The results of this investigation are discussed in section 3.3. Ultimately, the optimal shape found was an umbrella-like shape, with the location of the maximum force being located on the axis of rotation on the concave side of the shape. Compared to a spherical source of equal mass, centred at the origin, the umbrella shape had a fifth force 2.45 times stronger, when measured at the same separation distance. This affirms that fifth force experiments can receive improved sensitivity by optimising the shape of matter sources in the experiment.

In section 3.4 I investigated whether this optimal shape would change if I altered the distance from the source where the force was measured. I found that although the shapes returned by the genetic algorithm code changed position and length, they retained the umbrella-like shape and even the relative position where the force was maximised. I also found that each shape was the best choice when measuring at the distance it was optimised for, meaning that the optimal shape is dependent on the measuring distance. Finally, in section 3.5 I investigated how changing the field's potential affects the optimal shape. I found that not only were the umbrella shapes still the best choice, but the exact thickness of the umbrella in each case was such that the field just reaches its minimum value in the dense source. This meant that the source was unscreened while still having as small a minimum value as possible. This combination of features is interpreted as the main criteria for the optimal shape, and is hypothesised to be required even in a more realistic experiment where the fifth force is not measured at a single point but instead over a path or acting on an extended body.

I have shown in this work that not only does the shape of the sources of matter in a fifth force experiment affect the experiment sensitivity but I have also demonstrated a method to find the optimal shape for said experiments.

SELCIE is ideal for researchers working on the chameleon field, especially if they are interested in obtaining observables from systems that are very difficult to approximate. It has already been used to investigate the chameleon field profiles of astrophysical systems such as NFW galaxy clusters [2] and cosmic voids [3], for both of which I am a co-author. Additionally, SELCIE was recently used by members of the MICROSCOPE team in Ref. [118] to calibrate and test their own FEM code $femtoscope$.

Future plans for SELCIE include introducing time-dependent systems, and generalising the code so that it can also solve other screened scalar field models besides the chameleon. Some progress has already been made into adapting SELCIE to solve the symmetron equations of motion [130].

Bibliography

[1] Chad Briddon, Clare Burrage, Adam Moss, and Andrius Tamosiunas. SELCIE: a tool for investigating the chameleon field of arbitrary sources. *Journal of Cosmology and Astroparticle Physics*, 2021(12):043, dec 2021.

[2] Andrius Tamosiunas, Chad Briddon, Clare Burrage, Weiguang Cui, and Adam Moss. Chameleon screening depends on the shape and structure of nfw halos. *Journal of Cosmology and Astroparticle Physics*, 2022(04):047, 2022.

[3] Andrius Tamosiunas, Chad Briddon, Clare Burrage, Alan Cutforth, Adam Moss, and Thomas Vincent. Chameleon screening in cosmic voids. *Journal of Cosmology and Astroparticle Physics*, 2022(11):056, 2022.

[4] Chad Briddon, Clare Burrage, Adam Moss, and Andrius Tamosiunas. Using machine learning to optimise chameleon fifth force experiments, 2023.

[5] Adam G. Riess et al. Observational evidence from supernovae for an accelerating universe and a cosmological constant. *Astron. J.*, 116:1009–1038, 1998.

[6] Daniel J. Eisenstein, Idit Zehavi, David W. Hogg, Roman Scoccimarro, Michael R. Blanton, Robert C. Nichol, Ryan Scranton, Hee-

Jong Seo, Max Tegmark, Zheng Zheng, and et al. Detection of the baryon acoustic peak in the large-scale correlation function of sdss luminous red galaxies. *The Astrophysical Journal*, 633(2):560–574, Nov 2005.

[7] Daniel E. Holz and Scott A. Hughes. Using gravitational-wave standard sirens. *The Astrophysical Journal*, 629(1):15–22, Aug 2005.

[8] B. P. Abbott, R. Abbott, T. D. Abbott, S. Abraham, F. Acernese, K. Ackley, C. Adams, R. X. Adhikari, V. B. Adya, C. Affeldt, and et al. A gravitational-wave measurement of the hubble constant following the second observing run of advanced ligo and virgo. *The Astrophysical Journal*, 909(2):218, Mar 2021.

[9] Jerome Martin. Everything you always wanted to know about the cosmological constant problem (but were afraid to ask). *Comptes Rendus Physique*, 13(6-7):566–665, 2012.

[10] Ivaylo Zlatev, Li-Min Wang, and Paul J. Steinhardt. Quintessence, cosmic coincidence, and the cosmological constant. *Phys. Rev. Lett.*, 82:896–899, 1999.

[11] Edmund J. Copeland, M. Sami, and Shinji Tsujikawa. Dynamics of dark energy. *Int. J. Mod. Phys. D*, 15:1753–1936, 2006.

[12] Austin Joyce, Bhuvnesh Jain, Justin Khoury, and Mark Trodden. Beyond the Cosmological Standard Model. *Phys. Rept.*, 568:1–98, 2015.

[13] Y. Fujii and K. Maeda. *The Scalar-Tensor Theory of Gravitation.* Cambridge Monographs on Mathematical Physics. Cambridge University Press, 2003.

[14] E. G. Adelberger, Blayne R. Heckel, and A. E. Nelson. Tests of the gravitational inverse square law. *Ann. Rev. Nucl. Part. Sci.*, 53:77–121, 2003.

[15] D. J. Kapner, T. S. Cook, E. G. Adelberger, J. H. Gundlach, B. R. Heckel, C. D. Hoyle, and H. E. Swanson. Tests of the Gravitational Inverse-Square Law below the Dark-Energy Length Scale. *Phys. Rev. Lett.*, 98(2):021101, January 2007.

[16] Eric G Adelberger, JH Gundlach, BR Heckel, S Hoedl, and S Schlamminger. Torsion balance experiments: A low-energy frontier of particle physics. *Progress in Particle and Nuclear Physics*, 62(1):102–134, 2009.

[17] Kurt Hinterbichler and Justin Khoury. Symmetron Fields: Screening Long-Range Forces Through Local Symmetry Restoration. *Phys. Rev. Lett.*, 104:231301, 2010.

[18] Justin Khoury and Amanda Weltman. Chameleon cosmology. *Phys. Rev. D*, 69:044026, 2004.

[19] Alberto Nicolis, Riccardo Rattazzi, and Enrico Trincherini. The Galileon as a local modification of gravity. *Phys. Rev. D*, 79:064036, 2009.

[20] Amol Upadhye. Dark energy fifth forces in torsion pendulum experiments. *Phys. Rev. D*, 86:102003, 2012.

[21] Philippe Brax, Carsten van de Bruck, Anne-Christine Davis, David Fonseca Mota, and Douglas J. Shaw. Detecting chameleons through Casimir force measurements. *Phys. Rev. D*, 76:124034, 2007.

[22] Benjamin Elder, Valeri Vardanyan, Yashar Akrami, Philippe Brax,

Anne-Christine Davis, and Ricardo S. Decca. Classical symmetron force in Casimir experiments. *Phys. Rev. D*, 101(6):064065, 2020.

[23] René I. P. Sedmik and Mario Pitschmann. Next Generation Design and Prospects for Cannex. *Universe*, 7(7):234, 2021.

[24] Philippe Brax, Anne-Christine Davis, and Benjamin Elder. Casimir tests of scalar-tensor theories. *Physical Review D*, 107(8):084025, 2023.

[25] Peiran Yin, Rui Li, Chengjiang Yin, Xiangyu Xu, Xiang Bian, Han Xie, Chang-Kui Duan, Pu Huang, Jian-hua He, and Jiangfeng Du. Experiments with levitated force sensor challenge theories of dark energy. *Nature Phys.*, 18(10):1181–1185, 2022.

[26] Clare Burrage, Edmund J. Copeland, and E.A. Hinds. Probing Dark Energy with Atom Interferometry. *JCAP*, 03:042, 2015.

[27] Paul Hamilton, Matt Jaffe, Philipp Haslinger, Quinn Simmons, Holger Müller, and Justin Khoury. Atom-interferometry constraints on dark energy. *Science*, 349:849–851, 2015.

[28] Benjamin Elder, Justin Khoury, Philipp Haslinger, Matt Jaffe, Holger Müller, and Paul Hamilton. Chameleon Dark Energy and Atom Interferometry. *Phys. Rev. D*, 94(4):044051, 2016.

[29] Matt Jaffe, Philipp Haslinger, Victoria Xu, Paul Hamilton, Amol Upadhye, Benjamin Elder, Justin Khoury, and Holger Müller. Testing sub-gravitational forces on atoms from a miniature, in-vacuum source mass. *Nature Phys.*, 13:938, 2017.

[30] D. O. Sabulsky, I. Dutta, E. A. Hinds, B. Elder, C. Burrage, and Edmund J. Copeland. Experiment to detect dark energy forces using atom interferometry. *Physical Review Letters*, 123(6), Aug 2019.

[31] Philippe Brax and Clare Burrage. Atomic Precision Tests and Light Scalar Couplings. *Phys. Rev. D*, 83:035020, 2011.

[32] Philippe Brax, Anne-Christine Davis, and Benjamin Elder. Screened scalar fields in hydrogen and muonium. *Phys. Rev. D*, 107(4):044008, 2023.

[33] Philippe Brax and Guillaume Pignol. Strongly Coupled Chameleons and the Neutronic Quantum Bouncer. *Phys. Rev. Lett.*, 107:111301, 2011.

[34] A. N. Ivanov, R. Hollwieser, T. Jenke, M. Wellenzohen, and H. Abele. Influence of the chameleon field potential on transition frequencies of gravitationally bound quantum states of ultracold neutrons. *Phys. Rev. D*, 87(10):105013, 2013.

[35] Philippe Brax, Guillaume Pignol, and Damien Roulier. Probing Strongly Coupled Chameleons with Slow Neutrons. *Phys. Rev. D*, 88:083004, 2013.

[36] T. Jenke et al. Gravity Resonance Spectroscopy Constrains Dark Energy and Dark Matter Scenarios. *Phys. Rev. Lett.*, 112:151105, 2014.

[37] G. Cronenberg, H. Filter, M. Thalhammer, T. Jenke, H. Abele, and P. Geltenbort. A Gravity of Earth Measurement with a qBOUNCE Experiment. *PoS*, EPS-HEP2015:408, 2015.

[38] H. Lemmel, Ph. Brax, A. N. Ivanov, T. Jenke, G. Pignol, M. Pitschmann, T. Potocar, M. Wellenzohn, M. Zawisky, and H. Abele. Neutron Interferometry constrains dark energy chameleon fields. *Phys. Lett. B*, 743:310–314, 2015.

[39] K. Li et al. Neutron Limit on the Strongly-Coupled Chameleon Field. *Phys. Rev. D*, 93(6):062001, 2016.

[40] Philippe Brax, Santiago Casas, Harry Desmond, and Benjamin Elder. Testing Screened Modified Gravity. *Universe*, 8(1):11, 2021.

[41] Clare Burrage and Jeremy Sakstein. Tests of chameleon gravity. *Living Reviews in Relativity*, 21(1):1, March 2018.

[42] Clare Burrage and Jeremy Sakstein. A Compendium of Chameleon Constraints. *JCAP*, 11:045, 2016.

[43] Albert Einstein et al. The foundation of the general theory of relativity. *Annalen Phys*, 49(7):769–822, 1916.

[44] Frank Watson Dyson, Arthur Stanley Eddington, and Charles Davidson. Ix. a determination of the deflection of light by the sun's gravitational field, from observations made at the total eclipse of may 29, 1919. *Philosophical Transactions of the Royal Society of London. Series A, Containing Papers of a Mathematical or Physical Character*, 220(571-581):291–333, 1920.

[45] Irwin I Shapiro, Gordon H Pettengill, Michael E Ash, Melvin L Stone, William B Smith, Richard P Ingalls, and Richard A Brockelman. Fourth test of general relativity: preliminary results. *Physical Review Letters*, 20(22):1265, 1968.

[46] Benjamin P Abbott, Richard Abbott, TDe Abbott, MR Abernathy, Fausto Acernese, Kendall Ackley, Carl Adams, Thomas Adams, Paolo Addesso, RX Adhikari, et al. Observation of gravitational waves from a binary black hole merger. *Physical review letters*, 116(6):061102, 2016.

[47] Kazunori Akiyama et al. First M87 Event Horizon Telescope Results. I. The Shadow of the Supermassive Black Hole. *Astrophys. J. Lett.*, 875:L1, 2019.

[48] Kazunori Akiyama et al. First Sagittarius A* Event Horizon Telescope Results. I. The Shadow of the Supermassive Black Hole in the Center of the Milky Way. *Astrophys. J. Lett.*, 930(2):L12, 2022.

[49] Pierre Touboul, Gilles Métris, Manuel Rodrigues, Yves André, Quentin Baghi, Joël Bergé, Damien Boulanger, Stefanie Bremer, Patrice Carle, Ratana Chhun, et al. Microscope mission: first results of a space test of the equivalence principle. *Physical review letters*, 119(23):231101, 2017.

[50] John F Donoghue. Quantum general relativity and effective field theory. *arXiv preprint arXiv:2211.09902*, 2022.

[51] Roger Penrose. Gravitational collapse and space-time singularities. *Physical Review Letters*, 14(3):57, 1965.

[52] Nabila Aghanim, Yashar Akrami, Frederico Arroja, Mark Ashdown, J Aumont, Carlo Baccigalupi, M Ballardini, Anthony J Banday, RB Barreiro, Nicola Bartolo, et al. Planck 2018 results-i. overview and the cosmological legacy of planck. *Astronomy & Astrophysics*, 641:A1, 2020.

[53] Nabila Aghanim, Yashar Akrami, Mark Ashdown, J Aumont, C Baccigalupi, M Ballardini, AJ Banday, RB Barreiro, N Bartolo, S Basak, et al. Planck 2018 results-vi. cosmological parameters. *Astronomy & Astrophysics*, 641:A6, 2020.

[54] Steven Weinberg. The cosmological constant problem. *Reviews of modern physics*, 61(1):1, 1989.

[55] CP Burgess. The cosmological constant problem: why it's hard to get dark energy from micro-physics. *100e Ecole d'Ete de Physique: Post-Planck Cosmology*, pages 149–197, 2015.

[56] Stefan Nobbenhuis. Categorizing different approaches to the cosmological constant problem. *Foundations of Physics*, 36:613–680, 2006.

[57] Timothy Clifton, Pedro G Ferreira, Antonio Padilla, and Constantinos Skordis. Modified gravity and cosmology. *Physics reports*, 513(1-3):1–189, 2012.

[58] TMC Abbott, S Allam, P Andersen, C Angus, J Asorey, A Avelino, S Avila, BA Bassett, K Bechtol, GM Bernstein, et al. First cosmology results using type ia supernovae from the dark energy survey: constraints on cosmological parameters. *The Astrophysical Journal Letters*, 872(2):L30, 2019.

[59] E.G. Adelberger, J.H. Gundlach, B.R. Heckel, S. Hoedl, and S. Schlamminger. Torsion balance experiments: A low-energy frontier of particle physics. *Progress in Particle and Nuclear Physics*, 62(1):102–134, 2009.

[60] David Lovelock. The einstein tensor and its generalizations. *Journal of Mathematical Physics*, 12(3):498–501, 1971.

[61] David Lovelock. The four-dimensionality of space and the einstein tensor. *Journal of Mathematical Physics*, 13(6):874–876, 1972.

[62] Richard P. Woodard. Ostrogradsky's theorem on Hamiltonian instability. *Scholarpedia*, 10(8):32243, 2015.

[63] Clare Burrage, Edmund J Copeland, Peter Millington, and Michael Spannowsky. Fifth forces, higgs portals and broken scale invariance. *Journal of Cosmology and Astroparticle Physics*, 2018(11):036, 2018.

[64] J.M. Overduin and P.S. Wesson. Kaluza-klein gravity. *Physics Reports*, 283(5-6):303–378, apr 1997.

[65] Gregory Walter Horndeski. Second-order scalar-tensor field equations in a four-dimensional space. *International Journal of Theoretical Physics*, 10:363–384, 1974.

[66] David Langlois and Karim Noui. Degenerate higher derivative theories beyond horndeski: evading the ostrogradski instability. *Journal of Cosmology and Astroparticle Physics*, 2016(02):034, 2016.

[67] David Langlois and Karim Noui. Hamiltonian analysis of higher derivative scalar-tensor theories. *Journal of Cosmology and Astroparticle Physics*, 2016(07):016, 2016.

[68] Ph Brax, C Van de Bruck, AC Davis, J Khoury, and A Weltman. Chameleon dark energy. In *AIP conference proceedings*, volume 736, pages 105–110. American Institute of Physics, 2004.

[69] Clare Burrage, Edmund J. Copeland, and James A. Stevenson. Ellipticity weakens chameleon screening. *Physical Review D*, 91(6), Mar 2015.

[70] Philippe Brax, Anne-Christine Davis, and Benjamin Elder. (g-2)μ and screened modified gravity. *Phys. Rev. D*, 106(4):044040, 2022.

[71] Yuan-Ling Zhao, Yu-Jie Tan, Wen-Hao Wu, Jie Luo, and Cheng-Gang Shao. Constraining the chameleon model with the HUST-2020 torsion pendulum experiment. *Phys. Rev. D*, 103(10):104005, 2021.

[72] Carl T Kelley. *Iterative methods for linear and nonlinear equations.* SIAM, 1995.

[73] Martin S. Alnæs, Jan Blechta, Johan Hake, August Johansson, Benjamin Kehlet, Anders Logg, Chris Richardson, Johannes Ring, Marie E. Rognes, and Garth N. Wells. The fenics project version 1.5. *Archive of Numerical Software*, 3(100), 2015.

[74] Anders Logg, Kent-Andre Mardal, Garth N. Wells, et al. *Automated Solution of Differential Equations by the Finite Element Method*. Springer, 2012.

[75] Anders Logg and Garth N. Wells. Dolfin: Automated finite element computing. *ACM Transactions on Mathematical Software*, 37(2), 2010.

[76] Anders Logg, Garth N. Wells, and Johan Hake. *DOLFIN: a C++/Python Finite Element Library*, chapter 10. Springer, 2012.

[77] C. Geuzaine and J.-F. Remacle. Gmsh: a three-dimensional finite element mesh generator with built-in pre- and post-processing facilities. *International Journal for Numerical Methods in Engineering*, 79(11):1309–1331, 2009.

[78] Jonathan Braden, Clare Burrage, Benjamin Elder, and Daniela Saadeh. φenics: Vainshtein screening with the finite element method. *Journal of Cosmology and Astroparticle Physics*, 2021(03):010, Mar 2021.

[79] Clare Burrage, Ben Coltman, Antonio Padilla, Daniela Saadeh, and Toby Wilson. Massive Galileons and Vainshtein Screening. *JCAP*, 02:050, 2021.

[80] Amol Upadhye, Steven S. Gubser, and Justin Khoury. Unveiling chameleons in tests of gravitational inverse-square law. *Phys. Rev. D*, 74:104024, 2006.

[81] H.P. Langtangen and K.A. Mardal. *Introduction to Numerical Methods for Variational Problems*. Texts in Computational Science and Engineering. Springer International Publishing, 2019.

[82] Hans Petter Langtangen and Anders Logg. *Solving PDEs in Python*. Springer, 2017.

[83] Gilbert Strang. Piecewise polynomials and the finite element method. *Bull. Amer. Math. Soc.*, 79(6):1128–1137, 11 1973.

[84] Peter D Lax and Arthur N Milgram. Parabolic equations, volume 33 of annals of mathematics studies, 1954.

[85] Mamoru Shimizu, Tetsu Kitayama, Shin Sasaki, and Yasushi Suto. Mass-temperature relation of galaxy clusters: implications from the observed luminosity-temperature relation and x-ray temperature function. *The Astrophysical Journal*, 590(1):197, 2003.

[86] D. E. Applegate, A. Mantz, S. W. Allen, A. von der Linden, R. Glenn Morris, S. Hilbert, Patrick L. Kelly, D. L. Burke, H. Ebeling, D. A. Rapetti, and R. W. Schmidt. Cosmology and astrophysics from relaxed galaxy clusters – IV. Robustly calibrating hydrostatic masses with weak lensing. *Monthly Notices of the Royal Astronomical Society*, 457(2):1522–1534, 02 2016.

[87] A. R. Lyapin and R. A. Burenin. Relation between X-ray and Sunyaev—Zeldovich Galaxy Cluster Mass Measurements. *Astronomy Letters*, 45(7):403–410, July 2019.

[88] Ayumu Terukina, Lucas Lombriser, Kazuhiro Yamamoto, David Bacon, Kazuya Koyama, and Robert C. Nichol. Testing chameleon gravity with the Coma cluster. *JCAP*, 2014(4):013, April 2014.

[89] Harry Wilcox, David Bacon, Robert C. Nichol, Philip J. Rooney, Ayumu Terukina, A. Kathy Romer, Kazuya Koyama, Gong-Bo Zhao, Ross Hood, Robert G. Mann, Matt Hilton, Maria Manolopoulou, Martin Sahlén, Chris A. Collins, Andrew R. Liddle, Julian A. Mayers, Nicola Mehrtens, Christopher J. Miller, John P. Stott, and Pedro T. P. Viana. The XMM Cluster Survey: testing chameleon gravity using the profiles of clusters. *MNRAS*, 452(2):1171–1183, September 2015.

[90] Jeremy Sakstein, Harry Wilcox, David Bacon, Kazuya Koyama, and Robert C. Nichol. Testing gravity using galaxy clusters: new constraints on beyond Horndeski theories. *JCAP*, 2016(7):019, July 2016.

[91] Kazuya Koyama. Cosmological tests of modified gravity. *Reports on Progress in Physics*, 79(4):046902, April 2016.

[92] Matteo Cataneo and David Rapetti. Tests of gravity with galaxy clusters. *International Journal of Modern Physics D*, 27(15):1848006–936, January 2018.

[93] Andrius Tamosiunas, David Bacon, Kazuya Koyama, and Robert C. Nichol. Testing emergent gravity on galaxy cluster scales. *JCAP*, 2019(5):053, May 2019.

[94] Julio F. Navarro, Carlos S. Frenk, and Simon D. M. White. A Universal Density Profile from Hierarchical Clustering. *ApJ*, 490(2):493–508, December 1997.

[95] Clare Burrage, Edmund J. Copeland, Adam Moss, and James A. Stevenson. The shape dependence of chameleon screening. *JCAP*, 2018(1):056, January 2018.

[96] Dylan O. Sabulsky, Indranil Dutta, E. A. Hinds, Benjamin Elder,

Clare Burrage, and Edmund J. Copeland. Experiment to detect dark energy forces using atom interferometry. *Phys. Rev. Lett.*, 123(6):061102, 2019.

[97] Philippe Brax. Testing Chameleon Fields with Ultra Cold Neutron Bound States and Neutron Interferometry. *Phys. Procedia*, 51:73–77, 2014.

[98] Stephan Sponar, René I. P. Sedmik, Mario Pitschmann, Hartmut Abele, and Yuji Hasegawa. Tests of fundamental quantum mechanics and dark interactions with low-energy neutrons. *Nature Rev. Phys.*, 3(5):309–327, 2021.

[99] Tobias Jenke, Joachim Bosina, Jakob Micko, Mario Pitschmann, Rene Sedmik, and Hartmut Abele. Gravity resonance spectroscopy and dark energy symmetron fields: qBOUNCE experiments performed with Rabi and Ramsey spectroscopy. *Eur. Phys. J. ST*, 230(4):1131–1136, 2021.

[100] Martin Pernot-Borràs, Joel Bergé, Philippe Brax, Jean-Philippe Uzan, Gilles Métris, Manuel Rodrigues, and Pierre Touboul. Constraints on chameleon gravity from the measurement of the electrostatic stiffness of the MICROSCOPE mission accelerometers. *Phys. Rev. D*, 103(6):064070, 2021.

[101] R. S. Decca, D. Lopez, E. Fischbach, G. L. Klimchitskaya, D. E. Krause, and V. M. Mostepanenko. Novel constraints on light elementary particles and extra-dimensional physics from the Casimir effect. *Eur. Phys. J. C*, 51:963–975, 2007.

[102] Attaallah Almasi, Philippe Brax, Davide Iannuzzi, and René I. P. Sedmik. Force sensor for chameleon and Casimir force experiments with parallel-plate configuration. *Phys. Rev. D*, 91(10):102002, 2015.

[103] René Sedmik and Phillippe Brax. Status Report and first Light from Cannex: Casimir Force Measurements between flat parallel Plates. *J. Phys. Conf. Ser.*, 1138(1):012014, 2018.

[104] Galina L. Klimchitskaya and Vladimir M. Mostepanenko. Dark Matter Axions, Non-Newtonian Gravity and Constraints on them from Recent Measurement of the Casimir Force in the Micrometer Separation Range. *Universe*, 7:N9, 9 2021.

[105] Andrew A. Geraci, Scott B. Papp, and John Kitching. Short-range force detection using optically-cooled levitated microspheres. *Phys. Rev. Lett.*, 105:101101, 2010.

[106] Alexander D. Rider, David C. Moore, Charles P. Blakemore, Maxime Louis, Marie Lu, and Giorgio Gratta. Search for Screened Interactions Associated with Dark Energy Below the 100 μm Length Scale. *Phys. Rev. Lett.*, 117(10):101101, 2016.

[107] Jian Liu and Ka-Di Zhu. Cavity optomechanical spectroscopy constraints chameleon dark energy scenarios. *Eur. Phys. J. C*, 78(3):266, 2018.

[108] Sofia Qvarfort, Dennis Rätzel, and Stephen Stopyra. Constraining modified gravity with quantum optomechanics. *New Journal of Physics*, 24(3):033009, 2022.

[109] Alessandra Silvestri. Scalar Radiation from Chameleon-Shielded Regions. *Phys. Rev. Lett.*, 106(25):251101, June 2011.

[110] Jeremy Sakstein. Stellar Oscillations in Modified Gravity. *Phys. Rev. D*, 88(12):124013, 2013.

[111] Amol Upadhye and Jason H Steffen. Monopole radiation in modified gravity. *arXiv preprint arXiv:1306.6113*, 2013.

[112] Philippe Brax, Anne-Christine Davis, and Jeremy Sakstein. Pulsar Constraints on Screened Modified Gravity. *Class. Quant. Grav.*, 31:225001, 2014.

[113] R. Hagala, C. Llinares, and D. F. Mota. Cosmic Tsunamis in Modified Gravity: Disruption of Screening Mechanisms from Scalar Waves. *Phys. Rev. Lett.*, 118(10):101301, 2017.

[114] Taishi Ikeda, Vitor Cardoso, and Miguel Zilhão. Instabilities of scalar fields around oscillating stars. *Physical Review Letters*, 127(19):191101, 2021.

[115] Katherine Jones-Smith and Francesc Ferrer. Detecting Chameleon Dark Energy via Electrostatic Analogy. *Phys. Rev. Lett.*, 108:221101, 2012.

[116] R. Pourhasan, N. Afshordi, R. B. Mann, and A. C. Davis. Chameleon Gravity, Electrostatics, and Kinematics in the Outer Galaxy. *JCAP*, 12:005, 2011.

[117] Valeri Vardanyan and Deaglan J Bartlett. Modeling and testing screening mechanisms in the laboratory and in space. *arXiv preprint arXiv:2305.18899*, 2023.

[118] Hugo Lévy, Joël Bergé, and Jean-Philippe Uzan. Solving nonlinear Klein-Gordon equations on unbounded domains via the finite element method. *Phys. Rev. D*, 106(12):124021, 2022.

[119] Félix-Antoine Fortin, François-Michel De Rainville, Marc-André Gardner, Marc Parizeau, and Christian Gagné. DEAP: Evolutionary algorithms made easy. *Journal of Machine Learning Research*, 13:2171–2175, jul 2012.

[120] John R Koza, Martin A Keane, Matthew J Streeter, William Mydlowec, Jessen Yu, and Guido Lanza. *Genetic programming IV: Routine human-competitive machine intelligence*, volume 5. Springer Science & Business Media, 2005.

[121] Andrew N. Sloss and Steven Gustafson. 2019 Evolutionary Algorithms Review. *arXiv e-prints*, page arXiv:1906.08870, June 2019.

[122] D.E. Goldberg. *Genetic Algorithms in Search, Optimization, and Machine Learning*. Addison Wesley series in artificial intelligence. Addison-Wesley, 1989.

[123] Brad L. Miller and David E. Goldberg. Genetic algorithms, tournament selection, and the effects of noise. *Complex Syst.*, 9, 1995.

[124] M.J. Kochenderfer and T.A. Wheeler. *Algorithms for Optimization*. MIT Press, 2019.

[125] Yan-Chuan Cai, Nelson Padilla, and Baojiu Li. Testing gravity using cosmic voids. *Monthly Notices of the Royal Astronomical Society*, 451(1):1036–1055, 2015.

[126] Eder LD Perico, Rodrigo Voivodic, Marcos Lima, and David F Mota. Cosmic voids in modified gravity scenarios. *Astronomy & Astrophysics*, 632:A52, 2019.

[127] ND Padilla. Testing gravity with cosmic voids. *Boletin de la Asociacion Argentina de Astronomia La Plata Argentina*, 57:6–11, 2015.

[128] Christopher T Davies, Marius Cautun, and Baojiu Li. Cosmological test of gravity using weak lensing voids. *Monthly Notices of the Royal Astronomical Society*, 490(4):4907–4917, 2019.

[129] Joseph Clampitt, Yan-Chuan Cai, and Baojiu Li. Voids in modified gravity: excursion set predictions. *Monthly Notices of the Royal Astronomical Society*, 431(1):749–766, 2013.

[130] Kate Clements, Benjamin Elder, Lucia Hackermueller, Mark Fromhold, and Clare Burrage. Detecting dark domain walls. *arXiv preprint arXiv:2308.01179*, 2023.

Appendices

Appendix A

Genetic Algorithm Calibration

In this work I used DEAP [119], a software package designed to construct and perform GA simulations. DEAP comes equipped with a wide range of options including choices for selection, crossover, and mutation methods, each with their own control parameters. Before using the GA to optimise our fitness function, as laid out in section 3.2, I first tested the various possible configurations of the GA to find the most optimal one. This was accomplished using a test fitness function where the fitness value is the non-overlapping cross-sectional area of an input and target shape, both created using the Legendre polynomial parameterisation defined in section 3.3.2. Therefore, the goal of the GA in these simulations is to minimise this fitness value and return coefficients that are as close to the target ones as possible.

Due to the large number of possible configurations, I decided to treat our choice of selection, crossover and mutation methods as being independent from one another. This greatly reduces the number of configurations that require testing. For each of these configurations the GA was run 10 times. The distribution of the number of generations needed to reach convergence and the corresponding fitness values outputted by the GA are both plotted in Figure A.1 for a range of configurations. Additionally, I used this same test to evaluate other in-build algorithms available in DEAP, information on which can be found at `https://deap.readthedocs.io/en/master/api/algo.html`. Taking both the fitness distribution and number of generations until convergence into account I ultimately found the best choice of those tested was a custom algorithm that uses the methods: cxUniform(indpb=0.5) for crossover (configuration 3 in top plot of Figure A.1), mutGaussian(sigma=0.1) for mutation (configuration 1 in middle plot of Figure A.1), and selTournament(tournsize=10) for the selection method (configuration 1 in bottom plot of Figure A.1). Finally, I tested the effects of changing the input parameters of the chosen methods and found little effect on the distributions of the fitness values or number of generations until convergence.

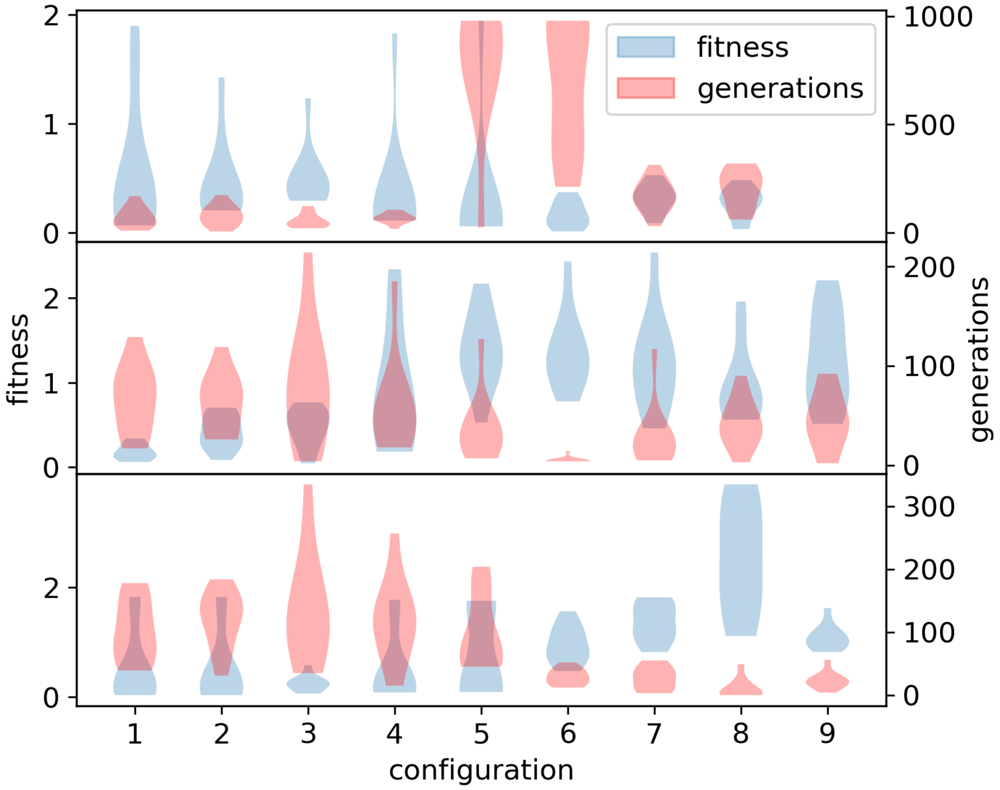

Figure A.1: Violin plots showing the distribution of the number of generations taken to reach convergence and corresponding fitness values outputted by 10 runs of the GA for a range of configurations, the details of which can be found at `https://deap.readthedocs.io/en/master/api/tools.html`. The fitness value is the non-overlapping cross-sectional area of the outputted shape and a target shape with coefficients $[0.5, 2, 0.9, 1.3]$, both of which are created using the Legendre polynomial parameterisation described in section 3.3.2. In each plot the selection, crossover, and mutation stages not being varied are set as selTournament(tournsize=10), cxUniform(indpb=0.5), and mutGaussian(sigma=0.1), respectively. The number of individuals in each population was 100. In the **top** plot the crossover method is varied with the configuration number, from left to right, corresponding to [cxOnePoint(), cxTwoPoint(), cxUniform(indpb=0.5), cxBlend(alpha=0.1), cxSimulatedBinary(eta=0.1), cxSimulatedBinary(eta=0.5), cxSimulatedBinaryBounded(eta=0.1), cxSimulatedBinaryBounded(eta=0.5)]. In the **middle** plot the mutation method is varied and the configurations are [mutGaussian(sigma=0.1), mutGaussian(sigma=0.3), mutGaussian(sigma=0.5), mutGaussian(sigma=0.7), mutGaussian(sigma=0.9), mutShuffleIndexes(), mutPolynomialBounded(eta=0.1), mutPolynomialBounded(eta=0.5), mutPolynomialBounded(eta=1.0)]. The **bottom** has the selection method being varied between [selTournament(tournsize=10), selTournament(tournsize=20), selTournament(tournsize=30), selTournament(tournsize=40), selTournament(tournsize=50), selNSGA2(), selSPEA2(), selRandom(), selBest()].

Appendix B

Defining Measuring Surface

Since I aim to investigate how the shape of the source contributes to the chameleon force, I require all other contributing factors to be kept unchanged. This includes the distance from the source where measurements are performed, which shall henceforth be denoted as d. Since the shapes used in this work can have a high level of complexity to them, the method used to enforce the measuring distance must work for arbitrary shapes. In this section I will discuss the different methods developed and compare them.

Refinement Method

The first method developed was to iterate over each of the mesh's vertex points and only consider the points which lie inside the vacuum chamber subdomain and that satisfy the required distance constraint. Recall that the boundary of the source is defined by a list of points P_{i}, where $\mathrm{i} \in [0, \mathrm{N}]$. The shortest distance between a point, P_{m}, and the surface of the source can then be approximated by measuring the Euclidean distance between

P_{m} and each P_{i}, as shown in equation (B.1).

$$\Delta_m \approx \underset{\mathrm{i}}{\operatorname{argmin}} \sqrt{\sum_{\mathrm{j}=0}^{3} (P_{\mathrm{i,j}} - P_{\mathrm{m,j}})^2} \tag{B.1}$$

This value becomes a better approximation as the separation distance between consecutive source boundary points decreases. Since the likelihood of a mesh vertex lying within machine precision ($\sim 10^{-14}$) of the distance d is ludicrously small, I must define a tolerance T_d. Therefore, if $\Delta_{\mathrm{m}} \in d \pm T_d/2$ then the field gradient at P_{m} will be recorded. Of these recorded values the largest is returned as the measurement.

An obvious problem with this method is the number of computations required. To find which vertices are a part of the vacuum subdomains a number of operations equal to the total number of vertices in the mesh need to be performed. If I have N_{vac} vertices in the vacuum mesh with N_{vac} and a source boundary defined by N_{s} points, then the number of times equation (B.1) would need to be called is $N_{\mathrm{vac}} \times N_{\mathrm{s}}$. As the mesh precision is increased this quickly becomes a very large number of operations, and consequently this procedure for obtaining the measurement is slow. Furthermore, this method introduces an error on the measuring distance of $T_d/2$, which will also produce an error on the measurement that favours vertices closer to the source where the field gradients are typically larger. However, decreasing T_d does not improve the error. This is because if T_d is reduced so as to be smaller than the typical cell size within the measuring distance, then it becomes increasingly likely for no values to be recorded in some regions. Therefore, T_d has a minimum size and so the error on the measurement will persist.

Boundary Method

Another method I developed involves modifying the mesh generating code so that what was previously the vacuum subdomain is now two distinct subdomains, and the surface between them (hence forth the measuring surface) is at all points a shortest distance d from the source boundary. Once such a mesh is constructed, rather than iterating over all vertices in the mesh and performing distance calculations, instead one simply iterates over the vertices on this new surface and returns the largest value field gradient magnitude as before. This resolves the problems with the previous method since there is no need to iterate over all the mesh vertices and of the ones I do, no distance calculation is required. Furthermore, the uncertainty on the true distance from the source to the vertices I measure are now at machine precision rather than the somewhat arbitrary $T_d/2$. Finally, an additional benefit is that since the measuring surface connects two subdomains, the size of the cells on this surface can be manually set in the code. This gives the user the ability to control the number of vertices, for increased spatial accuracy, and the precision of the field and field gradient profiles on the measuring surface. To construct the measuring surface around a 2D source formed from the list of points P_{i}, I constructed the following algorithm.

First a sorted copy of the list P_{i} is made such that the point with the largest y value is the first entry, while also preserving the ordering of the points. The reason for this is that it forces the first point of the measuring surface to be convex and so will always be located at the point $(x_0, y_0 + d)$, regardless of the behavior of the rest of the curve. In the case of multiple points sharing the same y-value then the first instance is chosen. The list is also made periodic by appending a duplicate of the first entry to the end of the list, so as to avoid "index out of range" errors later in the algorithm.

Next both the lengths and directions are calculated for the separation vectors between consecutive points $P_{\rm i}$ and $P_{\rm i+1}$ for $\rm i \in [0, N]$, and are labelled $l_{\rm i}$ and $\vec{n}_{\rm i}$, respectively. These two lists are also made periodic in the same way $P_{\rm i}$ was. For a convex shape, each point in the source boundary, $\vec{x}_{\rm i}$, corresponds to two points in the measuring surface given by

$$\vec{x}_{\rm i}^{(+)} = \vec{x}_{\rm i} + \mathcal{R}\vec{n}_{\rm i} \tag{B.2}$$

$$\vec{x}_{\rm i}^{(-)} = \vec{x}_{\rm i} + \mathcal{R}\vec{n}_{\rm i-1}, \tag{B.3}$$

where the matrix $\mathcal{R}$ is defined as

$$\mathcal{R} = \sigma d \begin{pmatrix} 0 & 1 & 0 \\ -1 & 0 & 0 \\ 0 & 0 & 0 \end{pmatrix}. \tag{B.4}$$

Here σ has magnitude unity but its sign depends on whether the points defining the source boundary run in the clockwise or counter-clockwise direction. Since the sign of σ is fixed for any given boundary (otherwise the measuring surface would intersect the source boundary) it can therefore be calculated around the first boundary point where the boundary's direction is unambiguous due to it having the largest y-value. Using the fact that all vectors $\vec{n}_{\rm i}$ have a zero z component, the formula for σ can be written as

$$\sigma = \mathrm{sgn}((\vec{n}_{\rm N-1} \times \vec{n}_0) \cdot \hat{z}) \tag{B.5}$$

To construct the measuring surface, an arc length, centred at $\vec{x}_{\rm i}$, is constructed starting at $\vec{x}_{\rm i}^{(-)}$ and ending at $\vec{x}_{\rm i}^{(+)}$. This arc is then connected to a line that joins $\vec{x}_{\rm i}^{(+)}$ and $\vec{x}_{\rm i+1}^{(-)}$. This process is then repeated for each point defining the source boundary to form the measuring surface. However, for concave source boundaries this introduces the possibility of intersecting lines and even lines going through the source boundary. To ensure the algorithm works for any closed source boundary, the algorithm computes where intersections will occur in advance and modify the measuring surface during construction.

The lines used to construct the surface each correspond to a single point belonging to the source boundary, such that the point $\vec{x}_\mathrm{i}$ maps to

$$\vec{L}_\mathrm{i} = \vec{n}_\mathrm{i} u_\mathrm{i} + \vec{x}_\mathrm{i}^{(+)}, \tag{B.6}$$

where $\vec{x}_\mathrm{i}^{(+)}$ is given in equation (B.2), and $u_\mathrm{i} \in [0, l_\mathrm{i}]$. If another line, $\vec{L}_\mathrm{k}$, were to intersect this initial line then this would occur if

$$u_\mathrm{i} = \frac{(\vec{\delta}_\mathrm{ik} \times \vec{n}_\mathrm{k}) \cdot \hat{z} + \sigma d (1 - \vec{n}_\mathrm{i} \cdot \vec{n}_\mathrm{k})}{(\vec{n}_\mathrm{i} \times \vec{n}_\mathrm{k}) \cdot \hat{z}}, \tag{B.7}$$

lay in the range $u_\mathrm{i} \in [0, l_\mathrm{i}]$, and

$$u_\mathrm{k} = \frac{(\vec{\delta}_\mathrm{ik} \times \vec{n}_\mathrm{i}) \cdot \hat{z} - \sigma d (1 - \vec{n}_\mathrm{i} \cdot \vec{n}_\mathrm{k})}{(\vec{n}_\mathrm{i} \times \vec{n}_\mathrm{k}) \cdot \hat{z}}, \tag{B.8}$$

in the range $u_\mathrm{k} \in [0, l_\mathrm{k}]$, where $\hat{z}$ is the unit vector in the z-direction, and $\vec{\delta}_\mathrm{ik} = \vec{x}_\mathrm{k} - \vec{x}_\mathrm{i}$. Another possibility is that the line $\vec{L}_\mathrm{i}$ intersects the arc length centred at $\vec{x}_\mathrm{k}$ instead of the accompanying line. This can only occur if $\vec{L}_\mathrm{i}$ comes within a distance d of the point $\vec{x}_\mathrm{k}$, which then means that $\eta_\mathrm{ik}^2 \geq 0$ where

$$\eta_\mathrm{ik}^2 = ((\vec{\delta}_\mathrm{ik} \times \vec{n}_\mathrm{i}) \cdot \hat{z})(2\sigma d - ((\vec{\delta}_\mathrm{ik} \times \vec{n}_\mathrm{i}) \cdot \hat{z})). \tag{B.9}$$

This alone does not guarantee that the line intersects the arc length that accompanies $\vec{x}_\mathrm{k}$. However, since $\vec{L}_\mathrm{i}$ starts on the measuring surface if it were to come within a distance d of the point $\vec{x}_\mathrm{k}$, but not intersect the accompanying arc length, then it must have intersected another part of the surface first, with a small value of u_i. Therefore, since I am only interested in the first intersection, the condition $\eta_{\mathrm{ik}}^2 \geq 0$ is enough to ensure an intersection with the arc length. If this occurs then the position on the line where the first intersection occurs will be at

$$u_{\mathrm{i}} = (\vec{\delta}_{\mathrm{ik}} \cdot \vec{n}_{\mathrm{i}}) - |\eta_{\mathrm{ik}}|. \tag{B.10}$$

The procedure to determine where the line L_{i} should end is to iterate over all values k > i and return the smallest value of u_{i}[1]. This value then gives the position of the intersection through equation (B.6). This becomes the starting point of the proceeding line, or arc, and the index is set to k, skipping all the points between i and k. In the case of a line-line intersection this means the lower bound of u_{k} is the value returned by equation (B.8). For a line-arc intersection the starting point of the arc length will the position of the intersection instead of $\vec{x}_{\mathrm{k}}^{(-)}$.

When determining if the arc length A_{i} is ended prematurely due to an intersection I again use $\eta_{\mathrm{ik}}^2 \geq 0$ to determine whether the line L_{k} comes within a distance d of the point $\vec{x}_{\mathrm{i}}$. If it does it will do so when

$$u_{\mathrm{k}} = -(\vec{\delta}_{\mathrm{ik}} \cdot \vec{n}_{\mathrm{k}}) \pm s|\eta_{\mathrm{ik}}|, \tag{B.11}$$

where

$$s = \sigma \mathrm{sgn}((\vec{n}_{\mathrm{i}} \times \vec{n}_{\mathrm{k}}) \cdot \hat{z}). \tag{B.12}$$

However, unlike in the line-arc intersection case, $\eta_{\mathrm{ik}}^2 \geq 0$ is not enough to ensure the intersection is on the arc length itself. I must therefore test which of the points given in equation (B.11) lie on the arc length and in the case of both which occurs earliest. To accomplish this I calculate the tangent vector to the chord connecting the start ($\vec{x}_{\mathrm{start}}$) and end ($\vec{x}_{\mathrm{end}}$) of

---

[1] Since the last point in the list is a copy of the first, interactions between these points are ignored.

the arc length

$$\vec{T} = (\vec{x}_{\text{end}} - \vec{x}_{\text{start}}) \times ((\vec{x}_{\text{end}} - \vec{x}_{\text{start}}) \times (\vec{x}_{\text{centre}} - \vec{x}_{\text{start}})), \tag{B.13}$$

where $\vec{x}_{\text{centre}}$ is the centre of the circle. If a point $\vec{x}$ lies on the arc length then $(\vec{x} - \vec{x}_{\text{start}}) \cdot \vec{T} \geq 0$. When such an intersection point is found, $\vec{T}$ can be updated using the intersection point as the new $\vec{x}_{\text{end}}$, thus ensuring the next intersection point will occur earlier (closer to $\vec{x}_{\text{start}}$).

If $|\vec{\delta}_{\text{ik}}| < 2d$ then there will exist two intersection points of circles centred at $\vec{x}_{\text{i}}$ and $\vec{x}_{\text{k}}$ located at

$$\vec{x}_{\text{p}} = \vec{x}_{\text{i}} + \frac{1}{2}\vec{\delta}_{\text{ik}} \pm \xi \mathcal{R} \vec{\delta}_{\text{ik}}, \tag{B.14}$$

where

$$\xi = \sqrt{\frac{1}{|\vec{\delta}_{\text{ik}}|^2} - \frac{1}{4d^2}}. \tag{B.15}$$

I use the same method as before to check whether either of these points are located on the arc length A_{i}, and if so which occurs earliest. As with the line case this will be done for all line and arc lengths corresponding to the points $\vec{x}_{\text{k}}$ where $\text{k} > \text{i}$. After which, the arc length will be constructed, terminating at the earliest intersection point, and the algorithm will skip to the line or arc length responsible for the intersection.

One disadvantage of this method compared to the first is that it is designed to work for systems defined on a 2D mesh, while the first method could also be applied to 3D systems. In theory an algorithm that constructs the measuring surface for a 3D source could be developed; however, in this work I focus on systems that can be expressed using a 2D mesh, and so a more complicated algorithm is not required.

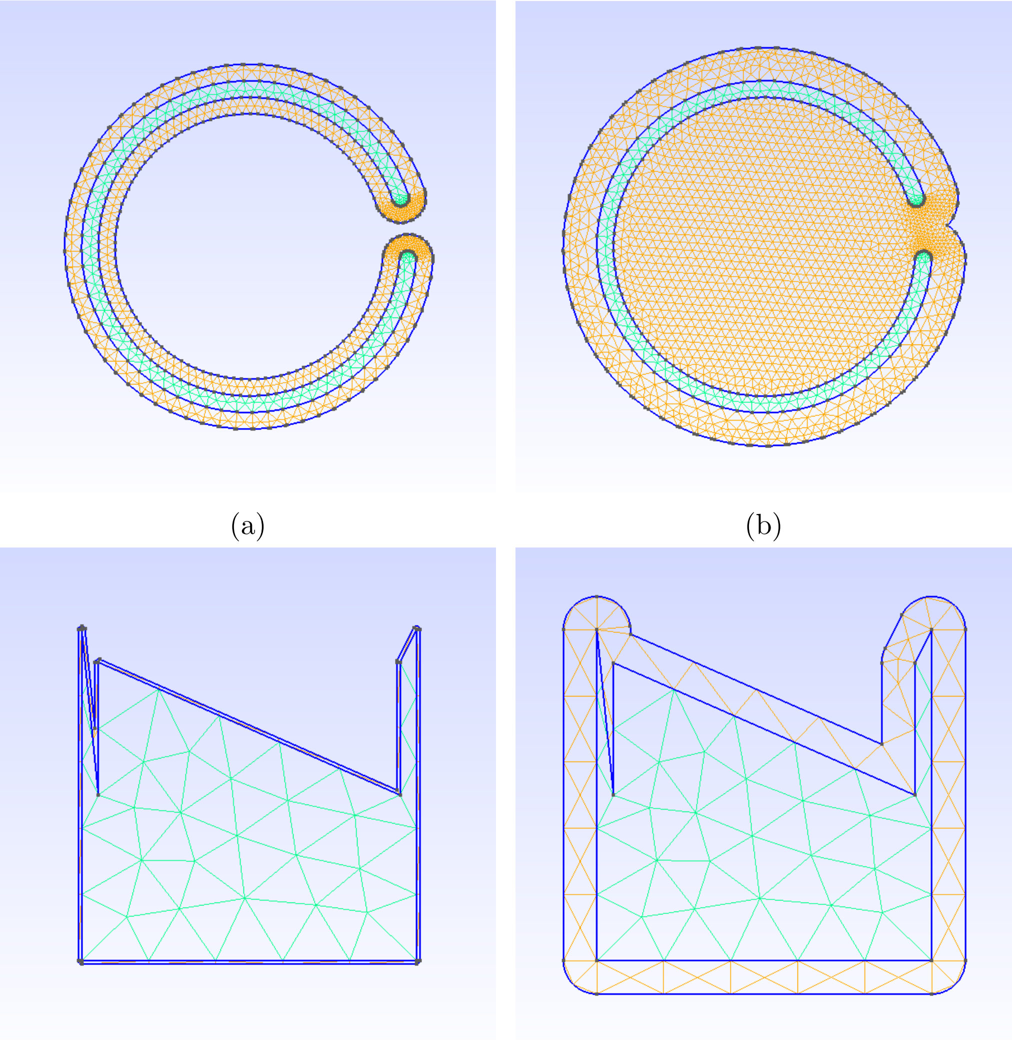

(a) (b)

(c) (d)

Figure B.1: Example meshes of the boundary surfaces constructed using the boundary method algorithm. In **a)** and **b)** the separation distance between the source shape and measuring surface is 0.1 and 0.2 respectively, while in **c)** and **d)** the separation distance is 10^{-3} and 10^{-2} respectively.

Some examples of measuring surface meshes constructed using this method are shown in Figure B.1

Comparison Between the Methods

To compare the two methods outlined above, I ran two copies of code that found the maximum fifth force around at a distance $d = 1/30$ to a source of density $\hat{\rho}_c = 10^{17}$, in a unit radius spherical vacuum chamber with a wall thickness of 0.1, and a background density of $\hat{\rho}_{\mathrm{bg}} = 1$. The source shape used is the axis-symmetric Legendre polynomial shape shown in Figure 2.2b. Both meshes used the settings (CellSizeMin = 10^{-4}, CellSizeMax = 0.1, DistMax = 0.4) for both the source and wall boundary. In the boundary method, the settings for the measuring surface were (CellSizeMin = 10^{-2}, CellSizeMax = 0.1, DistMax = 0.4), while in the refinement method the cell size in the measuring region was dictated by the equation $10^{-4} + 700\Delta_{\mathrm{m}}^2$.

The time taken for each section of the code to run was recorded and is shown in Table B.1. Comparing the run times of the two methods we see that although the initial time required to generate the mesh is long, all other parts of the algorithm are quicker. This is especially true for when the fifth force is being measured, since on the measuring surface fewer points need to be evaluated and the evaluation does not require any additional computation.

	Refinement Method ($\mathcal{M}_1$)	Boundary Method ($\mathcal{M}_2$)	Ratio ($\mathcal{M}_1/\mathcal{M}_2$)
Construct mesh (s)	122.02	374.216	~ 0.33
Construct density (s)	11.96	5.19	~ 2.31
Setup solver class (s)	93.70	59.02	~ 1.59
Solve field (s)	210.62	111.86	~ 1.88
Solve gradient (s)	1.51	0.63	~ 2.40
Make bounding box (s)	5.57	1.08	~ 5.17
Measure fifth force (s)	273.31	1.27	~ 214.50
Total run time (s)	718.70	553.26	~ 1.30
Measures force (10^{-6})	4.517	4.482	~ 1.01

Table B.1: A table containing the runtimes of each section of the fitness function described in section 3.3, but using different approaches to measuring where the fifth force is maximised.

Appendix C

Test Mesh Settings

Throughout this work I have simulated source masses inside of a unit radius vacuum chamber. The meshes used to perform these simulations consist of three boundaries: source, measuring, and the inner chamber wall[1]. The level of mesh refinement in the vicinity of each of these boundaries is controlled by the four parameters: CellSizeMin, CellSizeMax, DistMin, and DistMax. This would imply that the total number of parameters controlling the refinement of the mesh is twelve. I chose to set DistMin = 0 in all simulations, therefore reducing the number of parameters by three. This can be reduced by another three due to a degeneracy between CellSizeMax and DistMax when the other parameters are fixed. To determine how these six remaining parameters, three CellSizeMin and three DistMax, affect the measured value of the force and the total runtime, I ran simulations varying these parameters. The results are shown in Figure C.1. We see that for the ranges tested the fifth force always stayed within a 1% bound. Additionally, we see that changes to the wall boundary setting, both CellSizeMin and DistMax, had the largest effect on the runtime. Since the GA will call

---

[1] The refinement of the outer wall is left unconstrained and so will depend on the setting of the inner wall.

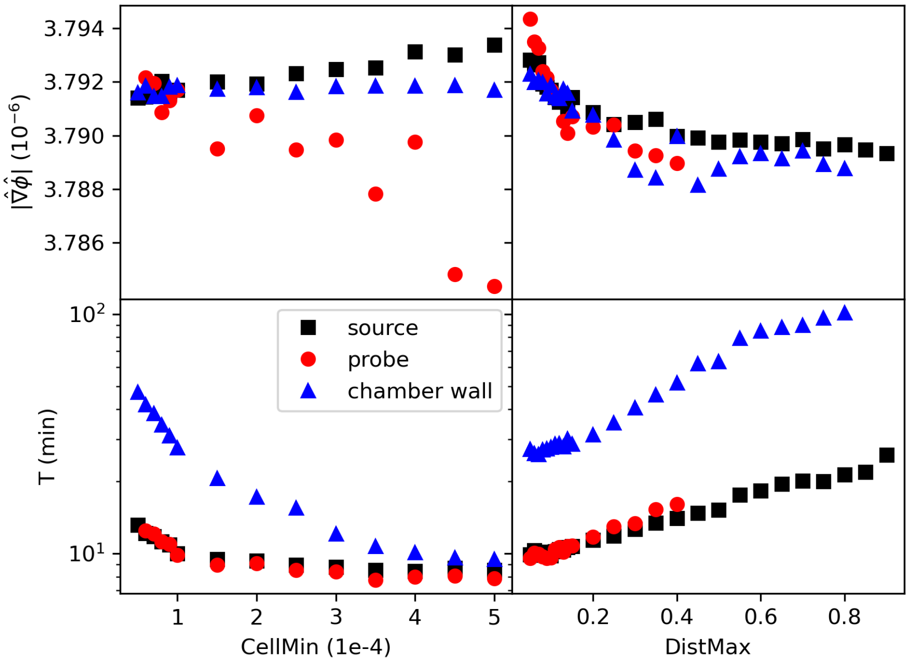

Figure C.1: Plots of measured fifth force ($|\hat{\nabla}\hat{\phi}|$), and runtime in minutes, against mesh settings CellSizeMin and DistMax for each boundary. All parameters not being varied are set to the default values of CellSizeMax = 0.01, DistMin = 0, and DistMax = 0.1. The default values for CellSizeMin for the source and measuring boundaries was 10^{-4}, and 5×10^{-4} for the wall boundary.

this function multiples times it is important to balance precision against runtime. Using the results in Figure C.1, I concluded that the default values chosen were satisfactory and were therefore used throughout the work in chapter 3.

Appendix D

Constraint Volume of Legendre shapes

Expanding out the Legendre polynomials in equation (3.6), it can be written as

$$R(x) = \sum_k C_k x^{2k} + \not{C}_k x^{2k+1}, \tag{D.1}$$

where I have used the short-hand

$$\begin{aligned} C_k &= \sum_q a_{2q} \left(\frac{(-1)^{q-k}(2q+2k)!}{4^q (q-k)!(q+k)!(2k)!} \right) \\ \not{C}_k &= \sum_q a_{2q+1} \left(1 + \frac{(-1)^{q-k}(2q+2k)!}{4^q (q-k)!(q+k)!(2k)!} \right). \end{aligned} \tag{D.2}$$

The volume of this shape can be calculated by performing the integral

$$V = \frac{2\pi}{3} \int_0^{\pi} [R(\cos\theta)]^3 H(R(\cos\theta)) \sin\theta d\theta, \tag{D.3}$$

where $H(x)$ is the Heavy step function. The reason for introducing $H(x)$ is that for some combinations of a_i, it is possible for equation 3.6 to be negative at some θ values. When this occurs, if $|R(\cos\theta)| < |R(\cos{(\theta+\pi)})| =$

$|R(-\cos\theta)|$ then the negative regions could be interpreted as holes in the shape. However, this condition can also be broken and so I choose to ignore these negative values by including $H(x)$. Evaluating the integral in equation D.3 gives

$$\begin{aligned}
V &= \frac{2\pi}{3}\int_{-1}^{1}[R(x)]^3 H(R(x))dx \\
&= \frac{2\pi}{3}\sum_i \int_{\omega_i^-}^{\omega_i^+}[R(x)]^3 dx \\
&= \frac{2\pi}{3}\sum_i \sum_{k_1,k_2,k_3}\int_{\omega_i^-}^{\omega_i^+}\left(C_{k_1}C_{k_2}C_{k_3} + 3C_{k_1}C_{k_2}\not{C}_{k_3}x\right. \\
&\qquad\qquad\qquad\qquad \left. + 3C_{k_1}\not{C}_{k_2}\not{C}_{k_3}x^2 + \not{C}_{k_1}\not{C}_{k_2}\not{C}_{k_3}x^3\right)x^{2(k_1+k_2+k_3)}dx \\
&= \frac{2\pi}{3}\sum_{k_1,k_2,k_3}\left(\frac{C_{k_1}C_{k_2}C_{k_3}}{2k+1}\Omega^{(2k+1)} + \frac{3C_{k_1}C_{k_2}\not{C}_{k_3}}{2k+2}\Omega^{(2k+2)}\right. \\
&\qquad\qquad \left. + \frac{3C_{k_1}\not{C}_{k_2}\not{C}_{k_3}}{2k+3}\Omega^{(2k+3)} + \frac{\not{C}_{k_1}\not{C}_{k_2}\not{C}_{k_3}}{2k+4}\Omega^{(2k+4)}\right).
\end{aligned} \tag{D.4}$$

In the first line of equation (D.4) I used the transformation $x = \cos\theta$. I then used the Heavy step function to break the integral into terms bounded by the roots of $R(x)$. In the final line I used the short-hand

$$\Omega^{(n)} = \sum_i \left(\omega_i^+\right)^n - \left(\omega_i^-\right)^n, \tag{D.5}$$

and $k = k_1 + k_2 + k_3$. Using this equation for the volume, I can rescale the coefficients, a_i, such that the volume has a particular value, η. Since each term in this expression possesses a combination of three a_i-coefficients, any set of coefficients can be mapped to a unique set that possesses the correct volume through the rescaling

$$a_i \to \tilde{a}_i = \left(\frac{V(a_i)}{\eta}\right)^{\frac{1}{3}} a_i, \tag{D.6}$$

where $V(a_i)$ is the volume of the original set of coefficients as given by equation D.4.

Appendix E

Rescaling Shapes to Constrain Volume

In our simulations the continuous space is replaced by a mesh consisting of discrete cells. For a 3D mesh these cells would consist of tetrahedrons with 4 vertices. In this case, measuring the volume of the shape simply involves summing over the volumes of each individual cell that comprises it. For systems with an imposed symmetry, the system can be represented using a 2D mesh consisting of triangular cells made with three vertices. I therefore wish to know how to calculate the volume of the full 3D shape using its 2D intersection and knowledge of the symmetry.

For rotational symmetry we can imagine projecting each of the triangular cells comprising the shape around the axis of symmetry. For cells not touching the axis this will lead to triangular tori centred on the axis, while cells touching the axis will form cone segments. I find that the volume of one of these rotationally extended triangles is

$$V = \frac{2\pi}{3}A(\delta_1 + \delta_2 + \delta_3), \tag{E.1}$$

where A is the area of the triangle and δ_i, for $i \in \{1, 2, 3\}$, are the distances between the vertices of the triangle and the axis of rotation. To obtain the total volume of the shape, I iterate over every cell comprising the shape and calculate the volume contribution of each cell using equation E.1.

In this work, shapes are constructed by joining a series of points together by straight lines to form their boundary. These points are defined on a plane by the radial values R_n, for $n \in [0, N]$, and have an angular separation $\delta\theta = \pi/N$. Therefore the nth triangle will be defined by the vertices at $(R_n, n\pi/N)$, $(R_{n+1}, (n+1)\pi/N)$, and the origin. Using equation (E.1) and summing over all the triangles the total volume of the shape is

$$V = \frac{\pi}{3}\sin(\delta\theta)\sum_{n=0}^{N-1} R_n R_{n+1}[R_{n+1}\sin((n+1)\delta\theta) + R_n \sin(n\delta\theta)]. \tag{E.2}$$

By performing the rescaling $R_i \to \epsilon R_i$, we see from equation (E.2) that the value transforms as $V \to \epsilon^3 V$. This means if I first calculate the volume using equation (E.2) and define $\epsilon = (V/\bar{V})^{1/3}$, then by rescaling the radial distances by ϵ this will act to fix the volume of the shape to be the target volume V.